Suspended calcium carbonate

2023 ASPRS INTERNATIONAL TECHNICAL SYMPOSIUM

JUNE 12-16, 2023
VIRTUAL

ASPRS is happy to announce the dates of its virtual conference. The 2023 ASPRS International Technical Symposium will take place.

The symposium will consist of:

- 15-minute oral presentations
- 5-minute Ignite-style presentations
- Poster Gallery
- Sustaining Member Vendor Spotlights
- ASPRS Society Highlights

Sessions will run each day from 10:00 AM to 6:00 PM Eastern Daylight Time (UTC - 4). All sessions will be recorded and made available on-demand to conference registrants. Presenters are eligible to submit full manuscripts for publication in the ISPRS Archives.

Interested in Presenting? For more information or to submit an abstract visit https://my.asprs.org/2023Symposium/2023-Symposium/Call-for-Abstracts.aspx

- Submission deadline is May 1, 2023
- Presenters will be notified of acceptance by May 8, 2023
- Presenters must be registered for the conference by May 22, 2023 to be included in the conference program

Registration Fees

- ASPRS Member $150 USD
- ASPRS Student Member $ 50 USD
- ASPRS Emeritus Member $ 25 USD
- Non Member $250 USD

Sponsorship Opportunities

- Vendor Spotlight/Product Demo
- Day Sponsor
- Session Sponsor
- Workshop Sponsor

"We are happy to offer this educational opportunity to the geospatial community. Virtual events are an excellent way to exchanammunity without the cost and time constraints of travel," said Karen Schuckman, ASPRS Executive Director

HTTPS://MY.ASPRS.ORG/2023SYMPOSIUM/

To have your press release published in *PE&RS*, contact Rae Kelley, rkelley@asprs.org.

INDUSTRY**NEWS**

ANNOUNCEMENTS

2023 William T. Pecora Award Nominations Now Being Accepted through May 1, 2023—The William T. Pecora Award is presented annually to individuals or groups who have made outstanding contributions toward understanding the Earth by means of remote sensing. The Department of the Interior (DOI) and the National Aeronautics and Space Administration (NASA) jointly sponsor the award.

The award was established in 1974 to honor the memory of Dr. William T. Pecora, former Director of the U.S. Geological Survey and Under Secretary, Department of the Interior. Dr. Pecora was a motivating force behind the establishment of a program for civil remote sensing of the Earth from space. His early vision and support helped establish what we know today as the Landsat satellite program.

The Award Committee must receive nominations for the 2023 award by May 1, 2023. Additional information can be found at www.usgs.gov/pecora or on the attached flyer; and questions can be directed to the Executive Secretary and Committee at pecora@usgs.gov.

Esri, the global leader in geographic information system (GIS) and location intelligence, honored select partners for their outstanding application of GIS software during the Plenary session at the Esri Partner Conference (EPC) held at the Palm Springs Convention Center in Palm Springs, CA. The award-winning companies are organizations in the Esri Partner Network and are recognized for their innovation and excellence in helping customers succeed with ArcGIS technology.

EPC award categories and winners include the following:

Analytics to Insights Award—*Delivering analytics and insights to users through location intelligence*: **Dewberry** and StreetLight Data.

ArcGIS Marketplace Award—*Outstanding presence on ArcGIS Marketplace*: VertiGIS North America.

ArcGIS SaaS Adoption Award—*Evolving customers and solutions to ArcGIS using SaaS*: Pandell Technology and Pro-West & Associates.

ArcGIS Software Adoption Award—*Demonstrating highly-aligned solutions built with ArcGIS software products*: Arora Engineers and Geo Data AG.

Cloud System Implementation Award—*Ensuring customer success through comprehensive implementation of the ArcGIS system in the cloud*: Axim Geospatial and ROK Technologies.

Creative Content Award—*Delivering creative content to ArcGIS users*: **Nearmap** and **Vexcel Imaging**.

GIS for Diversity Award—*Leveraging GIS in service to diversity, equity, inclusion, and belonging*: GISetc, a division of Critical Think and Timmons Group.

GIS for Good Award—*Compelling use of Esri technology to make an impact on current issues around the world*: Dymaptic and Nelson Intelligence Solutions.

Innovation Award—*Use of ArcGIS system in an innovative or disruptive way*: Houseal Lavigne and vGIS

Partner-to-Partner Collaboration Award—*Innovative technical or business collaboration between partners*: Datastory, GeoMarvel, and SymGEO.

Sustainable Development Award—*Helping customers meet global sustainable development goals by understanding their needs, mapping their work, measuring impact, analyzing performance, and engaging stakeholders*: Blue Raster and Codex Remote.

Top Co-Sell Partner Award—*Positively influences the adoption of Esri technology through solution sales, software implementation, and/or consulting engagements*: Geographic Technologies and SSP Innovations.

Top Solution Partner Award—*Drives the use of Esri technology through the sales of commercial solutions*: Motorola Solutions and VertiGIS GmbH.

Top Startup Partner Award—*Substantial opportunities for growth with Esri*: ICEYE.

The Esri Partner Conference was held March 4–6, 2023. During this event, organizations in the Esri partner community collaborate and network, hear about Esri's vision and new opportunities, build business relationships, learn from Esri experts, exchange ideas, discover the latest technology releases, and make plans for growing their businesses.

To learn more about the Esri Partner Network, visit go.esri.com/EsriPartnerNetwork.

Woolpert was a huge winner at the annual Geo Week conference in Denver, taking home multiple top awards. Geo Week combines the International Lidar Mapping Forum, SPAR 3D Expo & Conference, and AEC Next conferences to provide the geospatial industry's keystone event.

Literally chief among those honored was Woolpert Vice President and Chief Scientist Qassim Abdullah, who received the Lidar Leader Outstanding Personal Achievement Award. In addition to helping write standards upon which the industry is based, Abdullah serves as an advisor for agencies like NOAA and the Transportation Research Board, teaches

graduate students at Penn State University and the University of Maryland Baltimore County, and writes a monthly *Mapping Matters Column* for the *PE&RS*. Through these and countless other efforts, Abdullah continues to advance the lidar industry. He has been an immensely valued leader at Woolpert for more than 10 years.

Woolpert also received the Lidar Leader Outstanding Innovation in Lidar Award. The award was for the firm's Bathymetric Unmanned Littoral LiDar for Operational GEOINT technologies and sensor, also known as BULLDOG. Woolpert was granted a U.S. patent for its "Airborne Topo-Bathy Lidar System and Methods Thereof," and a lidar sensor system was developed by a multidisciplinary research and development team incorporating these technologies. These technologies enable the collection of high-resolution topographic and bathymetric data at a higher altitude, resulting in a broader swath than previously developed lidar systems. The Joint Airborne Lidar Bathymetry Technical Center of Expertise (JALBTCX) contracted with Woolpert to develop BULLDOG.

"Commercially available airborne lidar bathymetry systems currently operate at low altitudes, which are far below the altitudes of topographic lidar systems," Woolpert Vice President Nathan Hopper said. "Increasing the operational altitude of airborne lidar bathymetry systems to 10,000 feet presented several challenges that required novel approaches. This patent covers the proprietary technology developed to overcome the many challenges associated with high-altitude topography and bathymetry."

Hopper, Woolpert Senior Vice President and Geospatial Leader Joseph Seppi, Woolpert Vice President Mark Smits, and Chris Macon, a physical scientist for the U.S. Army Corps of Engineers, were instrumental to this technology and were on hand to accept the award. Collaboration with JALBTCX was key to this groundbreaking technology.

Woolpert also was honored with the MAPPS Membership Choice Award for a project that involved mission-critical data delivery for geohazard defense in Barry Arm, Alaska. The award recognized the work of eTrac, a Woolpert Company, and its immediate response to emergency request from U. S. Geological Survey and the Alaska Division of Geological and Geophysical Surveys.

The team acquired and expedited the delivery of bathymetric survey data to support accurate modeling of the seafloor and the region's steep continental slope, which was at risk for tsunami-generating submarine landslides that could lead to catastrophic loss of life and property. Woolpert Senior Vice President Jeff Lovin accepted the award on behalf of Woolpert Market Director and Certified Hydrographer Dave Neff.

Finally, Woolpert Vice President and Survey Discipline Leader David Kuxhausen received the **ASPRS Outstanding Service Award**. Kuxhausen's experience in photogrammetric and geodetic surveys, UAS data collection and analysis, and mobile lidar applications is unparalleled. He has been an outstanding leader and mentor at Woolpert for 24 years.
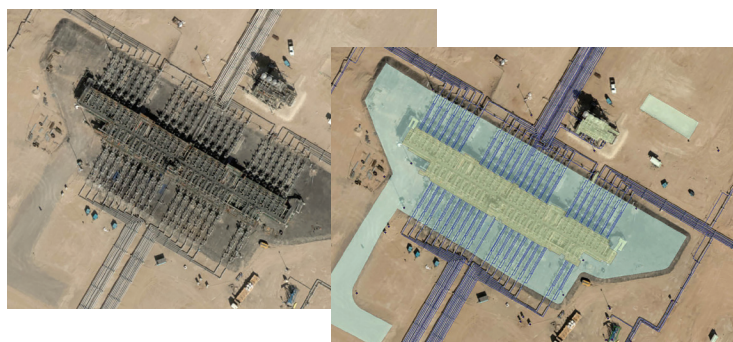
❥~

Request for Public Comment on a Draft Standard Ocean Mapping Protocol—The National Ocean Mapping, Exploration, and Characterization (NOMEC) Council and the Interagency Working Group on Ocean and Coastal Mapping (IWG-OCM) request public comment from all interested parties on the IWG-OCM's draft Standard Ocean Mapping Protocol (SOMP). The draft SOMP was developed in accordance with Objective 2.1 of the National Strategy for Ocean Mapping, Exploring, and Characterizing the United States Exclusive Economic Zone (National Strategy). Objective 2.1 directs the IWG-OCM to establish a SOMP to encourage consistency in data acquisition, stewardship and data management across a subset of ocean sensing capabilities for seafloor mapping, including bathymetry (acoustic and airborne), seabed backscatter, water column backscatter, side scan sonar imagery, sub-bottom profiling, and magnetometer data readings.

Comments must be received via email by 5:00 PM (ET) on June 2, 2023.

https://www.federalregister.gov/documents/2023/02/24/2023-03795/request-for-public-comment-on-a-draft-standard-ocean-mapping-protocol
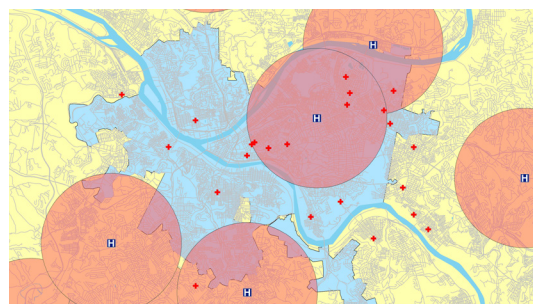
CALENDAR

197 Mapping Kuwait Oil Company's Assets using Photogrammetry Techniques

By Adnan Dashti, Faisal Al-Bous, Fahad Al Ajmi, Nasser Al Ajmi, Nasir Osman, and Ramesh Mahishi V Murthy

203 GIS Tips & Tricks — Buffers Everywhere but Where You Want Them?

211 A GPU-Accelerated PCG Method for the Block Adjustment of Large-Scale High-Resolution Optical Satellite Imagery Without GCPs

Qing Fu, Xiaohua Tong, Shijie Liu, Zhen Ye, Yanmin Jin, Hanyu Wang, and *Zhonghua Hong*

The precise geo-positioning of high-resolution satellite imagery (HRSI) without ground control points (GCPs) is an important and fundamental step in global mapping, three-dimensional modeling. In this article, to improve the efficiency of large-scale bundle adjustment (BA), we propose a combined Preconditioned Conjugate Gradient (PCG) and Graphic Processing Unit (GPU) parallel computing approach for the BA of large-scale HRSI without GCPs.

221 Identification of Drought Events in Major Basins of Africa from GRACE Total Water Storage and Modeled Products

Ayman M. Elameen, Shuanggen Jin, and *Daniel Olago*

Terrestrial water storage (TWS) plays a vital role in climatological and hydrological processes. Most of the developed drought indices from the Gravity Recovery and Climate Experiment (GRACE) over Africa neglected the influencing roles of individual water storage components in calculating the drought index and thus may either underestimate or overestimate drought characteristics. In this article, we proposed a Weighted Water Storage Deficit Index for drought assessment over the major river basins in Africa (i.e., Nile, Congo, Niger, Zambezi, and Orange) with accounting for the contribution of each TWS component on the drought signal.

233 Lightweight Parallel Octave Convolutional Neural Network for Hyperspectral Image Classification

Dan Li, Hanjie Wu, Yujian Wang, Xiaojun Li, Fanqiang Kong, and *Qiang Wang*

Although most deep learning-based methods have achieved excellent performance for hyperspectral image (HSI) classification, they are often limited by complex networks and require massive training samples in practical applications. Therefore, designing an efficient, lightweight model to obtain better classification results under small samples situations remains a challenging task. To alleviate this problem, a novel, lightweight parallel octave convolutional neural network (LPOCNN) for HSI classification is proposed in this article.

245 Model-Driven Precise Degradation Analysis Method of Highway Marking Using Mobile Laser Scanning Point Clouds

Ruifeng Ma, Xuming Ge, Qing Zhu, Xin Jia, Huiwei Jiang, Min Chen, and *Tao Liu*

Highway markings (HMs) are representative elements of inventory digitalization in highway scenes. The accurate position, semantics, and maintenance information of HMs provide significant support for the intelligent management of highways. This article presents a robust and efficient approach for extracting, reconstructing, and degrading analyzing HMs in complex highway scenes.

facebook.com/ASPRS.org   linkedin.com/groups/2745128   twitter.com/ASPRSorg   youtube.com/user/ASPRS

COVER DESCRIPTION

As early as the 1930s, researchers noticed that odd, milky-white patches of water sporadically discolor the generally bluer and shallow waters of the Bahama Banks. Sampling the discolored water patches made clear that these whiting events were caused by an abundance of fine-grained calcium carbonate particles suspended in the water.

However, why surges of calcium carbonate end up suspended in the water at particular times has never been clear. Some experts have argued that it is mainly a mechanical process, with currents dredging up calcium carbonate sediments. Others have proposed that phytoplankton blooms and other biological or chemical processes might be key to triggering whiting events.

"But in actuality, there is no scientific consensus on what cause them," explained Chuanmin Hu, an oceanographer at the University of South Florida.

The Operational Land Imager (OLI) on Landsat 8 captured this natural-color image of a whiting event off the west coast of Great Bahama Bank on April 4, 2015. The bright spots—whitings—are surrounded by shallow water. Whiting events generally persist for a few days to three months; the event shown here lasted for about two months before fading away.

In a recent attempt to better understand what causes whiting events, a team of University of South Florida researchers, led by Hu, developed a machine learning model that analyzed thousands of satellite images of the Bahama Banks collected by NASA's Aqua satellite between 2003-2020. In doing so, the research team assembled the longest and most detailed monthly, seasonal, and annual records of Bahama Bank whiting events ever created, according to Hu. The results were recently published in *Remote Sensing of Environment*.

The researchers reported stark seasonal patterns in the timing of whiting events, with significantly more of them happening in the spring and winter. They found large variations in the size of individual whiting patches, from 0.1 to 226 square kilometers, with the average size being 2.4 square kilometers for the Great Bahama Bank, roughly the size of 450 American football fields.

Most striking, the team observed what they termed a "mysterious" increase in the total area affected by whiting events, which rose from an average of about 25 square kilometers in 2003 to as much as 300-350 square kilometers in 2014-2015. After 2015, the total area affected began to decline gradually, returning to about 25 square kilometers by 2020. The cover image shows an event during the peak of whiting activity in January 2015.

"I wish I could tell you why we saw that peak in activity, but we're not there yet," said Hu. "We do see some interesting relationships between environmental conditions, such as the pH, the salinity of water, and the behavior of winds and currents, but we can't yet say what exact mechanical, biological, or chemical processes were responsible for that peak in activity. Ultimately, we need to do more field experiments and pair that with remote sensing research like this to better understand the formation processes."

For more information, visit https://landsat.visibleearth.nasa.gov/view.php?id=150866.

NASA Earth Observatory image by Joshua Stevens, using Landsat data from the U.S. Geological Survey. Story by Adam Voiland.

MAPPING KUWAIT OIL COMPANY'S ASSETS USING PHOTOGRAMMETRY TECHNIQUES

Adnan Dashti, Faisal Al-Bous, Fahad Al Ajmi, Nasser Al Ajmi, Nasir Osman, Ramesh Mahishi V Murthy

Operations Technical Services (North Kuwait), Kuwait Oil Company, Kuwait

●Introduction

The Infrastructure Master Plan (IMP) of the Operations Support Group, Kuwait Oil Company (KOC) is responsible for developing a Master Plan to manage the oil field's surface footprint. IMP produces and maintains the data used for planning, operations and Health, Safety & Environment (HSE) activities. IMP primarily uses the data from land survey to create a basemap. However, areas that are hazardous and inaccessible to surveyors create data voids. IMP supplements the missing details with data compiled using photogrammetry techniques. IMP utilizes DATEM Summit Evolution with ArcGIS and ArcGIS Pro for stereo visualization and photogrammetry data compilation.

●Mapping Approach

Aerial data acquisition for photogrammetry data compilation was performed using Leica RCD 30 Digital Imagery Sensor mounted on a Rockwell International 690A aircraft. The details of Aerial acquisition of the project were published in Photogrammetric Engineering & Remote Sensing, Vol. 87, No. 5, May 2021, pp. 313-317, DOI: 10.14358/PERS.87.5.313.

Mapping KOC assets involves coincident activities such as land survey and photogrammetry data compilation which were carefully planned so there were not duplication of effort or areas creating data voids. KOC fully understands that the utilities within inaccessible areas cannot be mapped by land surveyors. For instance, the extents of oil lakes which were created due to oil spills from the invasion of Iraq, the vital KOC assets within oil lake boundaries, etc., the access to which could pose life threatening risks to land surveyors.

●Challenges during Photogrammetry Data Compilation

The industry experts would agree that photogrammetry data compilation, though sounds easy, is quite a tedious task influenced by various external factors. The experience of IMP was no exception. Some of the challenges faced during the project life cycle and mitigation steps were:

1. Manpower mobilization- Kuwait has a small Photogrammetry industry in comparison to other third-world countries where there are many more photogrammetry production suppliers. Identifying experienced photogrammetry data compilers within the State of Kuwait posed to be a major challenge. The project could not be outsourced due to data sensitivity. In order to complete the task, manpower with experience in similar projects from the Middle East region were selected. With the onset of the COVID 19 pandemic, the selected manpower could not be mobilized on time due to the closure of international borders. In order to mitigate the risk of delay, locally available manpower was trained and used for data compilation. When International borders were open for foreigners to enter Kuwait, specialized manpower was mobilized

2. Changing the order of Survey- The project was conceptualized with photogrammetry data compilation as the first step, followed by land survey to update the attribute information. Since the photogrammetry data compilation schedule was pushed ahead, due to non-availability of manpower and other resources, the priority of areas of land survey had to be changed.

3. Updating Attribute information- Photogrammetrically compiled data does not have all the attribute information which are otherwise collected by field surveyors. Updating missing and/or incorrect attribute information to the compiled data was a challenge as some of the infrastructure had changed or were removed over time.

4. Connecting Above ground and Underground features- KOC's infrastructure such as pipelines, instrumentation cables, electric lines, etc., are both above and underground. Data compilation is possible for features visible and identifiable on stereo aerial images. However, underground assets can only be collected by field survey techniques. Working with data continuity from two sources is often a challenge. In order to overcome this, surveyors are provided with maps of areas where photogrammetry data compilation was completed. Changes to the above ground assets and connectivity of underground assets were updated.

5. Data currency- Aerial Images used for data compilation dates back to 2019, meaning the changes to the infrastructure post aerial acquisition date are not reflected in the images, making it difficult for surveyors to use the data in all areas. In order to overcome this, priority was given to areas within close vicinity of facilities such as Gathering Centers (GC) and Booster Stations (BS) where there would be little change to the infrastructure. Additionally, since the general topography within the oil fields have not changed much over the past three-years,

the data was also used to generate a Digital Terrain Model (DTM).

● Software

The selection of Software was another important step in the project's life cycle. KOC uses ESRI ArcGIS to create, edit, and store data. The ease of data integration within the enterprise GIS system could not be overlooked. Therefore, DATEM for ArcGIS and ArcGIS Pro software were selected for 3D visualization and data compilation. The selected software allows the user to edit, add, delete, and modify the features in the database concurrently. In addition, the data from feature compilation could be directly integrated to the enterprise GIS system.

● Photogrammetry Data Compilation

The primary goal of the project was to update the digital database that users' access to manage the assets, analysis for modeling purposes, as well as produce hard-copy maps. In addition to KOC assets, to depict the terrain as per the required accuracy standards, breaklines are also being captured. Breaklines are compiled to support 1-meter contour interval. The data compilation is being carried out using digital photogrammetric vector data acquisition methods, skilled photogrammetry compilers, following strict quality control (QC) procedures. Data processing techniques, the algorithms used in the topographical structuring of the data, the processing sequence and the procedures employed in the production of the final dataset are in strict accordance with KOC specification.

The process involved in data compilation is shown in Figure 2:

· Input data consists of aerial images, exterior orientation (EO) parameters, camera details, etc. The number of images are checked against the corresponding EO file to ensure completeness.

· Project setup is completed in DATEM Summit Evolution and in ArcGIS Pro. The project setup in DATEM Summit Evolution is carried out by creating the camera file referring to ADS 30. A control file is created by importing the EO parameters obtained after the completion of the aerial triangulation process. The project is set to UTM Zone 38 N projection of WGS 84. In ArcGIS Pro, a new geodatabase is created followed by a mosaic dataset. Camera details are entered and the EO parameters from summit evolution are imported. Stereo models are built for data compilation.

· QC of the project setup involves verifying that   the correct camera file is being used, checking if all the images are imported to the project, checking the stereo model footprint, checking the project parameters, etc.

· Data compilation is carried out adhering to KOC's specification and using the Enterprise Geodatabase. Tools within DATEM Summit Evolution such as contour generation and seamless update during data compilation come in handy during the production of the DTM. Only supplementary breaklines to support contours of 1-meter interval were compiled..

Figure 1. Photogrammetry Data Compilation.
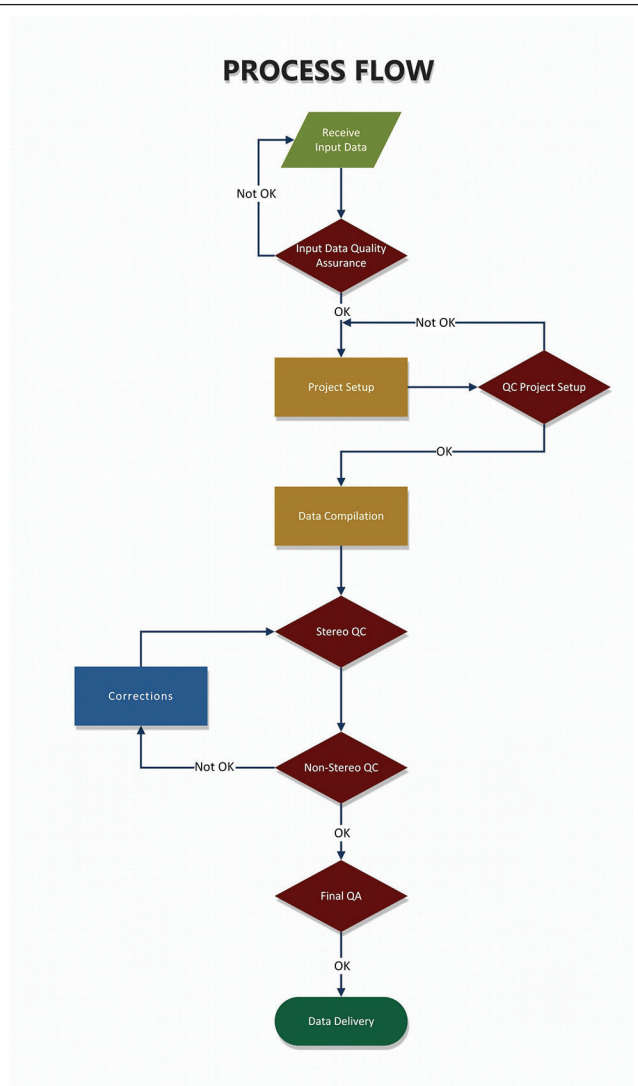
Figure 2. Process flow.

● Stereo QC

- Stereo QC is performed on all compiled models for interpretation, omissions, and any other compilation errors.
- Checking the compiled data for positional and elevation accuracies.
- Checking the data for the correct usage of data structure/feature classes.
- Checking the edge match of the compiled model with adjacent models.
- Generating contours at 1-meter interval and checking for DTM quality.

● Non-Stereo QC

- Verify model limits, buffer limits, and area limits to check completeness.
- Check for data connectivity and continuity between adjacent stereo models.
- Perform automated topological checks for overlaps, gaps, duplicates, etc., and perform corrections where required.
- Ensure uniform height in closed water polygons.

● Metadata Creation

The Federal Geographic Data Committee's (FGDC) Content Standard for Digital Spatial Metadata (CSDGM) is a well-known metadata standard that is being used around the world. With ArcGIS 10, the metadata editor is capable of creating and publishing FGDC CSDGM metadata. Information such as Data Quality Information, Spatial Reference Information, Entity and Attribute Information, Distribution Information, Time Period Information, Contact Information, etc., are embedded into the metadata file.
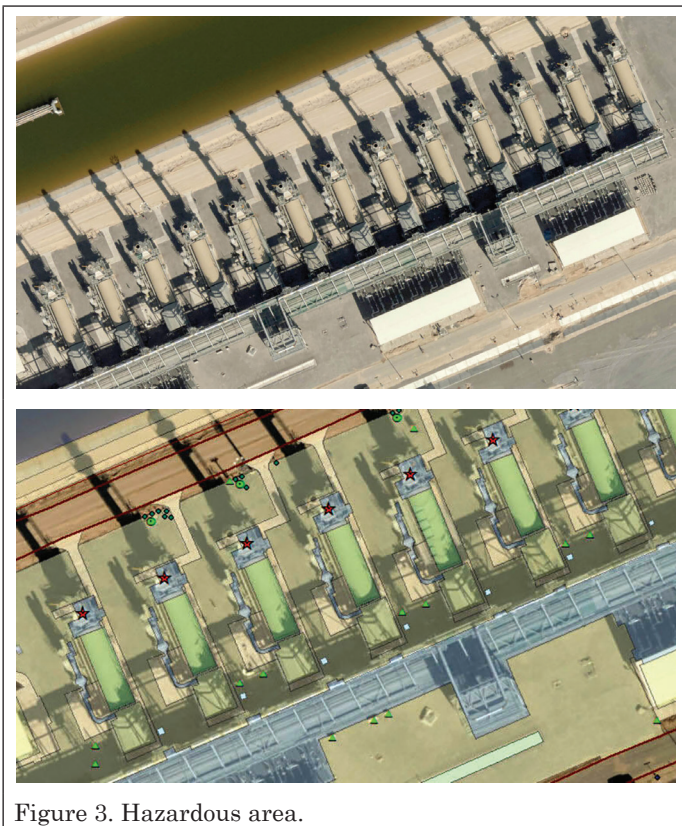
Figure 3. Hazardous area.

● Advantages of Photogrammetric Data Compilation Over Land Survey

1. Data compilation in hazardous areas- The upstream process of oil and gas production in KOC involves several steps starting from exploration, extraction to production of crude oil and natural gas. One of the activities during production of crude oil is to burn gases that usually accompany oil. This process is called flaring. The area around smokestacks or flares have high level of toxic gases making it hazardous for the surveyors to be exposed to. However, this vital infrastructure must be mapped and the information included in the database. Mapping data through photogrammetry techniques allows this in a safer and faster way without having to physically visit areas with high levels of toxins. An illustration of one such area is shown in Figure 3.

2. Data compilation within inaccessible areas- The vital installations of KOC are often secured by a fence and require special permission for access. Also, these areas are not always accessible due to security reasons. Mapping assets within such installations through land survey techniques poses a challenge. In order to obtain information in these areas, photogrammetry techniques are used (See Figure 4).

3. Data collection in a faster way- Features such as pipelines over large areas would require surveyors to spend more time in the field collecting the data. Whereas, the same data, when collected photogrammetrically, saves a significant amount of time. To quantify the efforts, photogrammetry compilation takes about 30% of the time in comparison to field survey. The surveyors could use the vector data and update the attribute information thus saving several man-hours.

4. Creation of DTM- Compiling data photogrammetrically enhanced the creation of an accurate digital terrain model by delineating hard and soft breaklines; such as ridge lines, hilly areas, wadis, drains, hydrographic features, etc. The DTM thus created, is used to create contours on the fly and terrain information is updated in areas where the DTM does not accurately represent the ground.

● Conclusion

Photogrammetry data compilation has helped KOC in optimizing their use of human resources to a great extent. In addition to mapping the KOC field assets faster, it also helps in keeping the working environment safe for the surveyors. This is done by mapping KOC assets photogrammetrically in hazardous and inaccessible areas, which would otherwise be not possible for the surveyors. It can be argued that the data compiled photogrammetrically would be less accurate in comparison with the field survey data. However, the purpose of this exercise was to fill in the missing information within hazardous and inaccessible areas which would be adequate for infrastructure planning purposes. The collected data was updated in the central enterprise geodatabase.

| Data collected by field survey | Additional data collected photogrammetrically | Dry Oil Lake |

Figure 4. Inaccessible areas.
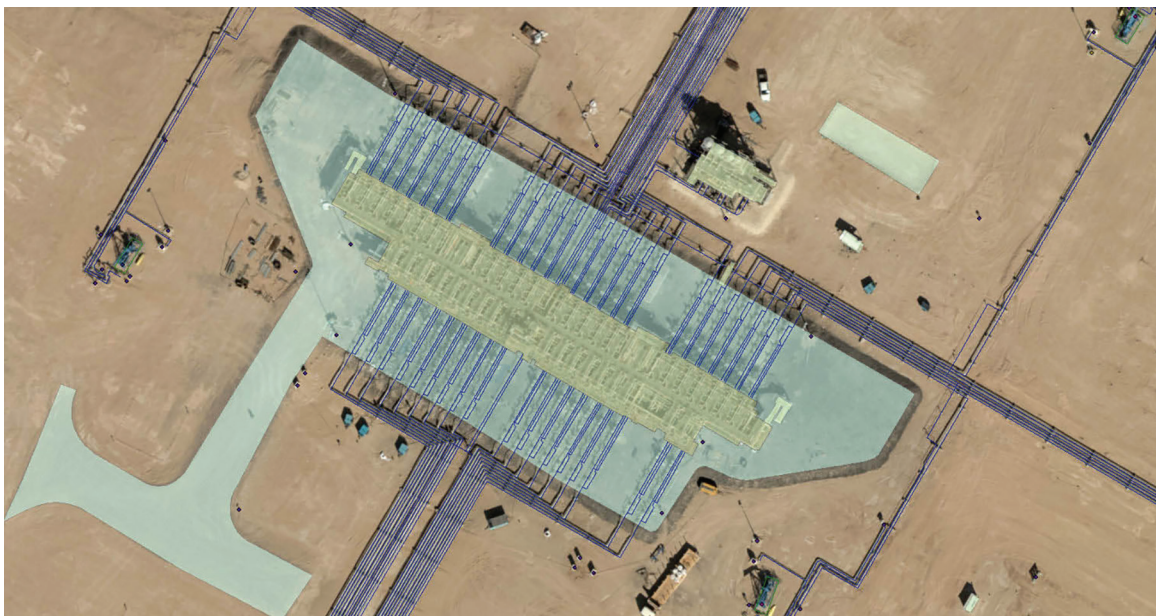
Figure 5. An example of pipelines over large areas.

PUBLISHING OPEN-ACCESS IN *PE&RS* IS NOW EASIER!

ASPRS is changing the subscription model of our monthly journal, *PE&RS*. ASPRS is waiving open-access fees for primary authors from subscribing institutions. Additionally, primary authors who are Individual Members of ASPRS will be able to publish one open-access article per year at no cost and will receive a 50% discount on open-access fees for additional articles.

- **Open Access matters!** By providing unrestricted access to research we can advance the geospatial industry and provide research that is available to everyone.

- **Institutions and authors receive more recognition!** Giving permission to everyone to read, share, reuse the research without asking for permission, as long as the author is credited.

- **Reputation matters!** Known for its high standards, *PE&RS* is the industry leading peer-review journal. Adding open access increases authors' visibility and reputation for quality research.

- **Fostering the geospatial industry!** Open access allows for sharing without restriction. Research is freely available to everyone without an embargo period.

Under the previous subscription model, authors and institutions paid $1500 or more in open-access fees per article. This will represent a significant cost savings. Open-access publications benefit authors through greater visibility of their work and conformance with open science mandates of funding agencies.

Subscriptions asprs.org/subscribe
Membership asprs.org/membership

asprs THE IMAGING & GEOSPATIAL INFORMATION SOCIETY

GIS
Tips & Tricks

Al Karlin, Ph.D. CMS-L, GISP

Buffers Everywhere but Where You Want Them?

Here is yet another Tips & Tricks column that comes by way of my GIS/Map Making Class at the University of Tampa. About mid-way through the semester, after we have gone through discussion of map projections and coordinate systems, we start on introductory spatial analyses with the introduction of the "buffer". We construct buffers around points, lines, and polygons and use them to count objects within their limits.

In Figure 1, I started with some local hospitals (the blue "H"s) and Federal Qualified Health Centers (FQCHs: red crosses) in the Pittsburg, PA area (blue polygon). Then I constructed a 3-mile buffer (orange, semi-transparent ovals) around each hospital to analyze the number of FQCHs within 3 miles of the hospitals. The data originated from the US Census Bureau in geographic coordinates (not a projection system), so when I specified a 3-mile buffer radius, the buf-
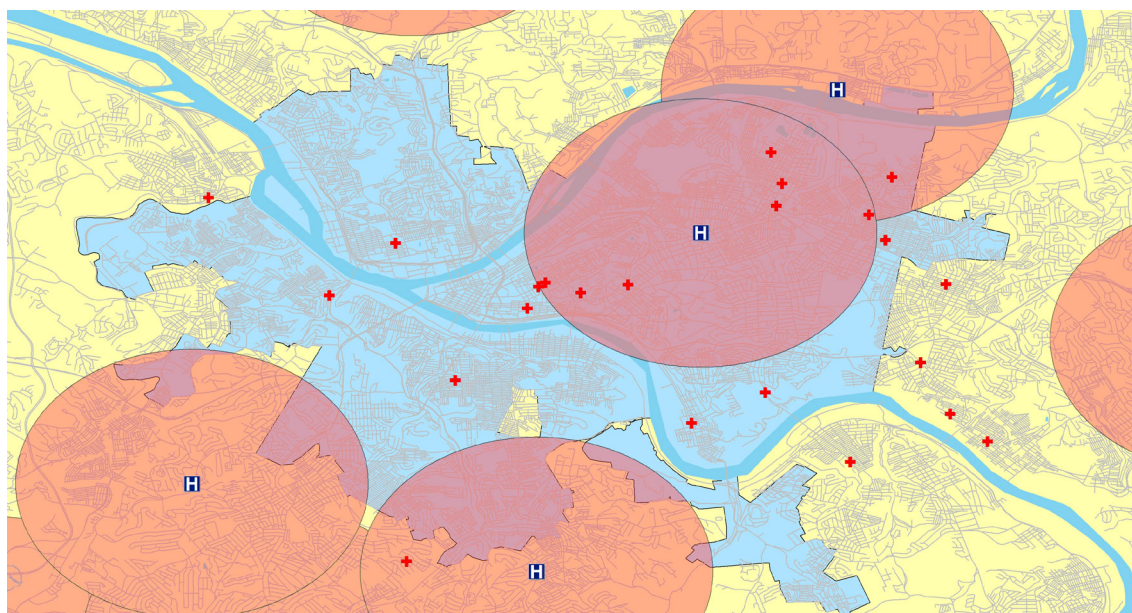
Figure 1. 3-mile Oval "buffers" around Hospitals resulting from the geographic coordinates (latitude/longitude) of the Hospital layer.

Creating buffers with any of the GIS software packages is easy; just find the tool (usually called, "Buffer"), identify the object to buffer, a buffer distance, set a few parameters (rounding, dissolved, etc.) and voila… a pretty instant spatial analysis. The buffer polygon can be used for spatial joins to count objects within, to select objects, and/or to clip other features. So, students gravitate to using and creating buffers for every analysis. However, in my classes, we generally start with some US Census Bureau data base map or some other layer that is in geographic coordinates, and therein lies the problem and this month's tip… Remember to change the coordinate system and projection before your make a buffer. The following example is from ArcGIS Pro 2.9, but the issues are similar with all GIS software programs.

fers appear as ovals with the major axis along the latitude and the minor axis along the latitude, in North America. This confuses students to no end; the buffers should be circles not ovals!

There are a few different approaches to making "circular" buffers, but they all revolve around having the data in a projected coordinate system. Hence, my GIS class does not make buffers until they understand projections.
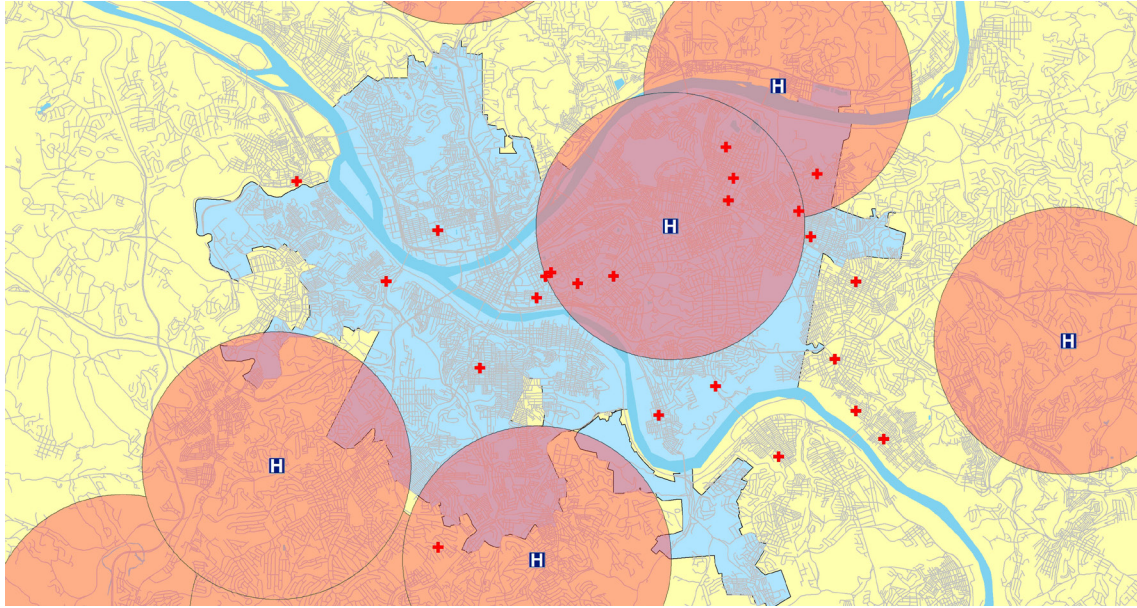
Figure 2. 3-mile circular "buffers" around Hospitals resulting from the projected coordinates (northings/eastings) of the Hospital layer.

TIP #1 — Project the source data BEFORE constructing the buffers. Most GIS software systems allow you to both specify a coordinate system (geographic or projected) for a data layer. In this case, the data layer should be defined as Geographic Coordinates with the North American Datum of 1983 (NAD83) or North American Datum of 1983 (2011). At most scales, the difference is negligible for our purposes. Then constructing the buffer using the appropriate geoprocessing tool will result in circular buffers as in Figure 2. In this case, I projected the geographic data into the Pennsylvania State Plane South (NAD 1983 (2011) FIPS 3702 (US Feet) coordinate system.

TIP #2 — Although not a preferred method, if you choose to maintain the DATA (point locations, buffers, etc.) in geographic coordinates, then you will get the same resulting map if you change the Data Frame coordinate system to the projected system. While the results will look the same, remember that distances may not be preserved by any on-the-fly projection calculations. So, for a "quick and dirty" map, just change the data frame coordinate system, but remember that the DATA are still in geographic coordinates.

Send your questions, comments, and tips to GISTT@ASPRS.org.

Al Karlin, Ph.D., CMS-L, GISP is with Dewberry's Geospatial and Technology Services group in Tampa, FL. As a senior geospatial scientist, Al works with all aspects of Lidar, remote sensing, photogrammetry, and GIS-related projects. He also teaches beginning map making at the University of Tampa.
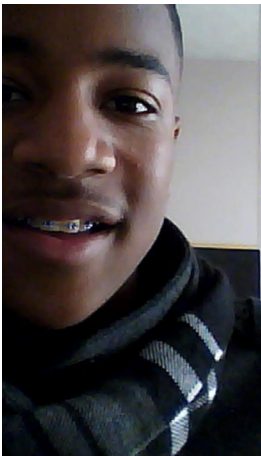
Brian Huberty, *SharedGeo*

Great Lakes Remote Sensing: Binational, Petascale, Wetlands and Habitats Change Mapping

History

This Sector Insight article is based on international cooperation and shared geospatial data – all without a major exchange of international funding. This approach for sharing data and resources, across an international border, can be applied to almost any large area or complex monitoring program – as demonstrated here.

The seeds for this project were planted in the 1990's by the Great Lakes Information Network or GLIN (https://www.glc.org/glin). Roger Gauthier, with the Great Lakes Commission, led a series of Regional Data eXchange (RDX) Conferences with the goal of fostering the exchange of geospatial data between Canada and the US.

In 2010, the author was granted a Radarsat-2 data grant from the Canadian Space Agency SOAR Program to investigate the use of satellite imagery for wetland mapping in collaboration with the University of Minnesota. This grant also reignited a collaboration with Dr. Brian Brisco with the Canada Centre for Remote Sensing (CCRS). In 2015, I was sent to Ottawa to renew collaborations that grew out of the Great Lakes Information Network.

Significance

The Great Lakes make up about 84% of North America's freshwater surface area and about 21% of the world's freshwater surface area. The total surface area of the Great Lakes Basin is about 244,106 square kilometers (93,971 square miles), which is about 0.2% of the Earth's total surface area of about 510.1 million square kilometers (196.9 million square miles). In the future, when the freshwater Greenland and polar ice caps melt into the saltwater oceans, the 21% of the planet's freshwater surface area increases to about 50%. Thus making the Great Lakes System an important freshwater resource to monitor for future generations.

Wetlands are one of the most dynamic and significant landscape features which help store and filter freshwater flowing into the Great Lakes. Due to human and climate actions, Great Lakes citizens and government leaders are observing rapid change in both interior and coastal wetland habitats around the Great Lakes Basin. Government, business and academic stakeholders are asking for rapid, seasonal views of the basin where they can take direct action to fix these problems.

Satellite and aerial images are essential tools used to track and observe wetland and associated habitat changes over time for large areas like the Great Lakes Basin. These images can come from a variety of optical, RADAR, lidar and SONAR sensors which now require petascale computing to ingest and process derived products due to the frequency of collection and the higher resolution of the sensors.

Glars Project

Starting in 2016, the University of Minnesota, Michigan Tech University, Minnesota Department of Natural Resources, SharedGeo.org, the Canada Centre for Remote Sensing and Environment and Climate Change Canada joined forces to develop a set of complex wetland and surface water mapping products led by the U.S. Fish & Wildlife Service and funded by the Great Lakes Restoration Initiative. With significant Blue Waters supercomputer support from the National Science Foundation, MAXAR commercial satellite imagery was accessed and processed via the National Geospatial-intelligence Agency (NGA) NextView Program. The team was able to process and create a variety of remote sensing demonstration products across pilot areas as well as the entire Great Lakes Basin.

For example, all available, stereo, sub-meter, MAXAR optical satellite imagery for the Great Lakes Basin were processed to create 2-meter surface vegetation elevation models as depicted in Figure 1.

The optical stereo satellite imagery were also classified for a variety of wetland derived products over a dozen pilot sites as depicted in Figure 2.

Figure 2 shows the pre- and post-herbicide treatment of Phragmites Australis (an invasive plant), from 2016 to 2017 near Saginaw, Michigan, using high-resolution MAXAR satellite imagery. The lower right map derived from the 7/19/2017 satellite image shows a dark purple triangular shaped area in the upper left portion of the map that was

Figure 1.

missed with herbicide treatment from the previous year. This example illustrates how land managers can be more accurate with treating wetlands to help eradicate an invasive plant.

Figure 3, taken between Michigan and Ontario, northeast of Detroit, of monthly Radarsat-2 images were collected and processed from 2016 through 2021. The objective was to show the dynamic water level rise over this six-year period as well as the duration of water saturation which is defined as a hydroperiod. A variety of fish and wildlife habitats are linked to these saturation zones.
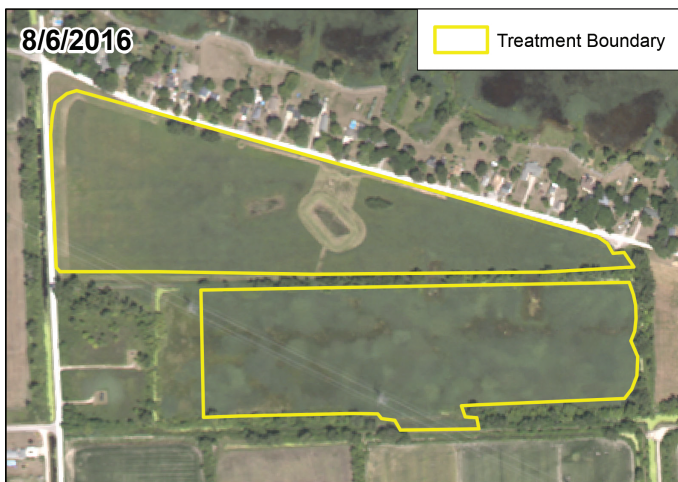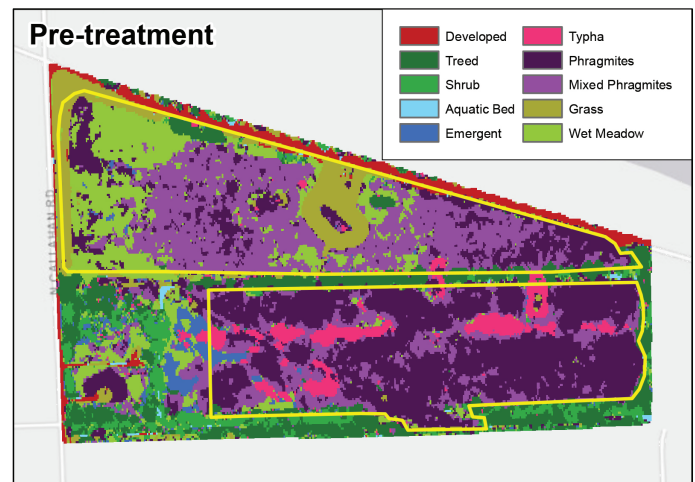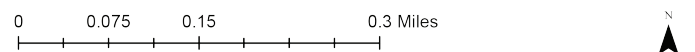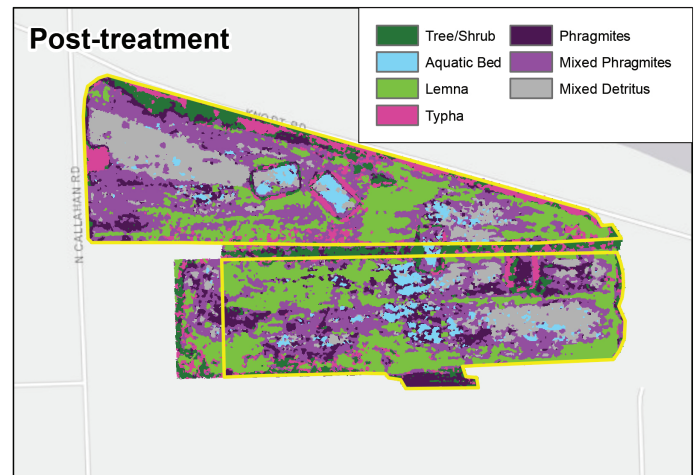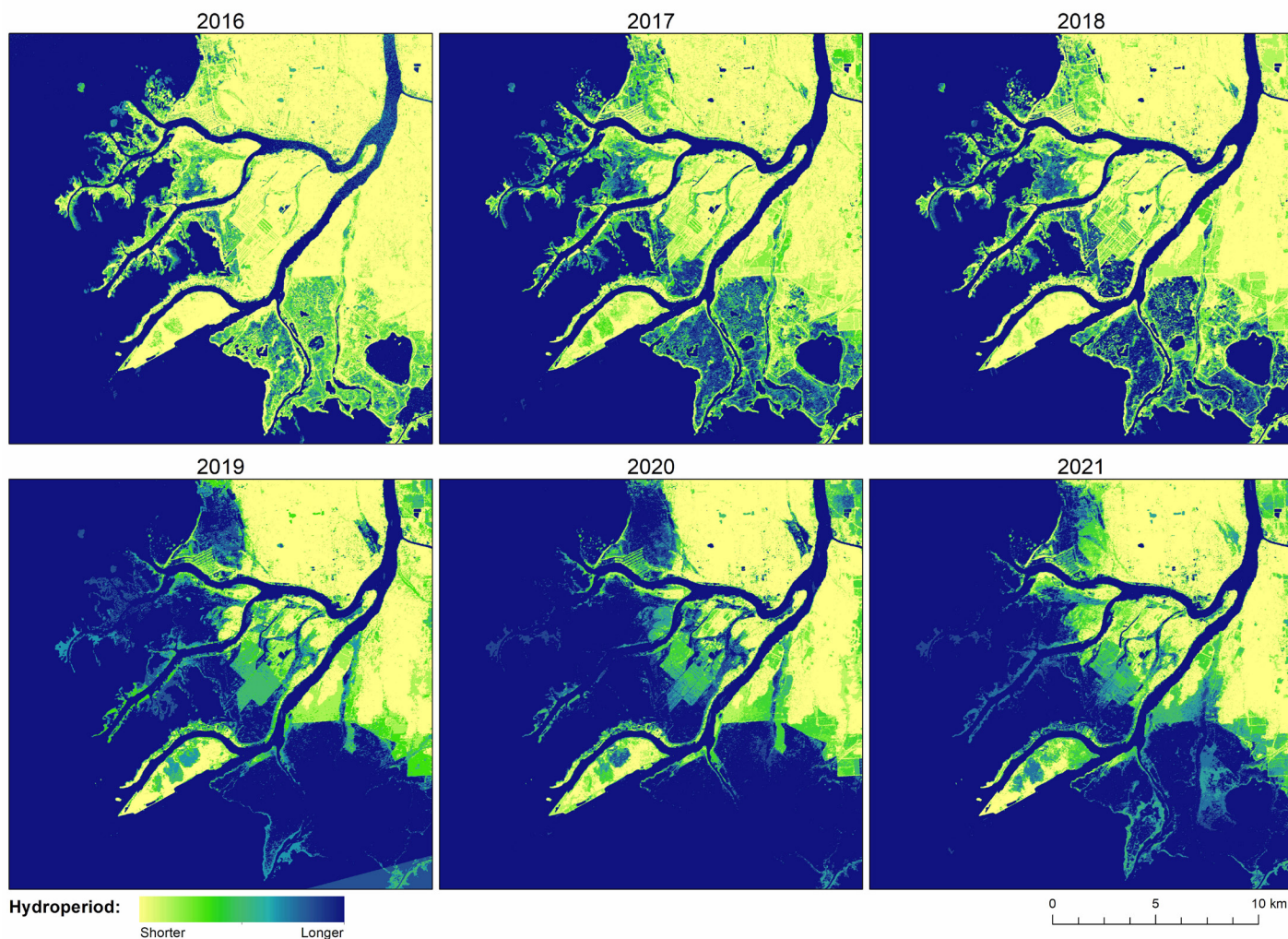
Figure 2.

Figure 3.

What is the Future for Great Lakes Remote Sensing?

As a consequence of this project, the Great Lakes Alliance for Remote Sensing (GLARS) was formed to help further binational remote sensing of the Great Lakes and data distribution. The examples shown in this Sector Insight article can all be accessed at https://glars.org.

The Great Lakes Restoration Initiative funded this project to demonstrate the next generation tools from optical and radar imagery for submeter, high resolution, multi-temporal image products. The challenge for the future will be to develop this into a binational program to monitor and sustain the Great Lakes. Such an approach as this results in good, solid applications based on teamwork and cooperation rather than competition. Given the importance of the Great Lakes to Canada, the US, and the planet, it should be expected that this work will lead to an on-going, dedicated program.

Dedication

This column is dedicated to the late Dr. Brian Brisco, Canada Centre for Remote Sensing, Natural Resources Canada. Unfortunately, Brian passed away in September of 2022 after bravely battling illness for many years. Brian led the CCRS research and development for radar research and applications for surface and water features. His interest is not surprising since he was an avid muskie fisherman and duck hunter. Brian was the recipient of the Canadian Remote Sensing Society's Larry Morley Gold Medal Award in 2017.

Author

Brian Huberty is an ASPRS Certified Mapping Scientist who is currently assisting SharedGeo (a geospatial non-profit) with a variety of remote sensing projects. Over the last four decades, he has applied remote sensing and geospatial assessment technologies for the Minnesota Department of Natural Resources, USDA Forest Service, USDA Natural Resources Conservation Service, U.S. Geological Service and the U.S. Fish & Wildlife Service. Mr. Huberty has B.S. and M.S. degrees from the University of Minnesota, College of Natural Resources specializing in geospatial resource inventory systems. Brian has held leadership positions within ASPRS and ISPRS.

Coordinate Systems of the World

Datums and Grids

Clifford J. Mugnier

A comprehensive consolidation of data for the world, this book gives a short precis of each nation, each nation's history, its topography and a chronology of the development of geodetic surveying and coordinate systems for that specific nation. A starting point of information for understanding the world's datums and grids.

Hb: 978-1-032-31034-3 | $176.00

TABLE OF CONTENTS:

For more details, or to request a copy for review, please contact: https://m.email.taylorandfrancis.com/review-copy-request-form

CRC Press
Taylor & Francis Group

Taylor & Francis Group
an **informa** business

For more information visit:
www.routledge.com/9781032310343

ASPRSNEWS

PE&RS' GRIDS & DATUMS COLUMN* IS NOW AVAILABLE AS A BOOK

Coordinate Systems of the World – Datums and Grids by Clifford J. Mugnier is a comprehensive consolidation of data based on the very popular Grids and Datums Column in *PE&RS*. This book provides a short precis of each country's history, topography, and a brief chronology of the development of their geodetic surveying and coordinate system.

Coordinate Systems of the World – Datums and Grids was published by CRC Press, a Taylor & Frances Group and, for a limited time only is available at a discounted rate of $176. See page 208 for more information about this book and how to order.

*The contents of the Grids & Datums Column reflect the views of the author, who is responsible for the facts and accuracy of the data presented herein. The contents do not necessarily reflect the official views or policies of the American Society for Photogrammetry and Remote Sensing and/or the Louisiana State University Center for GeoInformatics (C^{4}G).
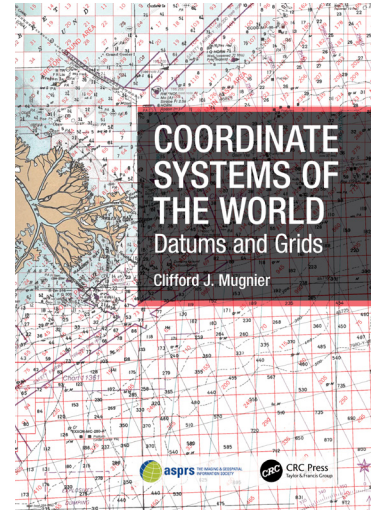
NEW ASPRS MEMBERS

ASPRS would like to welcome the following new members!

FOR MORE INFORMATION ON ASPRS MEMBERSHIP, VISIT
HTTP://WWW.ASPRS.ORG/JOIN-NOW

ASPRS' MAY GEOBYTE IS SCHEDULED FOR MAY 5TH

SeaSketch 2.0: A New, Free and Open-source Software Service for Map-based Surveys and Collaborative Geodesign
May 5th at 12 Noon ET

Originally launched in 2012, SeaSketch (www.seasketch.org) was developed to support the collaborative geodesign of marine spatial plans. Users can visualize dynamic maps, contribute information by way of map-based surveys, sketch and evaluate prospective zones (such as marine protected areas), and share designs in interactive forums. The new version of SeaSketch, available in the first quarter of 2023, substantially benefits users through new and improved functionality including (1) mobile / table compatibility, (2) vector-based map rendering to improve performance, (3) capabilities for working offline, (4) data hosting, (5) built-in cartographic tools and (6) an entirely free and open-source code base. I will demonstrate the core user-facing and administrative tools, drawing from a number of ongoing participatory mapping projects using SeaSketch on a national scale. Attendees will learn the basics for creating their own bespoke SeaSketch projects.

Presented by Will McClintock, Ph.D., Will McClintock is a marine scientist at the National Center for Ecological Analysis and Synthesis (NCEAS) within the University of California Santa Barbara (UCSB). He has over 20 years of experience developing and implementing software tools for marine spatial planning (MSP), conservation and fisheries management. As a member of the Blue Prosperity Coalition, he is currently supporting MSP in The Maldives, The Azores, Bermuda, Samoa, Fiji and other geographies. Other past and ongoing project locations include the US, UK, Canada, New Zealand, Norway, The Cook Islands, Gyana, Reunion, Indonesia and Australia. He received a B.A. in Biology from Earlham College, M.S. in Behavioral Ecology from the University of Cincinnati, M.A. in Counseling Psychology from Pacifica Graduate Institute, and a Ph.D. in Ecology, Evolution and Marine Biology from UCSB.

All live GeoBytes are complimentary to everyone—Register at www.asprs.org/geobytes.html

---

ASPRS Staff Directory

Membership/*PE&RS* Subscription/ Conferences
Yuki Day
office@asprs.org

Advertising/Exhibit Sales
Bill Spilman
bill@innovativemediasolutions.com

Peer-Review Article Submission
Alper Yilmaz
PERSeditor@asprs.org

Highlight Article Submission
Jie Shan
jshan@ecn.purdue.edu

Feature Article Submission
Featureeditor@asprs.org

Certification
applications@asprs.org

Calendar
calendar@asprs.org

ASPRS Bookstore
office@asprs.org

ASPRS Foundation
foundation@asprs.org

Mailing Address
PO Box 14713
Baton Rouge, LA 70898
301-493-0290, 225-408-4422 (fax)
www.asprs.org

ASPRS Workshop Series

It's not too late to earn Professional Development Hours

Miss one of our Live Online Workshops? You can purchase the workshops now and watch when you are ready!

Check out the workshops offered by visiting **https://asprs.prolearn.io/catalog**

A GPU-Accelerated PCG Method for the Block Adjustment of Large-Scale High-Resolution Optical Satellite Imagery Without GCPs

Qing Fu, Xiaohua Tong, Shijie Liu, Zhen Ye, Yanmin Jin, Hanyu Wang, and Zhonghua Hong

Abstract

The precise geo-positioning of high-resolution satellite imagery (HRSI) without ground control points (GCPs) is an important and fundamental step in global mapping, three-dimensional modeling, and so on. In this paper, to improve the efficiency of large-scale bundle adjustment (BA), we propose a combined Preconditioned Conjugate Gradient (PCG) and Graphic Processing Unit (GPU) parallel computing approach for the BA of large-scale HRSI without GCPs. The proposed approach consists of three main components: 1) construction of a BA model without GCPs; 2) reduction of memory consumption using the Compressed Sparse Row sparse matrix format; and 3) improvement of the computational efficiency by the use of the combined PCG and GPU parallel computing method. The experimental results showed that the proposed method: 1) consumes less memory consumption compared to the conventional full matrix format method; 2) demonstrates higher computational efficiency than the single-core, Ceressolver and multi-core central processing unit computing methods, with 9.48, 6.82, and 3.05 times faster than the above three methods, respectively; 3) obtains comparable BA accuracy with the above three methods, with image residuals of about 0.9 pixels; and 4) is superior to the parallel bundle adjustment method in the reprojection error.

Introduction

A large number of high-resolution optical satellites have been launched in the world and in China, such as SPOT-5 (Poli, Zhang, and Gruen 2004), IKONOS (Toutin and Cheng 2000), QuickBird (Noguchi *et al.* 2004), GeoEye (Fraser and Ravanbakhsh 2009), and Ziyuan-3 (ZY-3) (Tang *et al.* 2013; Jiang *et al.* 2015; Liu *et al.* 2016; Tong *et al.* 2015a; Tong *et al.* 2015b; Gong *et al.* 2017; Yang *et al.* 2017), which is China's first civil stereo surveying and mapping satellite. The ground resolution and geo-positioning accuracy of these systems are constantly being improved. The precise geo-positioning of high-resolution optical satellite imagery (HRSI) without ground control points (GCPs) is the premise for large-scale remote sensing mapping applications, including global mapping (Gong *et al.* 2017), three-dimensional modeling (Yang *et al.* 2017), and so on. However, there are two critical issues in large-scale block adjustment (BA) without GCPs: 1) how to improve the accuracy (Zhang *et al.* 2016; Chen *et al.* 2016; Wang *et al.* 2017; Ma *et al.* 2017; Jiao *et al.* 2018; Cao *et al.* 2019) of BA without GCPs; and 2) how to improve the calculation efficiency (Zhang *et al.* 2014; Zheng *et*

al. 2016; Gong *et al.* 2017; Yang *et al.* 2017; Wang *et al.* 2017; Sun *et al.* 2019) of large-scale BA.

The main HRSI systems, such as SPOT-5, IKONOS, and QuickBird, do not have a high accuracy of direct positioning (Zhang *et al.* 2016; Gong *et al.* 2017; Wang *et al.* 2017). The Rational Polynomial Coefficient (RPC) parameters contain obvious systematic errors, so that it is necessary to establish a corresponding error compensation model (Tao and Hu 2001; Fraser and Hanley 2005). Grodecki and Dial (2003) analyzed the systematic error of the RPC model and used an affine transformation model to correct the systematic errors; Zhang *et al.* (2016) improved the BA accuracy of SPOT-5 satellite images from 13.7 m to 5 m in the planar, and from 9 m to less than 5 m in the elevation; and Tong, Liu, and Weng (2009) studied a method of RPC systematic error correction and RPC parameter refinement and regeneration and assessed the accuracy of QuickBird satellite stereo images (Tong *et al.* 2010). In order to improve the BA accuracy of HRSI without GCPs, researchers have carried out a series of related studies. Yao *et al.* (2018) adopted a BA method based on repeated satellite images covering the same area, which improved the BA accuracy without GCPs. In addition, Pan *et al.* (2017) achieved better BA results by using other satellite image or aerial image with a higher geo-positioning accuracy as control information. Moreover, the geocoded information data, such as digital orthophoto models and digital elevation models (DEMs), can also be used as control data for the combined BA of satellite images (Zhang *et al.* 2016). For example, Zhou *et al.* (2018) used Shuttle Radar Topography Mission data to interpolate the elevation values of ground points corresponding to tie points as the initial adjustment values, which improved the BA accuracy, especially in the elevation direction. In addition, multi-source control information, such as synthetic aperture radar imagery (Zhang *et al.* 2021), high-precision optical satellite imagery (Pan *et al.* 2017), high geo-positioning aerial images (Song *et al.* 2021), or laser altimetry data (Jiao *et al.* 2018; Zhang *et al.* 2021) can also be introduced to carry out combined BA. Another approach is to use an independent model method (Chen *et al.* 2016), minimum height difference method (Chen *et al.* 2016), or other methods to match a certain number of virtual control points between the original images and the public geographic information data to improve the BA accuracy without GCPs (Zhang *et al.* 2016; Chen *et al.* 2016; Tong *et al.* 2020).

Due to the large number of images in large-scale BA and the complex structure of BA networks, large-scale BA without GCPs needs further study in practical applications. For large-scale BA, scholars have carried out some related research, including optimizing the minimum bandwidth to reduce the memory consumption of the normal equation (Wang *et al.* 2017). Although there are some effective computing methods for matrix decomposition, the inversion of large matrices (Agullo *et al.* 2011), the memory consumption of the normal equation, and the BA computing efficiency are all issues that need to be solved. Among the different methods, Zheng *et al.* (2016) proposed

Qing Fu, Xiaohua Tong, Shijie Liu, Zhen Ye, Yanmin Jin, Hanyu Wang, and Zhonghua Hong are with the College of Surveying and Geo-informatics, Tongji University, Shanghai 200092, China (xhtong@tongji.edu.cn).

Qing Fu is also with the School of Electronics and Information Engineering, Jinggangshan University, Ji'an 343009, China.

Zhonghua Hong is also with the College of Information Technology, Shanghai Ocean University, Shanghai, 201306, China.

a method based on DEM-assisted BA to improve the mapping accuracy for large numbers of images, and they carried out a BA experiment using ZY-3 and GF-1 images covering Jiangxi province of China. D'Angelo and Reinartz (2012) presented rational function model (RFM) to improve the BA accuracy of 414 pairs of CartoSat-1 stereo images covering northern Italy; Zhang *et al.* (2014) used the rigorous imaging geometry model to carry out a BA experiment without GCPs for ZY-3 three-line array (TLA) stereo images with a maximum length of 3000 km, in which, compared with the geo-positioning accuracy of forward intersection, the BA accuracy without GCPs for the ZY-3 satellite was greatly improved, reaching a planar accuracy of 8.3 m and an elevation accuracy of 5.0 m; Wang *et al.* (2017) used a conjugate gradient (CG) method to estimate the BA results, and a BA experiment without GCPs for 8802 ZY-3 TLA stereo images covering the whole of mainland China was carried out, which needed only two iterations to converge and cost about 15 min on a standard computer for the BA estimation (Gong *et al.* 2017; Yang *et al.* 2017); and Sun *et al.* (2019) proposed a multi-threaded parallel computing method based on RFM, which uses the OpenMP parallel computing method, and the time cost of the BA estimation was less than 7.5 min for the experimental area covered by 5241 ZY-3 satellite images. However, BA model estimation is still a time-consuming task in HRSI without GCPs, especially in the large scale. Furthermore, relatively few studies have combined the Preconditioned Conjugate Gradient (PCG) and Graphic Processing Unit (GPU) parallel computing methods for the large-scale BA of HRSI without GCPs.

In recent years, with the development of high-performance parallel GPU computing devices, the application of GPUs has not been confined to the field of the graphics display. Many CPU computing tasks can also be accomplished with parallel GPU computing devices, and GPUs can provide a computing performance that is tens or even hundreds of times faster than that of a CPU in the Single Instruction Multiple Data operations. As a result, GPU devices have been widely used in the field of high-performance computing for non-graphical displays. Before this, there had been lots of research work on BA using GPU devices in the computer vision community (Agarwal *et al.* 2010; Choudhary, Gupta, and Narayanan 2010; Wu *et al.* 2011; Liu, Gao, and Hu 2012; Hänsch, Drude, and Hellwich 2016; Zheng *et al.* 2017), which mainly focused on close-range photogrammetric digital images and unmanned aerial vehicle images. Zheng *et al.* (2017) used a combined PCG and GPU computing method for the BA of a data set with about 4500 digital images from the Community Photo Collections (CPC) project, where nine million image points could be processed in only 1.5 minutes while achieving a subpixel accuracy. Combining PCG and a high-performance GPU parallel computing method for the large-scale BA of HRSI without GCPs faces with three main problems: 1) estimation of the BA based on the PCG method; 2) the memory consumption of the error equation based on the Compressed Sparse Row (CSR) (Nathan and Garland 2009) sparse matrix format; and 3) the GPU-accelerated PCG method for BA estimation.

Therefore, in this paper, we present a combined PCG and GPU parallel computing method for the large-scale BA of HRSI without GCPs. In the proposed approach, the PCG method is used to calculate the unknown parameter results after BA model construction, which avoids the direct inversion of the design matrix of the normal equation. In addition, the CSR sparse matrix format is used to reduce the memory consumption of the normal equation, especially for large-scale BA experiments, and the combined PCG and GPU parallel computing method is used to further improve the computational efficiency of the BA model.

Methodology

Figure 1 shows the overall technical flowchart of the proposed BA method, i.e., the combined PCG and GPU parallel computing method for the large-scale BA of HRSI without GCPs, which consists of three main components, as follows:

(1) Construction of the BA model based on RFM, which is the premise of large-scale BA estimation for HRSI without GCPs.
(2) The PCG method is used to calculate the normal equation, the CSR sparse matrix format is used to save the memory consumption, and to accelerate the matrix operations of the correlation coefficients.

(3) The combined PCG and GPU parallel computing method is adopted to improve the efficiency of the whole BA estimation process.

Construction of the BA Model Based on RFM Without GCPs

The Rational Function Model
The imaging geometric model represents the geometric physical relationship between the image point coordinates and the ground point coordinates, which is the prime of the high-precision geo-positioning of remote sensing images. RFM is a more general expression of the sensor model and is suitable for all kinds of sensors (Tong *et al.* 2010; Chen *et al.* 2016; Zhang *et al.* 2016; Gong *et al.* 2017; Yang *et al.* 2017). From a numerical calculation point of view, RFM can be understood as a functional relationship, with the ground point coordinates as the independent variables and the image point coordinates as the dependent variables. The basic form is shown in Equation 1 (Tao and Hu 2001; Grodecki and Dial 2003; Fraser and Hanley 2005):

$$\begin{cases} r_n = \dfrac{\mathrm{Num}_L\left(P_n, L_n, H_n\right)}{\mathrm{Den}_L\left(P_n, L_n, H_n\right)} \\[2mm] c_n = \dfrac{\mathrm{Num}_L\left(P_n, L_n, H_n\right)}{\mathrm{Den}_L\left(P_n, L_n, H_n\right)} \end{cases} \tag{1}$$

where the dependent variable (r, c) represents the normalized image point coordinates in the scan direction and flight direction, and the independent variable (P, L, H) represents the normalized ground point coordinates. Num_L, Den_L, Num_S, and Den_S are general polynomials for different combinations of (P, L, H). In a polynomial, the power of each independent variable is no more than three, and the sum of the independent variables' power is also no more than three (Tao and Hu 2001; Grodecki and Dial 2003). Therefore, each polynomial is the sum of 20 different combinations of independent variables. The coefficients of the four polynomials and the normalized coefficients constitute the RFM coefficients (RPC) (Fraser and Hanley 2005; Tong *et al.* 2010).

Normalizing can improve the stability of solving the RFM coefficients and is used to reduce the data rounding errors caused by the large difference of the data series in the calculation procedure (Tong *et al.* 2010; Zhang *et al.* 2016; Gong *et al.* 2017; Yang *et al.* 2017). Normalizing is achieved by a translation and scaling procedure. The normalized equation is shown in Equation 2 (Tao and Hu 2001; Grodecki and Dial 2003; Fraser and Hanley 2005):

$$r_n = \frac{r - r_0}{r_s}, c_n = \frac{c - c_0}{c_s}$$

$$P_n = \frac{P - P_0}{P_s}, L_n = \frac{L - L_0}{L_s}, H_n = \frac{H - H_0}{H_s} \tag{2}$$

where r_0, c_0, P_0, L_0, H_0 are the normalized translation parameters, and r_s, c_s, P_s, L_s, H_s are the normalized scaling coefficients.

Construction of the BA Model Without GCPs
The systematic errors of the RFM are corrected by the additional compensation model in the image space (Tong *et al.* 2010; Zhang *et al.* 2016; Gong *et al.* 2017; Yang *et al.* 2017). Equation 1 can then be rewritten as:

$$\begin{cases} r + \Delta r = \dfrac{Num_L\left(P, L, H\right)}{Den_L\left(P, L, H\right)} \\[2mm] c + \Delta c = \dfrac{Num_s\left(P, L, H\right)}{Den_s\left(P, L, H\right)} \end{cases} \tag{3a}$$

$$\begin{cases} \Delta r = a_0 + a_1 r + a_2 c \\ \Delta c = b_0 + b_1 r + b_2 c \end{cases} \tag{3b}$$

where Δr, Δc are the systematic error correction parameters of the optical satellite imagery in the scan and flight directions, respectively; and (a_0, a_1, a_2, b_0, b_1, b_2) are the compensation parameters of the systematic
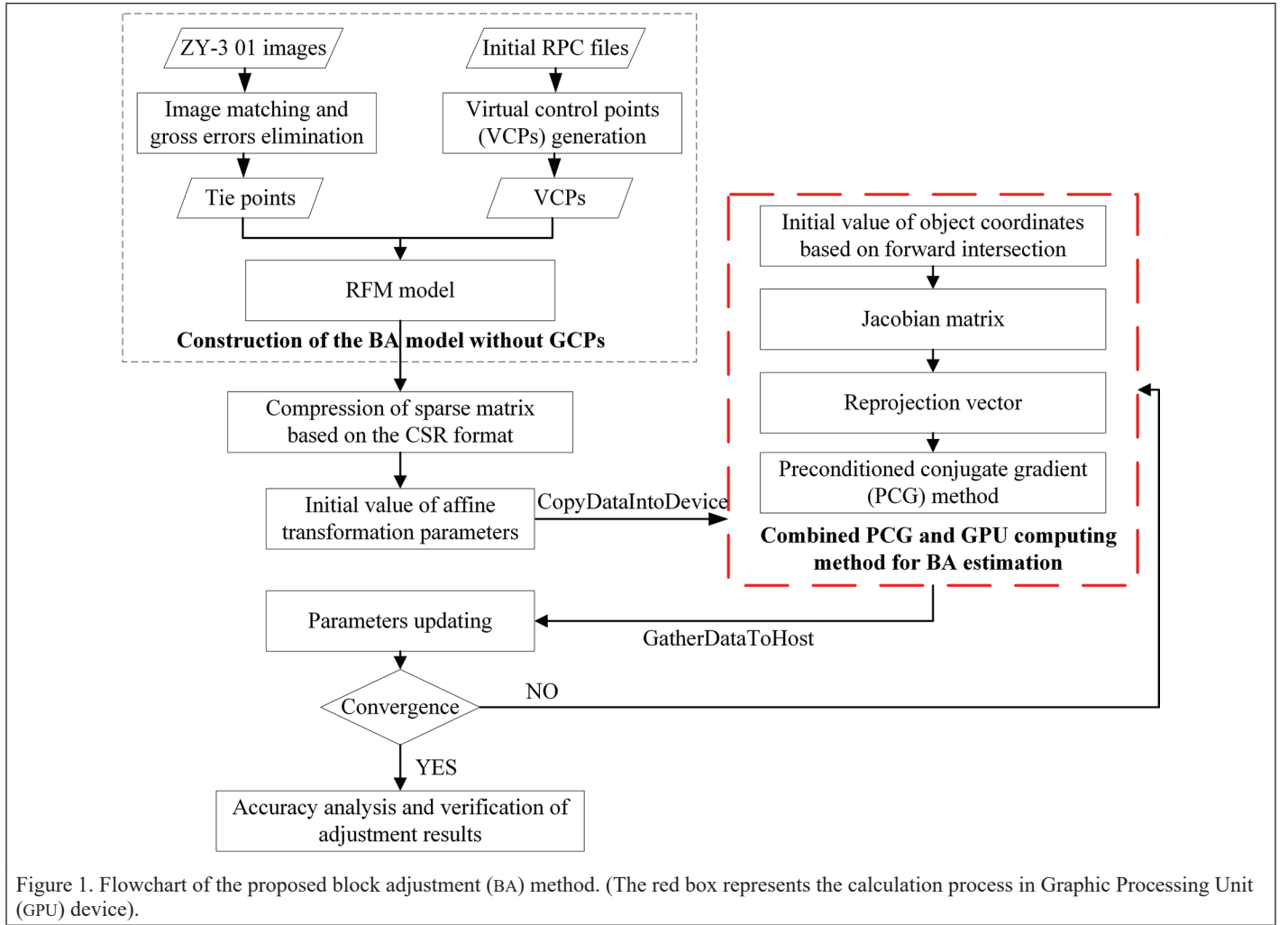
Figure 1. Flowchart of the proposed block adjustment (BA) method. (The red box represents the calculation process in Graphic Processing Unit (GPU) device).

errors. a_0 and b_0 are mainly used to compensate the system offset errors caused by model drift. a_1 and b_1 can be approximated to eliminate the model scanning direction errors caused by roll attitude. a_2 and b_2 can be used to eliminate the flight direction errors caused by pitch attitude (Tao and Hu 2001; Grodecki and Dial 2003). Due to the imaging characteristics of satellite platforms, the attitude compensation values are usually small (Fraser and Hanley 2005; Tong *et al.* 2010).

Equation 3a can be linearized by Taylor series expansion (Grodecki and Dial 2003), the matrix form is as follows:

$$V = At + Bx - L, P \quad (4)$$

where **V** represents the residual error vectors of the tie point measurements in the scan and flight directions; **A**, **B** are the corresponding coefficient matrices; **x** represents the correction vectors of the ground point coordinates corresponding to the tie points; **t** represents the correction vectors of the systematic error; **L** is the constant vector calculated from the initial value; and **P** represents the corresponding weight matrices.

According to the theory of least squares, the observed error equation can be further modified. Equation 4 can then be written as:

$$\begin{bmatrix} \mathbf{A^TPA} & \mathbf{A^TPB} \\ \mathbf{B^TPA} & \mathbf{B^TPB} \end{bmatrix} \begin{bmatrix} \mathbf{t} \\ \mathbf{x} \end{bmatrix} = \begin{bmatrix} \mathbf{A^TPL} \\ \mathbf{B^TPL} \end{bmatrix} \quad (5)$$

The normal equation matrix described in Equation 5 is a symmetric banded matrix. Therefore, in the BA estimation procedure, because there are too many unknowns, it is necessary to separate the affine transformation coefficients from the coordinate corrections of the ground points. In other words, we first eliminate a class of unknowns

(generally the coordinate corrections of ground point **x** (Gong *et al.* 2017; Yang *et al.* 2017)), and we obtain the modified normal equation containing only the parameters of the affine transformation coefficients **t**. After eliminating **x**, the solution of **t** can be shown as:

$$\mathbf{N_t} \times \mathbf{t} = \mathbf{R_t} \quad (6)$$

where $\mathbf{N_t} = \mathbf{A^TPA} - \mathbf{A^TPB} \times (\mathbf{B^TPB})^{-1} \times \mathbf{B^TPA}$ is the Schur complement matrix, which is a symmetric matrix, $\mathbf{N_t} = \mathbf{A^TPL} - \mathbf{A^TPB} \times (\mathbf{B^TPB})^{-1} \times \mathbf{B^TPL}$.

After calculating the corrections of the affine transformation parameters of each image, according to the calculation results of the modified normal equation, the corrections of the ground point coordinates **x** corresponding to the tie points are solved by replacing the normal Equation 5, and then the solution of **x** can be shown as:

$$\mathbf{x} = (\mathbf{B^TPB})^{-1} \times (\mathbf{B^TPL} - \mathbf{B^TPA} \times \mathbf{t}) \quad (7)$$

The BA solution is an iterative procedure. When the results of two BA solutions are less than the set threshold, the iterative procedure is stopped (Chen *et al.* 2016; Gong *et al.* 2017; Yang *et al.* 2017; Tong *et al.* 2020).

In addition, the virtual control points are generated from the initial RPC files in a regular grid (Yang *et al.* 2017).

Estimation of the Modified Normal Equation Based on Sparse Matrix and PCG Method

Storage and Compression of the Sparse Coefficient Matrix
The coefficient matrix of the normal equation in the large-scale BA model has obvious sparsity. For the large-scale sparse matrix, if a full-matrix

storage format is used to store the dense matrix, its storage requirement and computational time cost will be very high, and it will cost lots of unnecessary memory space. If a compressed storage format method is used to store the sparse coefficient matrix, it will not only reduce memory consumption, but will also reduce the computational time cost.

The common storage formats for sparse matrices include Coordinate (COO), Compressed Sparse Column, and Compressed Sparse Row (CSR) (Nathan and Garland 2009; Cheng, Tian, and Ma 2018). The COO format stores a sparse matrix by using the three arrays of values, rows, and columns index (colind), as shown in Figure 2a. CSR uses the three arrays of values, rows pointer (rowptr), and colind to store a sparse matrix, as shown in Figure 2b, which is suitable for the coefficient matrix storage and parallel matrix computing. At the same time, the value can be obtained from the row's pointer and columns index in the GPU device, respectively, then the sparse design matrix stored in the CSR format can better meet the characteristics of GPU parallel computing. In this study, we used the CSR storage format to compress the sparse design matrix of the modified normal equation.

Estimation of the Modified Normal Equation Based on the PCG Method
The CG method can make full use of the sparsity of the normal matrix and can be calculated without pre-estimating other parameters. In addition, the calculation required in each iteration is mainly the operation between vectors, which is convenient and easy for parallelization. The convergence speed of the CG method is closely related to the condition number of the design matrix (Zheng *et al.* 2017). The CG method can obtain high-precision approximate calculation results in fewer iterations. However, when the condition number of the design matrix is very large, the convergence speed is very slow. In the preconditioned conjugate gradient (PCG) method, after introducing the preconditioner matrix $\mathbf{M}$ through an appropriate preconditioning method, the eigenvalue distribution of the matrix is more centralized and the condition number of the design matrix is greatly reduced, so as to further improve the convergence speed. The PCG method is a very effective and efficient iterative method for solving large-scale sparse linear equations (Peng, Liu, and Wei 2021).

There are many preconditioning methods for symmetric positive definite linear equations, such as the diagonal preconditioner matrix (Wathen and Silvester 1993), the Jacobi preconditioning method (Byröd and Åström 2010), incomplete matrix decomposition (Bru and Tůma 2008), the multi-scale preconditioning matrix (Byröd and Åström 2009), etc. However, there is no general method that can be used to all the computational problems in which the condition number of the sparse design matrix is obviously different. The PCG method does not need to decompose the coefficient matrix, which can effectively reduce the memory consumption and improve the computational efficiency. The block Jacobi preconditioning matrix (Wu *et al.* 2011) is very simple, easy to calculate, and the preconditioned matrix is very stable, which satisfies the selection principle of the preconditioned matrix. Therefore, in this study, the block Jacobi preconditioning matrix was used to estimate the normal equation for the large-scale BA.

In Equation 6, $\mathbf{N}_t$ is an *n*-order positive definite symmetric matrix, and $\mathbf{t}$ and $\mathbf{R}_t$ are *n*-dimensional column vectors. If $\mathbf{M}$ is a preconditioner matrix, the PCG method is listed in Algorithm 1.

Algorithm 1: The preconditioned conjugate gradient (PCG) method
For $k = 0$;   Initial parameters: $\mathbf{t}^{(0)} = 0$, $\mathbf{r}^{(0)} = \mathbf{R}_t - \mathbf{N}_t \mathbf{t}^{(0)}$, $\mathbf{d}^{(0)} = \mathbf{M}^{-1} \mathbf{t}^{(0)}$
do   1: $\alpha^{(k)} = \mathbf{r}_k^T \mathbf{M}^{-1} \mathbf{r}^{(k)} / \mathbf{d}_k^T \mathbf{N}_t \mathbf{d}^{(k)}$ 2: $\mathbf{t}^{(k+1)} = \mathbf{t}^{(k)} + \alpha^{(k)} \mathbf{d}^{(k)}$ 3: $\mathbf{r}^{(k+1)} = \mathbf{t}^{(k)} + \alpha^{(k)} \mathbf{d}^{(k)}$ 4: $\beta^{(k)} = \mathbf{r}_{k+1}^T \mathbf{M}^{-1} \mathbf{t}^{(k+1)} / \mathbf{r}_k^T \mathbf{M}^{-1} \mathbf{r}^{(k)}$ 5: $\mathbf{d}^{(k+1)} = \mathbf{M}^{-1} \mathbf{r}^{(k+1)} + \beta^{(k)} \mathbf{d}^{(k)}$ 6: $k = k + 1$ while $\mathbf{d}^{(k)2} > \varepsilon$ Return $\mathbf{t}^{(k+1)}$

If the value of $\mathbf{d}^{(k)2}$ is within a predetermined threshold, the iterative procedure is stopped; otherwise, go to step 1.

The Combined PCG and GPU Computing Method for BA Estimation
The problem of BA estimation mainly includes the calculation of reprojection error, Jacobian matrix, preconditioner matrix, and multiplication between matrix and vector.

GPU Accelerated BA Parallel Computing Optimization Method
(1) *Parallel computation optimization of the reprojection errors* $\mathbf{L}$
The constant vector represents the reprojection errors of the tie points corresponding to the ground point on its corresponding image, which is only related to the coordinates of the ground points corresponding to the image points and the corresponding image parameters. The reprojection errors of different image points are independent of each other (Figure 3).

To realize the parallel calculation of reprojection error, each thread is responsible for calculating one reprojection. The number of threads is the same as that of reprojections, and each thread completes one reprojection error calculation independently. Then the parallel calculation of reprojection errors is converted into
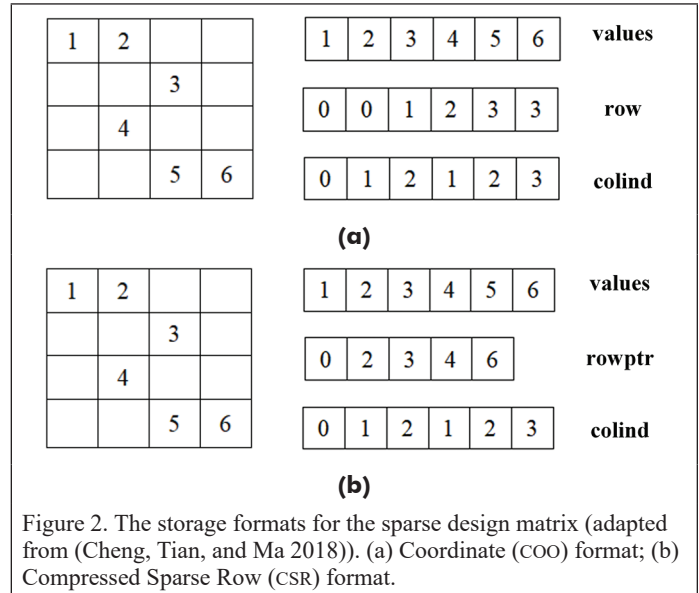
Figure 2. The storage formats for the sparse design matrix (adapted from (Cheng, Tian, and Ma 2018)). (a) Coordinate (COO) format; (b) Compressed Sparse Row (CSR) format.
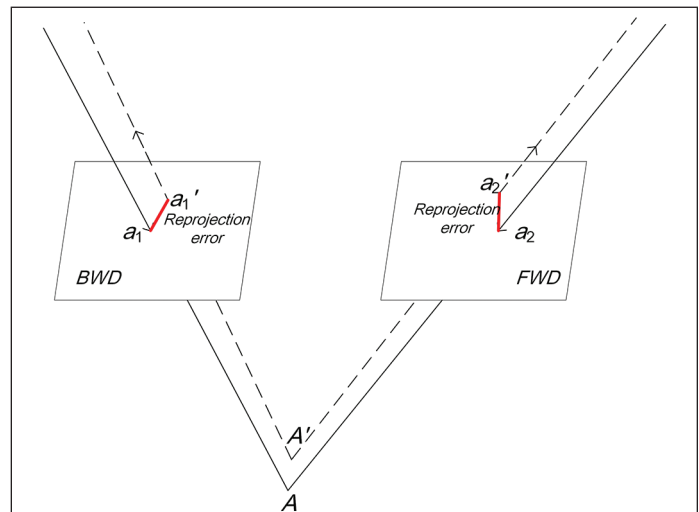
Figure 3. Reprojection errors. BWD represents the backward image, FWD represents the forward image. A represents the ground point coordinate, a1 and a2 represent the image point coordinates on the BWD and FWD images respectively, a_1' and a_2' represent the reprojection coordinates of the image points on the BWD and FWD images, respectively. Reprojection errors are only related to the ground points corresponding to the image points and each image parameters, and image points are independent of each other.

multi-threads to obtain the corresponding reprojection at the same time. The RPC parameters are obtained by the image index, the object coordinates of tie points are located by the image point index, and the image coordinates of tie points are located by the thread index in the projection procedure. Each thread obtains the corresponding parameters from the texture memory, and then according to the reprojection formula, the reprojection errors can be calculated in parallel.

(2) *Parallel computing optimization of the Jacobian matrix* **J** *and preconditioner matrix* **M**

The calculation of the Jacobian matrix **J** can be divided into the solution of image parameters and three-dimensional (3D) point coordinate parameters, i.e., $\mathbf{J} = [\mathbf{J}_c, \mathbf{J}_p]$, to solve the partial derivative $\mathbf{J}_c$ of image parameters and the partial derivative $\mathbf{J}_p$ of 3D point coordinates.

For each image point, the partial derivative matrix $\mathbf{J}_c$ of its corresponding image parameters can be represented by 12 values, and the partial derivative matrix $\mathbf{J}_p$ of corresponding 3D points can be represented by six values. Taking nine scenes of ZY-3 01 satellite images for an example, the number of corresponding ground points is 90 and the number of the image points is 351. The structure of the Jacobian matrix **J** is shown in Figure 4.

Similar to solving the reprojection errors, the parallel solution of the Jacobian matrix J is to establish the relationship between each thread and image parameter and 3D point coordinate. Firstly, the projection values are obtained in the global memory, and then the image parameters are located by the image index in the projection. Then, the 3D point coordinates are obtained from the global memory by the 3D point index in the projection. Finally, the Jacobian matrix J is obtained through the partial derivative formula.

The solution of the preconditioner matrix **M** can be transformed into solving the $\mathbf{J}_c^{\mathrm{T}}\mathbf{J}_c$ and $\mathbf{J}_p^{\mathrm{T}}\mathbf{J}_p$ matrix. The multiplication of the $\mathbf{J}_c^{\mathrm{T}}$ and $\mathbf{J}_c$ matrix is the dot product of the Jc column vector. For example, the value of the first row and second column of the $\mathbf{J}_c^{\mathrm{T}}\mathbf{J}_c$ matrix is the dot product of the first and second columns of the $\mathbf{J}_c$ matrix. Therefore, the product of matrix and matrix is decomposed into the dot product of vector and vector. The dot product between different column vectors is independent and is especially suitable for parallel calculations. The product of each dimension has no effect on the product of other dimensions, which can be calculated by compute unified device architecture's (CUDA's) parallel reduction function. The structure of the $\mathbf{J}_c^{\mathrm{T}}\mathbf{J}_c$ and $\mathbf{J}_p^{\mathrm{T}}\mathbf{J}_p$ matrix is shown in Figure 5.

Besides, the parallel calculation of the $\mathbf{J}_c^{\mathrm{T}}\mathbf{J}_c$ matrix can be carried out directly without storing the $\mathbf{J}_c^{\mathrm{T}}$ matrix. Considering that there are 36 groups of column vector multiplication, every six threads are used to calculate one dimension of the column vector product; that is, every six threads are used to process a row of the $\mathbf{J}_c^{\mathrm{T}}$ matrix and obtain 36 values. Because the 36 values obtained by every six threads, which are one-dimensional of a column vector, thus the CUDA parallel reduction function is used to add up the 36 values obtained by all the six threads in a group to get the result of the whole column vector dot product, that is, the result of the $\mathbf{J}_c^{\mathrm{T}}\mathbf{J}_c$ matrix. Besides, making full use of the symmetry of the $\mathbf{J}_c^{\mathrm{T}}\mathbf{J}_c$ matrix can further reduce about half of the computation and reduce the access to shared memory on the GPU device. Similarly, the parallel calculation of the $\mathbf{J}_c^{\mathrm{T}}\mathbf{J}_c$ matrix can also be calculated according to this method, except that the thread block size is different, that is, nine values obtained by every three threads.

(3) *Parallel computing optimization of the product of the Jacobian matrix* **J** *and constant vector* **L**

The multiplication of the $\mathbf{J}_c^{\mathrm{T}}\mathbf{L}$ matrix can be decomposed into the dot product of column vector and reprojection error vector. The dot product between different column vector and reprojection error vector is independent and can be computed in parallel, and the process of vector dot product can be operated by the CUDA parallel reduction function.

The parallel computation of the $\mathbf{J}_c^{\mathrm{T}}\mathbf{L}$ matrix is carried out directly without storing the $\mathbf{J}_c^{\mathrm{T}}$ matrix. Taking the parallel solution of the $\mathbf{J}_c^{\mathrm{T}}\mathbf{L}$ matrix for an example, a two-dimensional thread block *dimBlock*$(n + 1, 2)$ is defined. Define the thread grid as

dimGrid(cam_num). Each thread block is responsible for one image, and each thread is used to calculate the product of three values in the $\mathbf{J}_c^{\mathrm{T}}$ matrix and the corresponding reprojection error.

Each thread block contains $2 * (n + 1)$ threads. Each thread calculates the product of three values in the JcT matrix and the corresponding reprojection error L. The $2 * (n + 1)$ threads are called
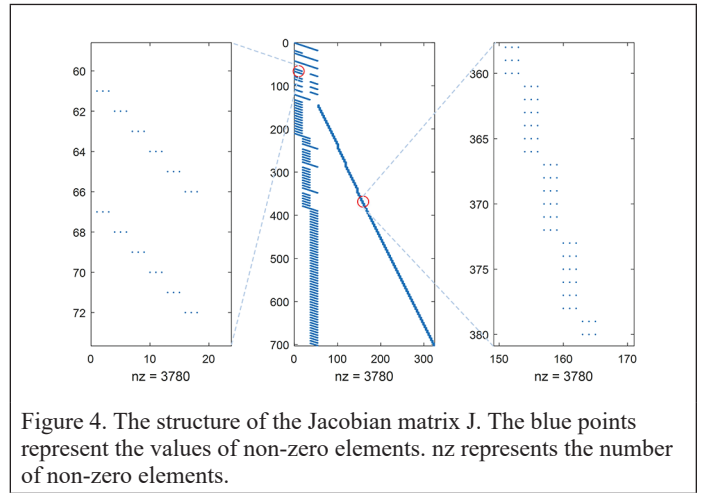
Figure 4. The structure of the Jacobian matrix J. The blue points represent the values of non-zero elements. nz represents the number of non-zero elements.

(a)

(b)
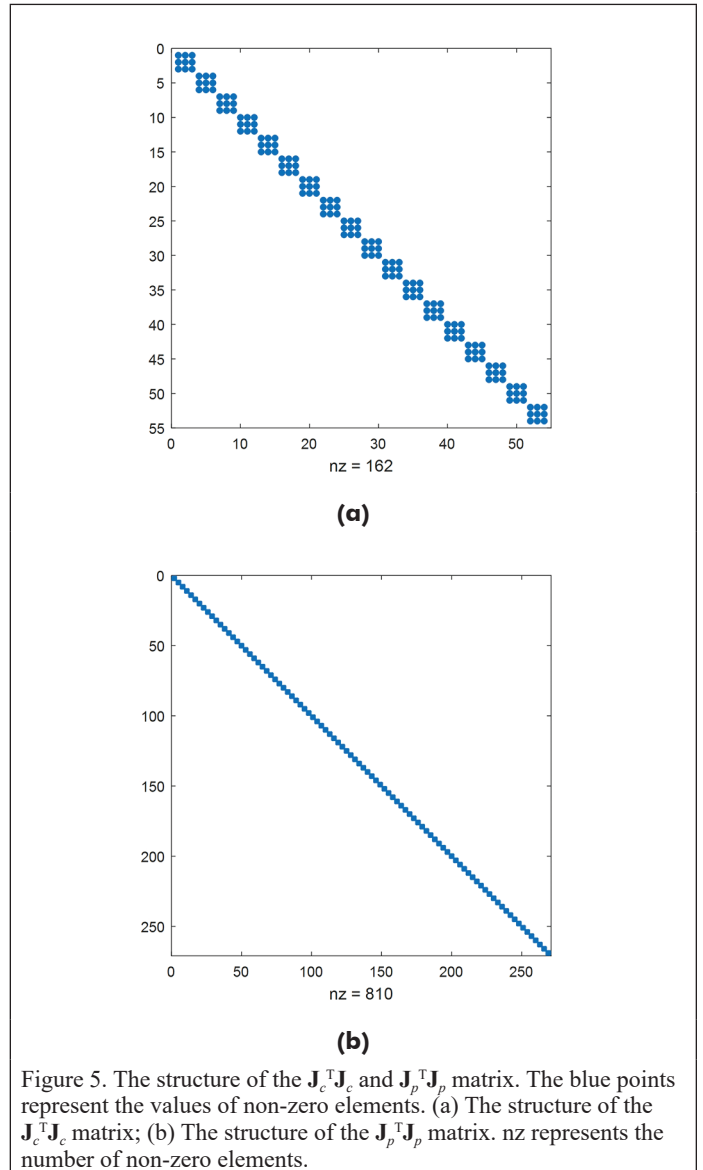
Figure 5. The structure of the $\mathbf{J}_c^{\mathrm{T}}\mathbf{J}_c$ and $\mathbf{J}_p^{\mathrm{T}}\mathbf{J}_p$ matrix. The blue points represent the values of non-zero elements. (a) The structure of the $\mathbf{J}_c^{\mathrm{T}}\mathbf{J}_c$ matrix; (b) The structure of the $\mathbf{J}_p^{\mathrm{T}}\mathbf{J}_p$ matrix. nz represents the number of non-zero elements.

repeatedly until the JcTL matrix is calculated, and each thread is responsible for calculating three results. Then, 6 * (n + 1) results of 2 * (n + 1) threads are stored into shared memory. Finally, the parallel reduction calculation is completed in shared memory to obtain the $\mathbf{J}_c^T\mathbf{L}$ matrix of each image. The calculation results of the whole $\mathbf{J}_c^T\mathbf{L}$ matrix can be obtained by solving several thread blocks at the same time. Besides, thread synchronization statements should be used. The _syncthreads function is used to synchronize threads to ensure that all threads have been stored into the shared memory before performing parallel reduction operations.

GPU Accelerated PCG Parallel Computing Optimization Method

Each step in the PCG method is serial, which involves two times of sparse matrix and vector multiplication, one time of preconditioner matrix and vector multiplication, two times of dot product of two vectors, three times of vector updating, and two times of scalar division. The data-level parallel operation can be used to matrix-vector multiplication, vector-vector multiplication, and vector updating. As a result, the GPU-accelerated PCG method can be used for large-scale BA estimation. The GPU device is used for parallel computation between matrix and vector, and vector and vector, before and during each iteration. The CPU is used to control the iteration cycle, the convergence condition judgment, and the scalar division. NVIDIA's CUDA Sparse Matrix Library cuSPARSE (NVIDIA 2019a) provides operations for sparse matrices, which can be multiplied between vectors by using the *CusparseDcsrmv* function in the cuSPARSE library. The *CublasDdot* function in the cuBLAS (NVIDIA 2019b) library can be used to implement the operation of the dot product of two vectors. The *CublasDaxpy* function in the cuBLAS library is used to update the vector. In this way, the complete PCG method can be realized by using the correlation functions of the cuSPARSE library and the cuBLAS library.

The workflow of the combined PCG and GPU parallel computing method for large-scale BA estimation is shown in Figure 6.

Experiments and Discussion

Study Area and Data Sets

In this study, the BA experiment was carried out using two data sets, namely 132 scenes of Ziyuan-3 (ZY-3) 01 images of Taihu Basin and 829 scenes of ZY-3 01 images of almost the whole Jiangxi Province in China (as shown in Figure 7), which cover areas of about 240 × 310 km and 520 × 650 km, respectively. The software environment used in the experiment was the Windows 10 64-bit operating system, Microsoft Visual Studio 2017 (VC++), and CUDA 10.2. The hardware was a Dell high-performance graphics workstation (the graphics workstation was equipped with a 6-core i7-8700 CPU @ 3.2GHz, 32 GB memory, and an NVIDIA Quadro P2000 professional graphics card with 5 GB global memory).

Two sets of data were used to test the proposed method and the other methods. Details of the data used in this study are provided in
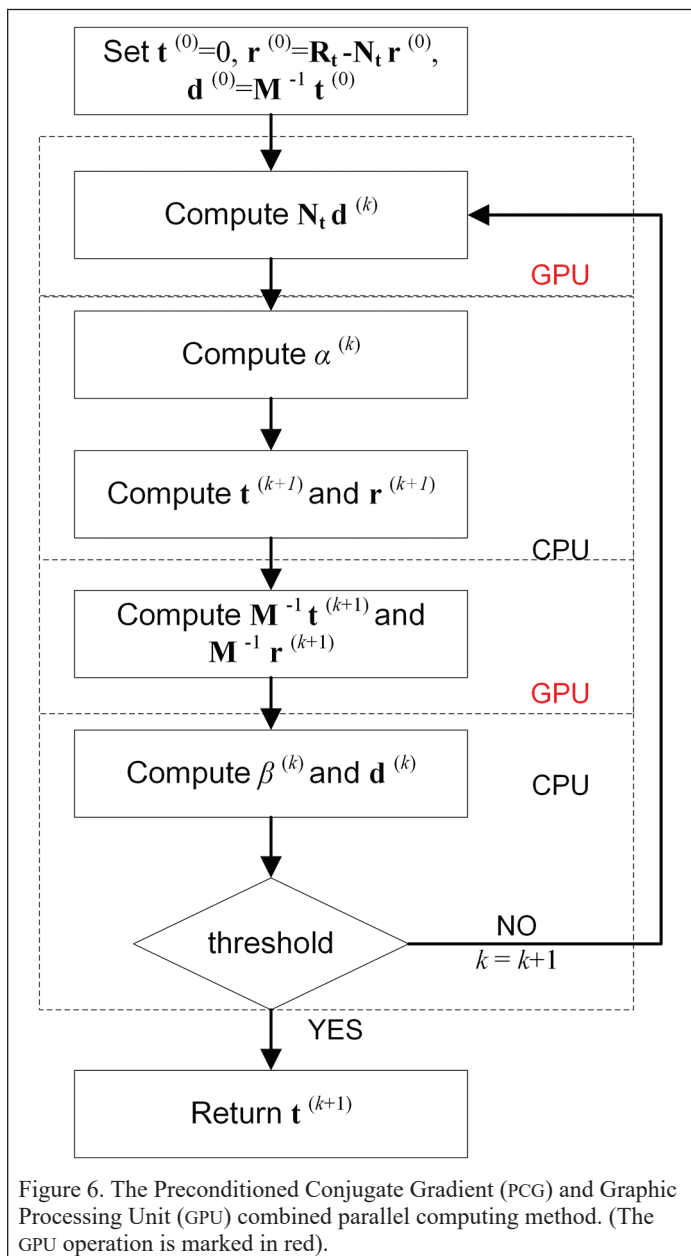
Figure 6. The Preconditioned Conjugate Gradient (PCG) and Graphic Processing Unit (GPU) combined parallel computing method. (The GPU operation is marked in red).
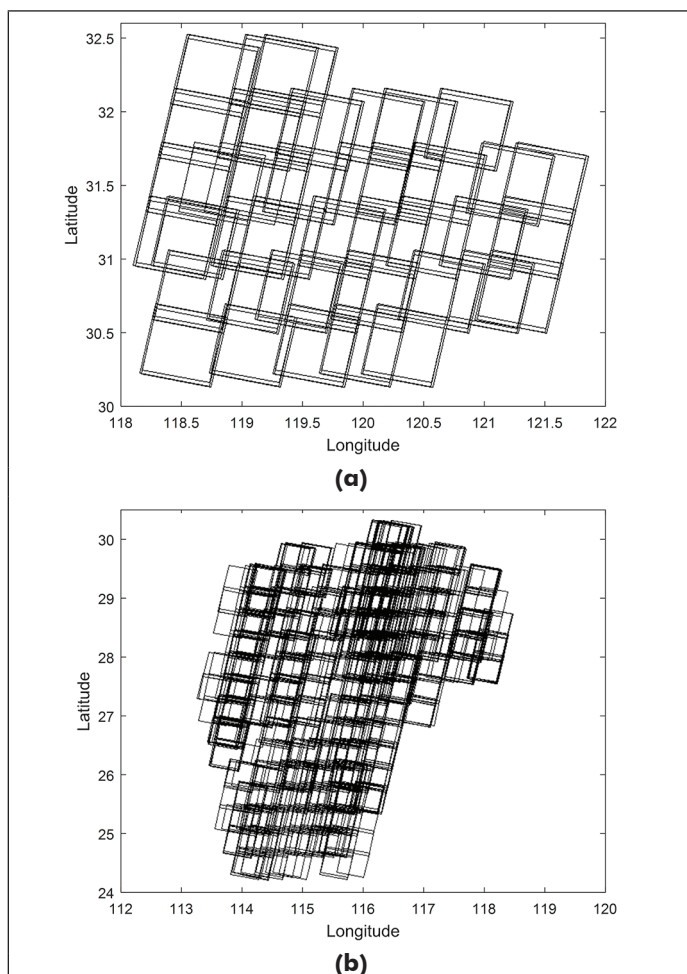
Figure 7. ZY-3 01 satellite image coverage of the two data sets. (a) ZY-3 01 image coverage in the data set A; (b) ZY-3 01 image coverage in the data set B.

Table 1. Data set A contained 132 scenes of ZY-3 01 satellite images, in which the terrain was plain and hilly. Data set B included 829 scenes of ZY-3 01 images, in which the terrain was hilly and mountainous. The ZY-3 01 satellite images of the two areas were captured between 2015 and 2020. Each image was attached with the RPC vendor file. A certain overlap also existed between adjacent images. The survey areas included mountainous, hilly, plain, and other topographic areas, with a maximum and minimum elevation difference of 2500 m.

According to the automatic image-matching methods, such as the scale-invariant feature transform algorithm and k-nearest neighbor matching strategy (the nearest distance threshold is set to 0.8), tie points are acquired from adjacent images, and then the OpenMP parallel matching strategy is adopted to improve the matching efficiency. The number of tie points obtained from the image matching algorithm is very high without a tie point selection strategy and exits some obvious gross errors. In order to solve this issue, we adopted the random sample consensus gross error detection and elimination method, which is effective at reducing the influence of gross errors in the BA results. 63 528 uniform tie points were matched after the use of the above method in the data set A, which cost about one hour, and 158 961 uniform tie points were matched in the data set B, which cost nearly eight hours. The distribution of the tie points of the two data sets is shown in Figure 8.

In order to verify the performance of the proposed method in memory consumption, computational efficiency, and BA accuracy, we compared it with the Single-core CPU and multi-core CPU computing methods. Besides, in order to reduce the statistical error, 10 repeated experiments were carried out and the average value was calculated.

Experimental Results and Discussion

Results of the Memory Consumption Comparison
Between the Proposed Method and the Existing Ones
The conventional dense matrix storage format, the CSR sparse matrix storage format, including the single-core CPU, multi-core CPU computing, Ceres-solver, parallel bundle adjustment (PBA) (Wu *et al.* 2011), and the proposed method were used to process the two groups of experimental data. The memory consumption of the five methods was recorded, respectively. The results of the memory consumption during the BA procedure are listed in Table 2.

From Table 2, it can be seen that the memory consumption of the CSR sparse format is clearly lower than that of the conventional full matrix. When the number of images is 132 (data set A), the full matrix storage format needs at least 80 GB of memory in theory, which will eventually lead to the failure of the BA, because of the inability of a standard computer to allocate such a large amount of memory. After using the CSR format of matrix for the normal equation, only about maximum 345 MB memory space is needed to store all the data needed in the BA.

If the number of images continues to increase, the memory required by the full matrix format will continue to increase. When the number of images increases to 829 (data set B), the full matrix storage format needs at least 1000 GB of memory, in theory. After using the CSR format of matrix for the normal equation, only about maximum 562 MB memory space is needed. However, the memory consumption of the PBA and the proposed methods are higher than that of the single-core CPU, multi-core CPU computing, and Ceres-solver methods, because of the introduction of the GPU device. In addition, the memory consumption of the proposed method is lower than that of PBA method, because of Jacobian transpose matrix $\mathbf{J}_c^T$ is not stored, and the matrix $\mathbf{J}_c^T\mathbf{J}_c$ is a symmetric matrix and only needs to calculate the upper triangular. Meanwhile, a temporary vector stored in the shared memory is calculated in each thread for the multiplication of the matrix $\mathbf{J}_c^T$ and matrix $\mathbf{J}_c$, which not only saves global memory consumption, but also improves matrix multiplication computing efficiency.

Comparison of the Computational Time Costs
Between the Proposed Method and the Existing Ones
The time costs and computational speedup by the five methods for the two data sets are listed in Table 3. As can be seen from Table 3, when
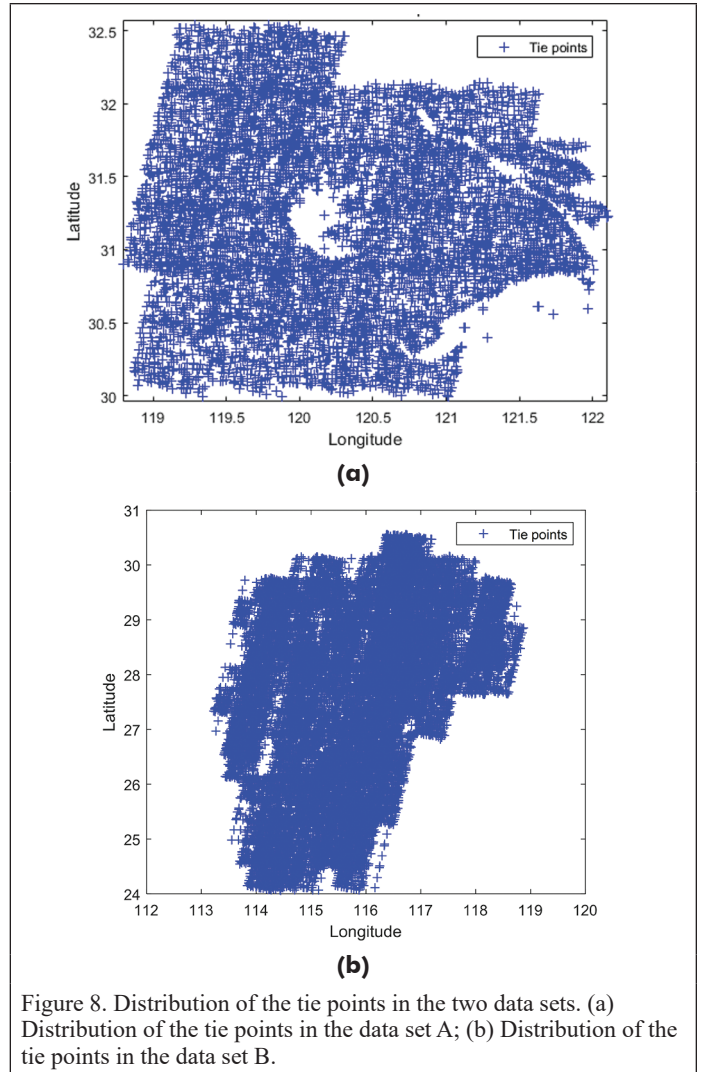
Figure 8. Distribution of the tie points in the two data sets. (a) Distribution of the tie points in the data set A; (b) Distribution of the tie points in the data set B.

Table 1. Details of the test data sets.

Data Set	Source	Topography	Capture Time	Number of Images	Number of Tie Points
A	ZY-3 01	plain and hilly	2015–2016	132	63 528
B	ZY-3 01	hilly and mountainous	2017–2020	829	158 961

Table 2. Memory consumption of the different methods.

Data Set	CSR Sparse Matrix (Units: MB)				
	Single-core CPU	Multi-core CPU	Ceres-solver	PBA	The Proposed Method
A	184	195	189	356	345
B	340	352	346	583	562

CSR = Compressed Sparse Row; MB = megabytes; CPU = central processing unit; PBA = parallel bundle adjustment.

Table 3. Computational time costs of the different methods (units: seconds).

Data Set	Single-Core CPU	Multi-Core CPU	Ceres-Solver	PBA	The Proposed Method
A	3.21	1.78	2.06	0.56	0.63
B	41.90	13.47	30.15	4.01	4.42

CPU = central processing unit; PBA = parallel bundle adjustment.

the number of images is 132, the conventional full matrix storage method fails in BA because of the limitation of the memory consumption. And the efficiency of the multi-core CPU computing and Ceres-solver methods are higher than that of the single-core CPU computing method, whereas the calculation efficiency of the PBA method is the highest and the proposed method is comparable with PBA method. The computational time costs of the mentioned above five methods are 3.31 s, 1.78 s, 2.06 s, 0.56 s, and 0.63 s in the data set A, and in the data set B, the computational time costs of the five methods are 41.90 s, 13.47 s, 30.15 s, 4.01 s, and 4.41 s, respectively.

As can be seen from Table 4, when the number of images is small (data set A), the computational speedup of the multi-core CPU computing method is a little faster than that of the single-core CPU computing method, namely 1.86 times, while when the number of images is large (data set B), the computational speedup of the multi-core CPU computing method is 3.11 times faster than that of the single-core CPU computing method. But the computational speedup of the proposed method is obviously faster than that of the single-core CPU computing method, namely 5.25 and 9.48 times faster in the two data sets, respectively. In addition, the computational speedup of the PBA method is obvious faster than that of the single-core CPU computing method, namely 5.73 and 10.45 times faster in the two data sets, respectively.

Table 4. Computational speedup of the different methods.

Data Set	Single-Core CPU	Multi-Core CPU	Ceres-Solver	PBA	The Proposed Method
A	1	1.80	1.56	5.73	5.10
B	1	3.11	1.39	10.45	9.48

CPU = central processing unit; PBA = parallel bundle adjustment.

Comparison of BA Accuracies Between the Proposed Method and the Existing Ones

The PBA method and proposed method were found to be superior to the single-core CPU, multi-core CPU computing, and Ceres-solver methods in the computational efficiency. In order to further verify the performance of the proposed method in BA accuracy, we compared the BA accuracy of the above methods. The two groups of data were processed by the methods mentioned above, and the BA accuracy was compared and analyzed.

The BA accuracy was measured by the relative accuracy, i.e., the reprojection residuals of the tie points. Analysis of the reprojection residuals of the tie points can evaluate the accuracy and stability of the BA, which can also reflect the relative geo-positioning accuracy of the images to a certain extent. The BA accuracies of the data set A are shown in Table 5, and the residual errors in the x- and y-directions after the BA by the methods are shown in Figure 9.

The relative geo-positioning accuracy in the data set A is shown in Figure 9, before and after the application of the proposed BA method. The residual errors of the tie points are shown in Table 5, before and after the BA. As can be seen from Table 5, the BA accuracy of the proposed method is comparable to that of the single-core CPU, multi-core CPU computing, and Ceres-solver methods. The maximum reprojection image point residual of the forward intersection used RPC vendor file is 7.973 pixels, the root-mean-square error (RMSE) is 1.725 pixels in the x- (flight) direction, the maximum residual is 10.204 pixels, and the RMSE is 2.466 pixels in the y- (scan) direction. After BA with the proposed method, the maximum residual is 3.787 pixels, the RMSE is 0.561 pixels in the x- (flight) direction, the maximum residual is

7.167 pixels, and the RMSE is 0.752 pixels in the y- (scan) direction. Meanwhile, the BA accuracy of the proposed method is superior to that of the PBA method. The reason is that the threshold value is larger and fewer iterations in the PBA method, which causes the PBA method more efficient than the proposed method.

Conclusions

In this paper, in view of the challenges encountered in the large-scale BA of HRSI without GCPs, we have presented a combined PCG and GPU parallel computing method to estimate the BA results, which can reduce the memory consumption and computational time cost while ensuring the BA accuracy. The PCG method is used to estimate the normal equation, the CSR sparse matrix storage format is adopted to reduce the memory consumption, and a GPU parallel computing method is used to improve the computational efficiency of the proposed approach. Two sets of real data, made up of 132 scenes of ZY-3 01 satellite remote sensing images in Taihu Basin and 829 scenes of ZY-3 01 images almost in the whole of Jiangxi Province of China, were used for the
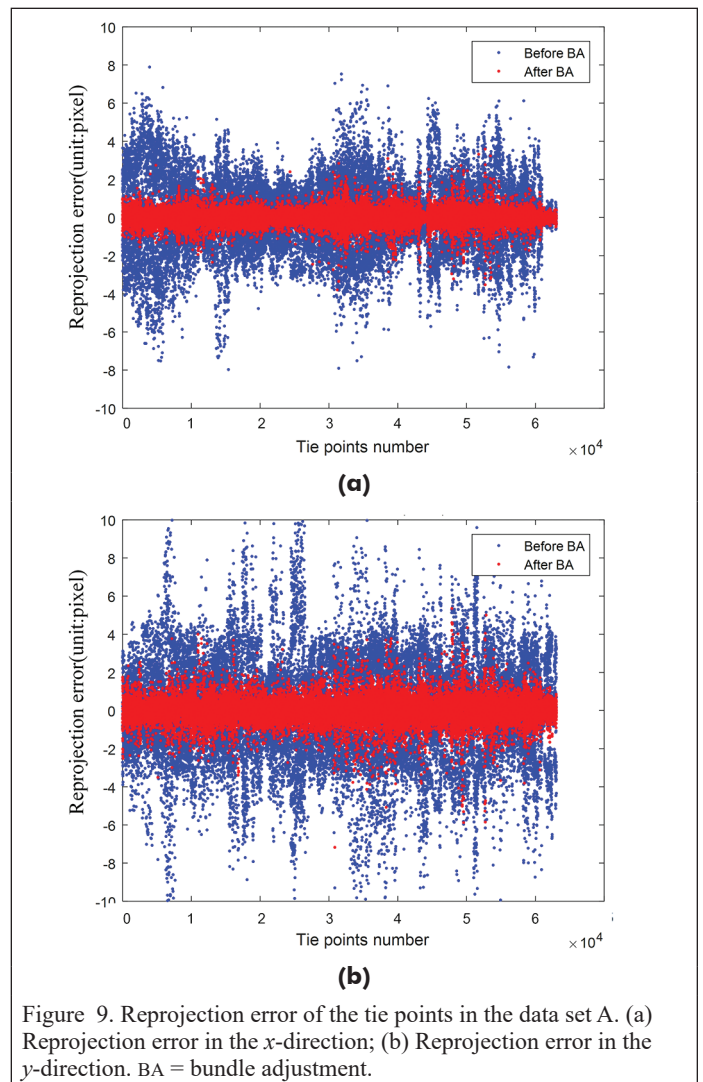
Figure 9. Reprojection error of the tie points in the data set A. (a) Reprojection error in the *x*-direction; (b) Reprojection error in the *y*-direction. BA = bundle adjustment.

Table 5. The root-mean-square error (RMSE) of the different methods (units: pixels)

Data Set	Single-Core CPU			Multi-Core CPU			Ceres-Solver			PBA			The Proposed Method		
	x	*y*	*xy*	*x*	*y*	*xy*	*x*	*y*	*xy*	*x*	*y*	*xy*	*x*	*y*	*xy*
A	0.375	0.630	0.733	0.375	0.630	0.733	0.375	0.630	0.733	0.381	0.674	0.774	0.376	0.631	0.734
B	0.561	0.750	0.936	0.561	0.750	0.936	0.561	0.750	0.936	0.659	0.791	1.03	0.561	0.752	0.938

comparative experiments. Through the comparative analysis of the experimental results, the following conclusions could be drawn:

(1) Compared with the conventional full matrix storage format, the CSR format was found to be able to reduce the memory consumption, and when the number of satellite images reached 829 (data set B), the tie point number reached 158 961, and the memory consumption of the proposed method was 562 MB, while the full matrix storage method failed in the memory application.

(2) The computational speed of the proposed method was found to be much faster than that of the single-core CPU computing method. When the number of images was increased to 132 (data set A), the computational speed of the proposed method was 6.21 times faster than that of the single-core CPU computing method. When the number of images was increased to 829 (data set B), the time costs of the proposed method, the single-core CPU and multi-core CPU computing methods being 4.42 s, 13.47 s, and 41.90 s, and the computational speedup of the proposed method and multi-core CPU computing methods was 9.48 and 3.11 times faster than that of the single-core CPU computing method, respectively, while the full matrix storage method failed in the BA estimation because of the high memory consumption. While the computational efficiency of the proposed method is comparable with that of the PBA method.

(3) The proposed method was able to obtain almost the same BA accuracy as the other methods. When the number of images was 829 in the data set B, the reprojection residuals of the tie points of the proposed method, the single-core CPU, multi-core CPU computing, Ceres-solver, and PBA methods were 0.938, 0.936, 0.936, 0.936, and 1.03 pixels, respectively. Moreover, the BA accuracy of the proposed method is superior to that of the PBA method.

Acknowledgments

References

Agarwal, S., N. Snavely, S. Seitz and R. Szeliski. 2010. Bundle adjustment in the large. Pages 29–42 in *Proceedings European Conference on Computer Vision*, held in Heraklion, Crete, 5–11 September 2010.

Agullo, E., C. Augonnet, J. Dongarra, M. Faverge, H. Ltaief, S. Thibault and S. Tomov. 2011. QR factorization on a multicore node enhanced with multiple GPU accelerators. Pages 932–943 in *Proceedings IEEE International Symposium on Parallel and Distributed Processing*, held in Anchorage, Ala., 16–20 May 2011.

Bru, R. and M. Tůma. 2008. Balanced incomplete factorization. *Siam Journal on Scientific Computing* 30:2302–2318. https://doi.org/10.1137/070696088.

Byröd, M. and K. Åström. 2009. Bundle adjustment using conjugate gradients with multiscale preconditioning. Pages 1–10 in *Proceedings British Machine Vision Conference*, held in London, UK, 7–10 September 2009.

Byröd, M. and K. Åström. 2010. Conjugate gradient bundle adjustment. Pages 114–127 in *European Conference on Computer Vision*, held in Heraklion, Crete, 5–11 September 2010.

Cao, N., P. Zhou, X. Wang and G. Li. 2019. Laser altimetry data-aided satellite geometry model refined processing. *Journal of Remote Sensing* 23:291–302. https://doi.org/10.11834/jrs.20197252.

Chen, X., B. Zhang, T. Zhang, H. Guo and M. Cen. 2016. Public DEM-assisted positioning method for Chinese satellite imagery without ground control points. *Acta Geodaetica et Cartographica Sinica* 45:1361–1370.

Cheng, K., J. Tian and R. Ma. 2018. Study on efficient storage format of sparse matrix based on GPU. *Computer Engineering* 44:54–60.

Choudhary, S., S. Gupta and P. Narayanan. 2010. Practical time bundle adjustment for 3d reconstruction on the GPU. Pages 423–435 in *Proceedings European Conference on Computer Vision*, held in Heraklion, Crete, 5–11 September 2010.

D'Angelo, P. and P. Reinartz. 2012. DSM based orientation of large stereo satellite image blocks. Pages 209–214 in *Proceedings XXII ISPRS Congress 2012, ISPRS—International Archives of the Photogrammetry, Remote Sensing and Spatial Information Sciences*, held in Melbourne, Australia, 25 August–1 September 2012.

Fraser, C. S. and H. B. Hanley. 2005. Bias-compensated RPCs for sensor orientation of high-resolution satellite imagery. *Photogrammetric Engineering and Remote Sensing* 71(8):909–915.

Fraser, C. S. and M. Ravanbakhsh. 2009. Geo-reference performance of GEOEYE-1: Early indications of metric performance. Pages 1–6 in *Proceedings ISPRS High-Resolution Earth Imaging for Geospatial Information Workshop*, held in Hannover, Germany, 2–5 June 2009.

Gong, J., M. Wang and B. Yang. 2017. High-precision geometric processing theory and method of high-resolution optical remote sensing satellite imagery without GCP. *Acta Geodaetica et Cartographica Sinica* 46:1255–1261.

Grodecki, J. and G. Dial. 2003. Block adjustment of high-resolution satellite images described by rational polynomials. *Photogrammetric Engineering and Remote Sensing* 69(1):59–68.

Hänsch, R., I. Drude and O. Hellwich. 2016. Modern methods of bundle adjustment on the GPU. Pages 43–50 in *Proceedings ISPRS Annals of Photogrammetry, Remote Sensing and Spatial Information Sciences*, held in Prague, Czech Republic, 12–19 July 2016.

Jiang, Y., G. Zhang, X. Tang, D. Li, T. Wang, W. Huang and L. Li. 2015. Improvement and assessment of the geometric accuracy of Chinese high-resolution optical satellites. *IEEE Journal of Selected Topics in Applied Earth Observations and Remote Sensing* 8(10):4841–4852.

Jiao, N., F. Wang, H. You, M. Yang and X. Yao. 2018. Geometric positioning accuracy improvement of ZY-3 satellite imagery based on statistical learning theory. *Sensors* 18(6):1701.

Liu, S., X. Tong, F. Wang, W. Sun, C. Guo, Z. Ye, Y. Jin, H. Xie and P. Chen. 2016. Attitude jitter detection based on remotely sensed images and dense ground controls: A case study for Chinese ZY-3 satellite. *IEEE Journal of Selected Topics in Applied Earth Observations and Remote Sensing* 9(12):5760–5766.

Liu, X., W. Gao and Z. Hu. 2012. Hybrid parallel bundle adjustment for 3D scene reconstruction with massive points. *Journal of Computer Science and Technology* 27(6):1269–1280.

Ma, Z., X. Wu, L. Yan and Z. Xu. 2017. Geometric positioning for satellite imagery without ground control points by exploiting repeated observation. *Sensors* 17(2):240.

Nathan, B. and M. Garland. 2009. Implementing sparse matrix-vector multiplication on throughput-oriented processors. Pages 1–11 in *Proceedings of the Conference on High Performance Computing Networking*, held in Portland, Ore., 14–20 November 2009.

Noguchi, M., C. Fraser, T. Nakamura, T. Shimono and S. Oki. 2004. Accuracy assessment of QuickBird stereo imagery. *Photogrammetric Record* 19(106):128–137.

NVIDIA. CUDA CUBLAS Library. 2019a. <https://developer.download.nvidia.cn/compute/DevZone/docs/html/CUDALibraries/doc/CUBLAS_Library.pdf, 10 December 2019>.

NVIDIA. CUDA CUSPARSE Library. 2019b. <https://developer.download.nvidia.cn/compute/DevZone/docs/html/CUDALibraries/doc/CUSPARSE_Library.pdf, 10 December 2019>.

Pan, X., T. Jiang, A. Yu, X. Wang and Y. Zhang. 2017. Geo-positioning of remote sensing images with reference image. *Journal of Remote Sensing* 23:673–684.

Peng, J., J. Liu and H. Wei. 2021. A scalable parallel preconditioned conjugate gradient method for bundle adjustment. *Applied Intelligence* 1–13.

Poli, D., L., Zhang and A. Gruen. 2004. SPOT-5/HRS stereo images orientation and automated DSM generation. Pages 421–432 in *Proceedings ISPRS Annals of Photogrammetry, Remote Sensing and Spatial Information Sciences*, held in Istanbul, Turkey Republic, 12–23 July 2004.

Song, W., S. Liu, X. Tong, C. Niu, Z. Ye and Y. Jin. 2021. Combined geometric positioning and performance analysis of multi-resolution optical imageries from satellite and aerial platforms based on weighted RFM bundle adjustment. *Remote Sensing* 13:620.

Sun, Y., L. Zhang, B. Xu and Y. Zhang. 2019. Method and GCP-independent block adjustment for ZY-3 satellite images. *Journal of Remote Sensing* 23:205–214.

Tang, X., G. Zhang, X. Zhu, H. Pan, Y. Jiang, P. Zhou and X. Wang. 2013. Triple linear-array image geometry model of ZiYuan-3 surveying satellite and its validation. *International Journal of Image and Data Fusion* 4:33–51.

Tao, C. V. and Y. Hu. 2001. A comprehensive study of the rational function model for photogrammetric processing. *Photogrammetric Engineering and Remote Sensing* 67(12):1347–1357.

Tong, X., Q. Fu, S. Liu, H. Wang, Z. Ye, Y. Jin, P. Chen, X. Xu, C. Wang, S. Liu, Z. Hong and K. Luan. 2020. Optimal selection of virtual control points with planar constraints for large-scale block adjustment of satellite imagery. *Photogrammetric Record* 35(10):487–508.

Tong, X., L. Li, S. Liu, Y. Xu, Z. Ye, Y. Jin, F. Wang and H. Xie. 2015a. Detection and estimation of ZY-3 three-line array image distortions caused by attitude oscillation. *ISPRS Journal of Photogrammetry and Remote Sensing* 101(3):291–309.

Tong, X., S. Liu and Q. Weng. 2010. Bias-corrected rational polynomial coefficients for high accuracy geo-positioning of QuickBird stereo imagery. *ISPRS Journal of Photogrammetry and Remote Sensing* 65(2):218–226.

Tong, X., S. Liu and Q. Weng. 2009. Geometric processing of QuickBird stereo imageries for urban land use mapping: A case study in Shanghai, China. *IEEE Journal of Selected Topics in Applied Earth Observations and Remote Sensing* 2(2):61–66.

Tong, X., Y. Xu, Z. Ye, S. Liu, X. Tang, L. Li, H. Xie and J. Xie. 2015b. Attitude oscillation detection of the ZY-3 satellite by using multispectral parallax images. *IEEE Transactions on Geoscience and Remote Sensing* 53(6):3522–3534.

Toutin, T. and P. Cheng. 2000. Demystification of IKONOS. *Earth Observation Magazine* 9:17–21.

Wang, M., B. Yang, D. Li and Y. Pi. 2017. Technologies and applications of block adjustment without control for ZY-3 images covering China. *Geomatics and Information Science of Wuhan University* 42(4):427–433.

Wathen, A. and D. Silvester. 1993. Fast iterative solution of stabilised Stokes systems. Part I: Using simple diagonal preconditioners. *SIAM Journal on Numerical Analysis* 30(3):630–649.

Wu, C., S. Agarwal, B. Curless and S. Seitz. 2011. Multicore bundle adjustment. Pages 3057–3064 in *Proceedings of the IEEE Conference on Computer Vision and Pattern Recognition*, held in Colorado Springs, Colo., 20–25 June 2011.

Yang, B., M. Wang, W. Xu, D. Li and Y. Pi. 2017. Large-scale block adjustment without use of ground control points based on the compensation of geometric calibration for ZY-3 images. *ISPRS Journal of Photogrammetry and Remote Sensing* 134:1–14.

Yao, X. and H. You. 2018. Multi-observed block adjustment for satellite images without ground control points. *Remote Sensing Technology and Application* 33:555–562.

Zhang, G., B. Jiang, T. Wang, Y. Ye and X. Li. 2021. Combined block adjustment for optical satellite stereo imagery assisted by spaceborne SAR and laser altimetry data. *Remote Sensing* 13:3062.

Zhang, Y., Y. Wan, X. Huang and X. Ling. 2016. DEM-assisted RFM block adjustment of pushbroom nadir viewing HRS imagery. *IEEE Transactions on Geoscience and Remote Sensing* 54(2):1025–1034.

Zhang, Y., M. Zheng, X. Xiong and J. Xiong. 2014. Multistrip bundle block adjustment of ZY-3 satellite imagery by rigorous sensor model without ground control point. *IEEE Geoscience and Remote Sensing Letters* 12(4):865–869.

Zheng, M., Y. Zhang, S. Zhou, J. Zhu and X. Xiong. 2016. Bundle block adjustment of large-scale remote sensing data with block-based sparse matrix compression combined with preconditioned conjugate gradient. *Computers and Geosciences* 92(7):70–78.

Zheng, M., S. Zhou, X. Xiong and J. Zhu. 2017. A new GPU bundle adjustment method for large-scale data. *Photogrammetric Engineering and Remote Sensing* 83:633–641.

Zhou, P., X. Tang, Z. Wang, N. Cao and X. Wang. 2018. SRTM-assisted block adjustment for stereo pushbroom imagery. *Photogrammetric Record* 33(161):49–65.

IN-PRESS ARTICLES

Oussama Mezouar, Fatiha Meskine, Issam Boukerch. Automatic Satellite Images Ortho-rectification using K-means based Cascaded Meta-heuristic Algorithm.

Yuanyang Lin, Jing He, Gang Liu, Biao Mou, Bing Wang, and Rao Fu. UAS-based multi-temporal rice plant height change prediction.

Bo Xu, Daiwei Zhang, Han Hu, Qing Zhu, Qiang Wang, Xuming Ge, Min Chen, Yan Zhou. Spherical Hough Transform for Robust Line Detection toward a 2D-3D Integrated Mobile Mapping System.

Xinyan Pang, Na Ren, Changqing Zhu, Shuitao Guo, Ying Xiong. Blind and Robust Watermarking Algorithm for Remote Sensing Images Resistant to Geometric Attacks.

Zhikang Lin, Wei Liu, Yulong Wang, Yan Xu, Chaoyang Niu. Change Detection in SAR Images through Clustering Fusion Algorithm and Deep Neural Networks.

Hongbin Luo, Wanqiu Zhang, Cairong Yue, and Si Chen. Strategies for Forest Height Estimation by High-Precision DEM Combined with Short-Wavelength PolInSAR TanDEM-X.

Yunping Chen, Yue Yang, Lei Hou, Kangzhuo Yang, Jiaxiang Yu, and Yuan Sun. High-Resolution Aerosol Optical Depth Retrieval in Urban Areas Based on Sentinel-2.

Xiaoguang Ruan, Fanghao Yang, Meijing Guo, and Chao Zou. 3D Scene Modeling Method and Feasibility Analysis of River Water-Land Integration.

Identification of Drought Events in Major Basins of Africa from GRACE Total Water Storage and Modeled Products

Ayman M. Elameen, Shuanggen Jin, and Daniel Olago

Abstract

Terrestrial water storage (TWS) plays a vital role in climatological and hydrological processes. Most of the developed drought indices from the Gravity Recovery and Climate Experiment (GRACE) over Africa neglected the influencing roles of individual water storage components in calculating the drought index and thus may either underestimate or overestimate drought characteristics. In this paper, we proposed a Weighted Water Storage Deficit Index for drought assessment over the major river basins in Africa (i.e., Nile, Congo, Niger, Zambezi, and Orange) with accounting for the contribution of each TWS component on the drought signal. We coupled the GRACE data and WaterGAP Global Hydrology Model through utilizing the component contribution ratio as the weight. The results showed that water storage components demonstrated distinctly different contributions to TWS variability and thus drought signal response in onset and duration. The most severe droughts over the Nile, Congo, Niger, Zambezi, and Orange occurred in 2006, 2012, 2006, 2006, and 2003, respectively. The most prolonged drought of 84 months was observed over the Niger basin. This study suggests that considering the weight of individual components in the drought index provides more reasonable and realistic drought estimates over large basins in Africa from GRACE.

Introduction

Droughts have increased in frequency and severity due to climate change throughout the world's river basins in recent decades (Forootan *et al.* 2019). According to the sixth assessment report of the International Panel for Climate Change (IPCC), global temperatures have risen by ~1°C since industrialization, which may further amplify by 1.5°C between 2030 and 2050 as a result of human activities (IPCC 2018). As the population grows and water demand increases, droughts are triggered and aggravated by anthropogenic activities such as deforestation and the construction of dams (Schlosser *et al.* 2014; AghaKouchak 2015; Omer *et al.* 2020; Sarfo *et al.* 2022). To prioritize adaptation actions in global hot spots, it is essential to characterize droughts.

Although the continent has abundant water resources with meeting its ecological and agricultural needs, climatic extremes are becoming increasingly perilous, endangering the valuable water supply and millions of lives on the continent (Masih *et al.* 2014; IPCC 2022). Two of the biggest drought tragedies ever documented in history occurred in the Sahel region in 2007 and the Nile basin in 1984. These droughts caused the death of approximately 750 000 people (Vicente-Serrano *et al.* 2012). Future projections indicate that the probability of drought occurrence will increase across the entire African continent, leading to significant regional implications (Ahmadalipour and Moradkhani 2018; IPCC 2022). Additionally, excessive water demand may lead to the overuse of freshwater resources, which might result in disputes among water users during dry spells. This may increase the risk of hydro-political tension in Africa, as the Transboundary Rivers represent 64% of the entire region's landmass (United Nations Environment Program 2010). Monitoring the drought situation in Africa is crucial for prioritizing adaptations to avert water scarcity and disputes.

Long and uninterrupted in situ hydro-climatic observations are required for drought monitoring. Yet Africa's land-based observation network has been deteriorating with time, having only one-eighth of the minimum density required by the World Meteorological Organization and with only 22% of stations fully meeting the Global Climate Observing System requirements (Dobardzic *et al.* 2019). Due to the insufficiency of in situ data records in Africa, monitoring hydrological drought in the continent's basins has been limited (Ferreira *et al.* 2018). Additionally, a substantial financial and political commitment is required to record and share in situ observations, both of which are frequently missing. Remote sensing observations represent an alternative source to counter data deficiencies in many data-poor regions worldwide. Moreover, satellite-borne sensors have featured as an effective tool for tracking droughts, considering their capacity to offer regional-to-global coverage (Jiao *et al.* 2021).

Several remote sensing–based products have been used globally to assess and detect drought situations. Among these are Moderate Resolution Imaging Spectroradiometer (MODIS)–based evapotranspiration, soil moisture from Sentinel-1 and the Soil Moisture Active Passive radiometer, and the Normalized Difference Vegetation Index from Landsat (West *et al.* 2019; Modanesi *et al.* 2020). Although these measurements could deliver valuable information about agricultural and meteorological droughts, the task of assessing hydrological drought remains daunting (Papa *et al.* 2022) since they can capture only surface and shallow subsurface conditions. Also, it is problematic to evaluate droughts based only on surface measurements (e.g., precipitation and soil moisture), as the reduction of water from the deepest aquifers may continue even after the surface storage has dried up (Leblanc *et al.* 2009). After launching the Gravity Recovery and Climate Experiment (GRACE) satellite mission in 2002, the potential time-variable gravity measurement offered an integrated perspective for drought monitoring since it can capture vertically integrated terrestrial water storage (TWS)

Ayman M. Elameen is with the School of Remote Sensing and Geomatics Engineering, Nanjing University of Information Science and Technology, Nanjing 210044, China.

Shuanggen Jin is with the School of Remote Sensing and Geomatics Engineering, Nanjing University of Information Science and Technology, Nanjing 210044, China; the School of Surveying and Land Information Engineering, Henan Polytechnic University, Jiaozuo 454000, China; and Shanghai Astronomical Observatory, Chinese Academy of Science, Shanghai 200030, China (sgjin@nuist.edu.cn; sg.jin@yahoo.com).

Daniel Olago is with the Department of Earth and Climate Sciences, University of Nairobi, Nairobi 00100, Kenya..

changes (i.e., from the top surface water to the deepest groundwater) (Ndehedehe *et al.* 2018).

The unique potential of GRACE measurements offered hydrologists a new dimension to develop new GRACE-based drought indices (Hassan and Jin 2014; Jin and Zhang 2016). Therefore, numerous studies have applied GRACE-based indicators for drought analysis and monitoring. For example, Kumar *et al.* (2021) evaluated the drought severity over the Godavari basin using the GRACE Combined Climatologic Deviation Index. Liu *et al.* (2020) proposed a GRACE-based Drought Severity Index and assessed the drought variations for China's large basins. Khorrami and Gunduz (2021) proposed an Enhanced Water Storage Deficit Index to observe drought conditions in Turkey. Wu *et al.* (2021) characterized the drought over southwest China using the GRACE-derived Total Storage Deficit Index. Cui *et al.* (2021) developed a multiscale Standardized Terrestrial Index of water storage to assess the global hydrological droughts.

A number of studies have been performed to track droughts in Africa using different drought indices. Examples of earlier investigations and the indices used by different authors are listed in Table 1. The majority of used indices either originated from a single TWS component, such as surface water (precipitation) or were created primarily to take into account the total TWS components, including surface, soil, ground, snow, and canopy water. The influence role of the individual TWS components in drought index is not taken into account in these previous studies. Each water storage component is an essential hydrological variable to comprehend drought occurrences, according to Lopez *et al.* (2020). Since the TWS-based drought indicator considers all components together, the primary problem is abstract. As a result, it is more reasonable to analyze these components separately since one of them (e.g., groundwater) could alleviate the drought impact. Therefore, this study aims to consider the role of individual TWS components and their relative contributions to drought index computing, which might lead to a more reasonable and realistic drought evaluations.

Answering the topic of how different water storage elements respond to drought conditions throughout Africa's major river basins is the main goal of this study. To do this, we used the Weighted Water Storage Deficit Index (WWSDI) (Wang *et al.* 2020), which was developed from the GRACE WSDI but also considered the influence of the individual TWS components to provide further reliable droughts assessment. We used the WWSDI to identify the critical drought characteristics (i.e., severity, intensity, and duration) over five Africa's major river basins (Nile, Congo, Niger, Zambezi, and Orange) (see Figure 1) during the 2003–2016 period. We further compared the analysis of WWSDI against the GRACE-based Water Storage Deficit Index (WSDI) and the commonly used indicators—the self-calibrated Palmer Drought Severity Index (scPDSI), the Standardized Precipitation Index, and the Standardized Precipitation Evapotranspiration Index—to assess its efficiency. The understudied river basins in this article represent the major sources of temporal fluctuations of hydrological masses across the continent. They lie between 32.6°S to 31.4°N and 11.5°W to 39.8°E and cover a broad range of different sizes, and climate zones vary from humid to semiarid. More details regarding these basins are provided in Table 2. Further details on the data sets, the methods used, and results are highlighted in subsequent sections.

Materials and Methods

Data Sets
In this section, we provide a brief introduction of the data used in this study. Table 3 provides a tentative summary.

Precipitation
The study of droughts requires a thorough grasp of precipitation. This study uses monthly precipitation of 0.25° × 0.25° from 2003 to 2016, acquired from the seventh version of the Tropical Rainfall Measurement Mission (TRMM 3B43) (Huffman *et al.*, 2007). Numerous studies (Ferreira *et al.* 2018; Abd-Elbaky and Jin 2019) have been conducted over Africa using this data set. Moreover, Awange *et al.* (2016) reported that TRMM was suitable for hydrometeorological applications over most parts of Africa.

Table 1. Different drought indices employed in previous studies.

River Basin	Drought Indices/Data Inputs	References
Nile	GRACE TWSD	Hasan *et al.* (2021)
	SPI, SPEI, SSI	Nigatu *et al.* (2021)
	MSDI	
	PDSI	
	GRACE WSDI	
	GRACE CCDI	
	GRACE GGDI	
Congo	SPI, SRI	Ndehedehe *et al.* (2019)
	SPI, GRACE TWS change, MERRA TWS change	Ndehedehe *et al.* (2017)
	SPEI, GRACE-TWS change	Ndehedehe *et al.* (2020)
Niger	De-seasoned GRACE TWS change	Ferreira *et al.* (2018)
	SPI, SPEI, SRI	Oguntunde *et al.* (2018)
	SPI, GRACE TWS change, MERRA TWS change	Ndehedehe *et al.* (2017)
Zambezi	GRACE WSD	Thomas *et al.* (2014)
	SPI, TSDI	Hulsman *et al.* (2021)
	WLDI	
Orange	SPI, SPEI	Abiodun *et al.* (2019)

CCDI = Combined Climatologic Deviation Index; GGDI = GRACE Groundwater Drought Index; GRACE = Gravity Recovery and Climate Experiment; MSDI = Precipitation and Soil Moisture Integrated Index; PDSI = Palmer Drought Severity Index; SPEI = Standardized Precipitation Evapotranspiration Index; SPI = Standardized Precipitation Index; SRI = Standardized Runoff Index; SSI = Soil Moisture Index; TSDI = Total Storage Deficit Index; TWSD = total water storage deficit; WLDI = Water-Level Deficit Index; WSD = water storage deficit; WSDI = Water Storage Deficit Index.

Table 2. Area, length, climate, and mean annual precipitation of river basins selected in this study.

River Basin	Area (10^5 km^2)	Length (km)	Climate	Mean Annual P (mm)	Elevation (m)
Nile	31.8	6700	Semiarid	678	726
Congo	37.5	4667	Humid	705	737
Niger	21.8	4200	Semiarid	1504	419
Zambezi	13.8	2650	Semiarid	975	1003
Orange	9.7	2300	Semiarid	359	270

Potential Evapotranspiration
The present study utilizes monthly potential evapotranspiration (PET) retrieved from the MOD16A2 sensor, publicly available worldwide at 8-day temporal resolutions and 500-m spatial resolution (Running *et al.* 2017). We select MODIS16A2 data sets due to their relatively lower magnitude of uncertainty and rather good performance over the region (Andam-Akorful *et al.* 2015; Mekonnen *et al.* 2022). MODIS16A2 PET data extraction was conducted using Google Earth Engine (GEE). The 8-day PET data were averagely weighted to obtain the monthly PET values for this study.

GRACE-Derived TWS Anomalies
GRACE measurements (Jin *et al.* 2011; Ndehedehe *et al.* 2020) provide useful information for hydrological studies since they offer a quantitative assessment of monthly variations of water in lakes, rivers, reservoirs, snow, soil, and aquifers. The present study employs the sixth release of the spherical harmonics coefficient solutions processed by the Center for Space Research (CSR) at the University of Texas at Austin (Zhang *et al.* 2018), to derive gridded terrestrial water storage anomaly (TWSA) data over the selected river basins from 2003 to 2016 at a spatial resolution of 1°.

The coefficients were processed by being truncated at degree and order 60. They were then filtered and destriped using a 400-km-radius Gaussian filter. The leakage reduction and averaging approach (Khaki *et al.* 2018) were used in this study to minimize the leakage error contributions over the understudied river basins. The missing months in the
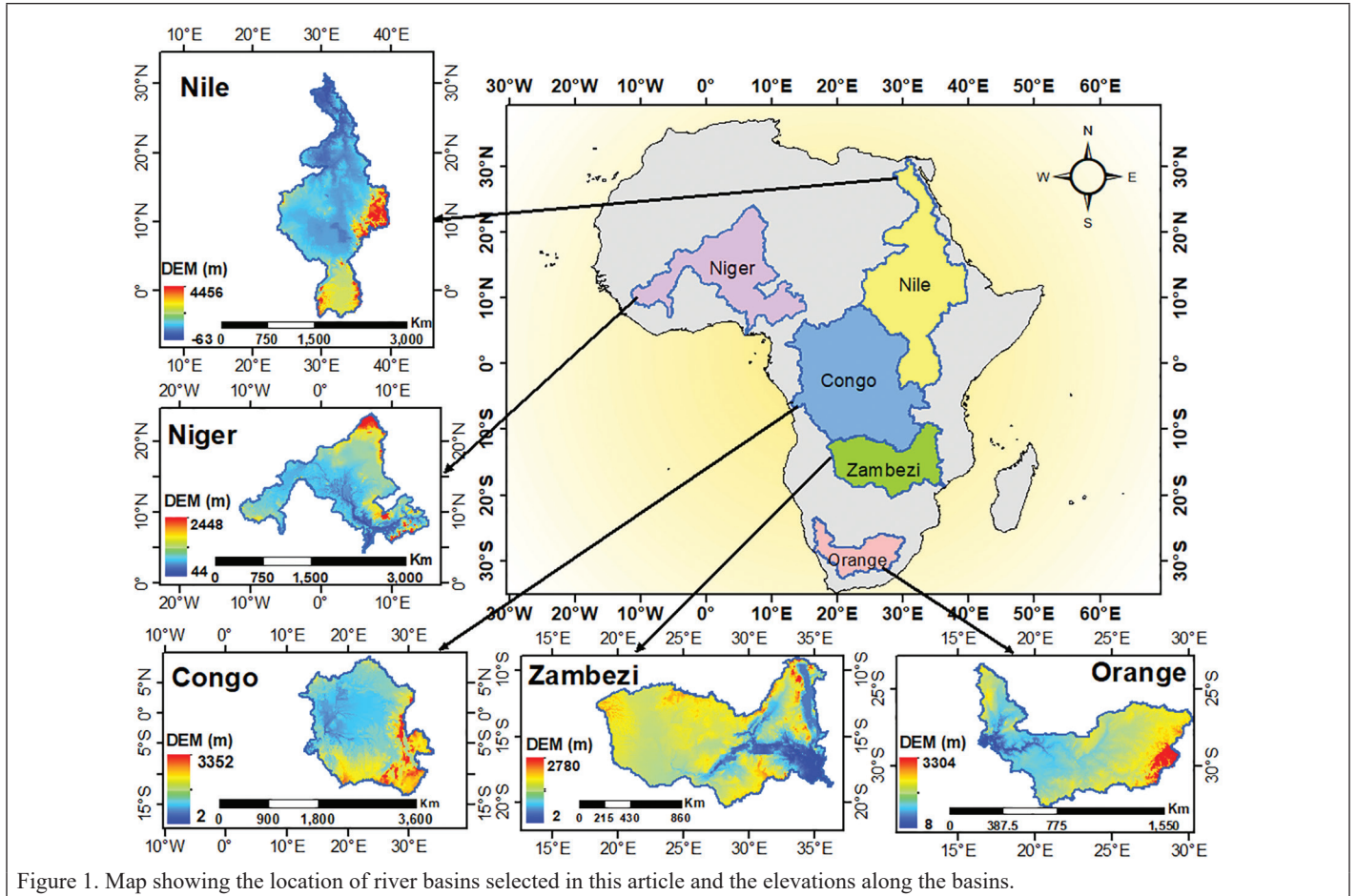
Figure 1. Map showing the location of river basins selected in this article and the elevations along the basins.

Table 3. Data sets used in this study.

Categories	Data/Model	Time Span	Spatial Resolution	Data Sources
GRACETWS	CSR-SH (RL06)	2003–2016	1°×1°	http://www2.csr.utexas.edu/grace/
Precipitation	TRMM	2003–2016	0.25°×0.25°	https://disc.gsfc.nasa.gov/datasets/TRMM_3B43_7
Surface water	WGHM	2003–2016	0.5°×0.5°	https://doi.pangaea.de/10.1594/PANGAEA.918447
Soil moisture	WGHM	2003–2016	0.5°×0.5°	https://doi.pangaea.de/10.1594/PANGAEA.918447
Snow water equivalent	WGHM	2003–2016	0.5°×0.5°	https://doi.pangaea.de/10.1594/PANGAEA.918447
Canopy water	WGHM	2003–2016	0.5°×0.5°	https://doi.pangaea.de/10.1594/PANGAEA.918447
Potential evaporation	MOD16A2	2003–2016	500 m	https://developers.google.com/earth-engine/datasets/catalog/MODIS_006_MOD16A2
scPDSI	CRU	2003–2016	0.5°×0.5°	https://crudata.uea.ac.uk/cru/data/drought/

CRU = Climate Research Unit; CSR = Center for Space Research; GRACE TWS = Gravity Recovery and Climate Experiment terrestrial water storage; scPDSI = self-calibrated Palmer Drought Severity Index; TRMM = Tropical Rainfall Measurement Mission; WGHM = WaterGAP Global Hydrology Model.

time series were filled using linear interpolation via averaging the prior and subsequent months (Yang *et al.* 2017).

scPDSI Gridded Data Sets
This study utilizes monthly scPDSI (Wells *et al.* 2004) time-series (v4.04) data sets for the period 2003–2016, with a spatial resolution of 0.5°. The data sets were collected from the Climate Research Unit (CRU) at the University of East Anglia, United Kingdom.

WaterGAP Global Hydrology Model
This study uses the WaterGAP Global Hydrology Model (WGHM) to separate the components of GRACE TWS data (i.e., surface water storage [SWS], soil moisture storage [SMS], groundwater storage [GWS], snow water equivalent [SWE], and plant canopy water storage [CWS]). Given that the SWS and GWS are taken into account, the WaterGAP model has an advantage over the Global Land Data Assimilation System (GLDAS) (Huang *et al.* 2019). Moreover, climate fluctuations and anthropogenic influences on water availability are also considered (Wang *et al.* 2020). The recent model version (WaterGAP 2.2d) at a resolution of 0.5° is used

in this study (Müller Schmied *et al.* 2021). The data are available from January 2000 to December 2016.

Methodology

Processing Standardized Drought Indices
Standardized indices are widely used to quantify droughts worldwide. We employ SPI, SPEI, and scPDSI to assess the effectiveness of WWSDI in characterizing drought events over the chosen basins for this study. SPI is a meteorological drought index that is based only on precipitation (Satish Kumar *et al.* 2021). To compute SPI, the monthly TRMM precipitation is normalized by utilizing an equal probability function. SPEI is an expansion of SPI, as it includes the influence of evapotranspiration on drought under changing environments. SPEI is computed by subtracting precipitation from potential evapotranspiration using climatic water balance. Hence, TRMM precipitation and MOD16 PET products were employed to calculate SPEI. It required long-term observations to reliably calculate SPI and SPEI; however, many studies, such as Sun *et al.* (2018), have successfully used the available GRACE term

to characterize drought phenomena. Both indicators can be obtained at different timescales (1, 3, 6, 9, 12, and 24 months). However, each timescale reflects a distinct condition. For example, 1 month could indicate meteorological types of droughts, 3 months could reflect the soil moisture conditions, 6 months may indicate anomalies in land water storage, and 9 months could depict the agricultural droughts well. Hence, to provide a solid validation for WWSDI performance, the 6-month timescale was employed since it can effectively demonstrate the TWS deficit that was monitored by WWSDI (Sun *et al.* 2018; Wang *et al.* 2020). Another widely used meteorological drought index is the scP-DSI, which is developed based on the Palmer Drought Severity Index (PDSI) using a physical water balance model. The scPDSI timescale is fixed unlike the two indices previously described.

Processing Components Estimation
As mentioned previously, TWSA is composed of the following:

$$TWSA = GWSA + SMSA + SWEA + SWSA + CWSA \quad (1)$$

In this study, TWSA is estimated from Grace, whereas soil moisture storage anomalies (SMSA), snow water equivalent anomalies (SWEA), surface water storage anomalies (SWSA), and canopy water storage anomalies (CWSA) are the anomalies of SMS, SWE, SWS, and CWS, deduced from the WGHM. Groundwater storage anomalies (GWSA) are estimated via subtracting TWSA from the WGHM-derived components in Equation 1. Note that the SWEA and CWSA have minimal contribution to TWSA over African basins. Thus, they are assumed to be negligible and not considered in groundwater storage anomalies computation, as indicated in Equation 1 (further description provided in "Results and Analysis"). SMSA and SWSA are expanded into the spherical harmonic coefficients, truncated to 60°, ordered, and filtered by Gaussian filter.

Component Contribution Ratio
We utilized the component contribution ratio (CCR) to determine the mean percentage contribution of a single water storage component to the temporal variability of the total TWS (Huang *et al.* 2019). CCR is calculated as the ratio of the mean absolute deviation (MAD) of a storage component to the total TWS variability (TV), as expressed by (Zhang *et al.* 2019)

$$CCR_S = \frac{MAD_S}{TV} \quad (2)$$

where $MAD_s = \frac{1}{N} \sum_{t}^{N} |S_t - \bar{S}|$, S denotes the single storage components, and TV is the total variability, calculated as summation of all components MAD_s ($\sum_{S}^{Storages} MAD_S$).

Processing the WWSDI
In this study, in order to depict drought in the five large Africa's basins, we adopted the WWSDI developed by Wang *et al.* (2020). WWSD is based on WSD, which represents the difference between TWSA time series and the monthly means of TWSA values (Thomas *et al.* 2014) and is computed as

$$WSD_{u,v} = TWSA_{u,v} - \overline{TWSA}_v \quad (3)$$

where $TWSA_{u,v}$ is the value of TWSA time series for the vth month of the uth year and $\overline{TWSA}_v$ is the mean value of the vth month of TWSA during the study period. A negative deviation represents storage deficits. Furthermore, three continuous negative months or longer is considered a drought event (Thomas *et al.* 2014). In order to make comparisons against SPI, SPEI, and scPDSI in this study, the WSD is normalized to WSDI by the zero-mean normalization method, based on the expression

$$WSDI = \frac{WSD - \mu}{\sigma} \quad (4)$$

where σ and μ indicate standard deviations and the mean of the WSD time series, respectively. In order to construct WWSD, we incorporated

different TWS components (i.e., GWS, SWS, and SMS) to the drought index by weighting these components through their CCR using Equation 2. We subsequently calculated the water deficit for each component (i.e., groundwater storage deficit [GWSD], surface water storage deficit [SWSD], and soil moisture storage deficit [SMSD]) like the WSD. Thereafter, WWSD was generated by combining these water components' deficits after multiplying them by their respective weights,

$$WWSD = \omega_1 GWSD + \omega_2 SWSD + \omega_3 SMSD \quad (5)$$

where ω_i (= 1, 2, 3) represent the derived weight from Equation 2. Finally, WWSDI is achieved by normalizing WWSD, as shown in Equation 4.

Results and Analysis

Distribution of Precipitation, Terrestrial Water Storage, and Its Components
The monthly averaged TWSA variation and its individual components other than precipitation over 14 years (from January 2003 to December 2016) are illustrated in Figure 2. A clear seasonal cycle as well as interannual variation in the amount of TWSA, GWSA, SMSA, SWSA, and precipitation are visible for all the basins. CWSA and SWEA variations were observed to be minimal over all the basins. Thus, the latter two components are not considered in the following analysis.
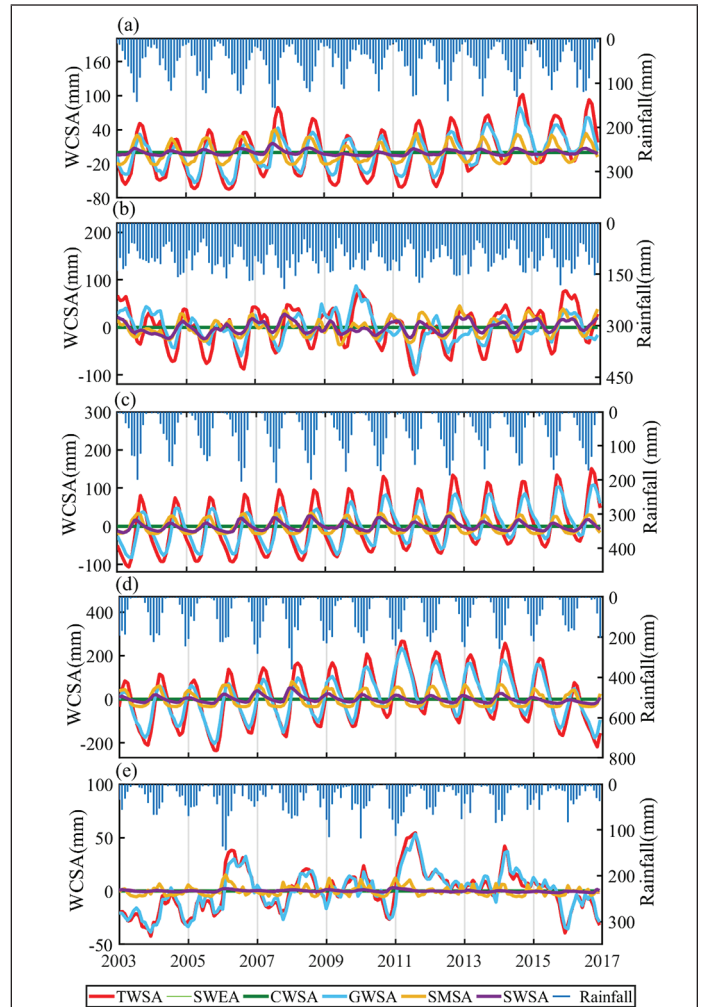
Figure 2. Time series of monthly precipitation, the terrestrial water storage anomaly (TWSA), and the terrestrial water components storage anomaly (WCSA) in the (a) Nile, (b) Congo, (c) Niger, (d) Zambezi, and (e) Orange river basins.

A comparison of precipitation and the TWSA seasonal cycle is shown in Table 4. It can be observed that both the Nile and the Niger basins followed broadly similar seasonal cycle variation since they have similar climatological/hydrological characteristics. Also, the Zambezi and Orange basins revealed similar pattern of the rainiest and driest months in terms of precipitation and TWSA.

It is clear from Figure 2 that a time lag exists between the peak of precipitation and TWSA as well as between the individual components of TWSA. Herein, the lag between TWSA, GWSA, SMSA, SWSA, and precipitation is further quantified via calculating the Pearson correlation coefficients among these storage components as well as the respective perception for different time lags (i.e., 0–12 months). Subsequently, the value of the maximum correlation coefficient between each two variables and the lags (numbers in brackets) corresponding to those maximum values are identified and shown in Figure 3.

The results from Figure 3 suggest a time lag of 0 to 2 months between TWS anomalies derived from GRACE and precipitation over

Table 4. Wet and dry seasons of precipitation and terrestrial water storage anomalies (TWSA) over large African river basins.

River Basin	Wet Months		Dry Months	
	Precipitation (mm)	TWSA (mm)	Precipitation (mm)	TWSA (mm)
Nile	Jun–Aug (101.5)	Sep–Nov (48.3)	Dec–Feb (14.5)	Mar–May (−41.9)
Congo	Sep–Nov (154.4)	Dec–Feb (32.8)	Jun–Aug (7.9)	Sep–Nov (−47.2)
Niger	Jun–Aug (136)	Sep–Nov (75.7)	Dec–Feb (2.6)	Mar–May (−64.8)
Zambezi	Dec–Feb (204.6)	Mar–May (49.7)	Jun–Aug (2.8)	Sep–Nov (−188.6)
Orange	Dec–Feb (60.7)	Mar–May (6.45)	Jun–Aug (7.09)	Sep–Nov (−9.33)

the five basins. In general, the change in TWS was clearly noticeable in the season following the precipitation change over all basins (see Table 4). This result is consistent with the findings of Abd-Elbaky and Jin (2019) and Zhang *et al.* (2019). Concerning the lags between individual

Figure 3. Maximum Pearson correlation coefficients between monthly terrestrial water storage anomalies (TWSA), the individual components of TWSA, and precipitation in the (a) Nile, (b) Congo, (c) Niger, (d) Zambezi, and (e) Orange river basins. The numbers in brackets represent the corresponding lag months.
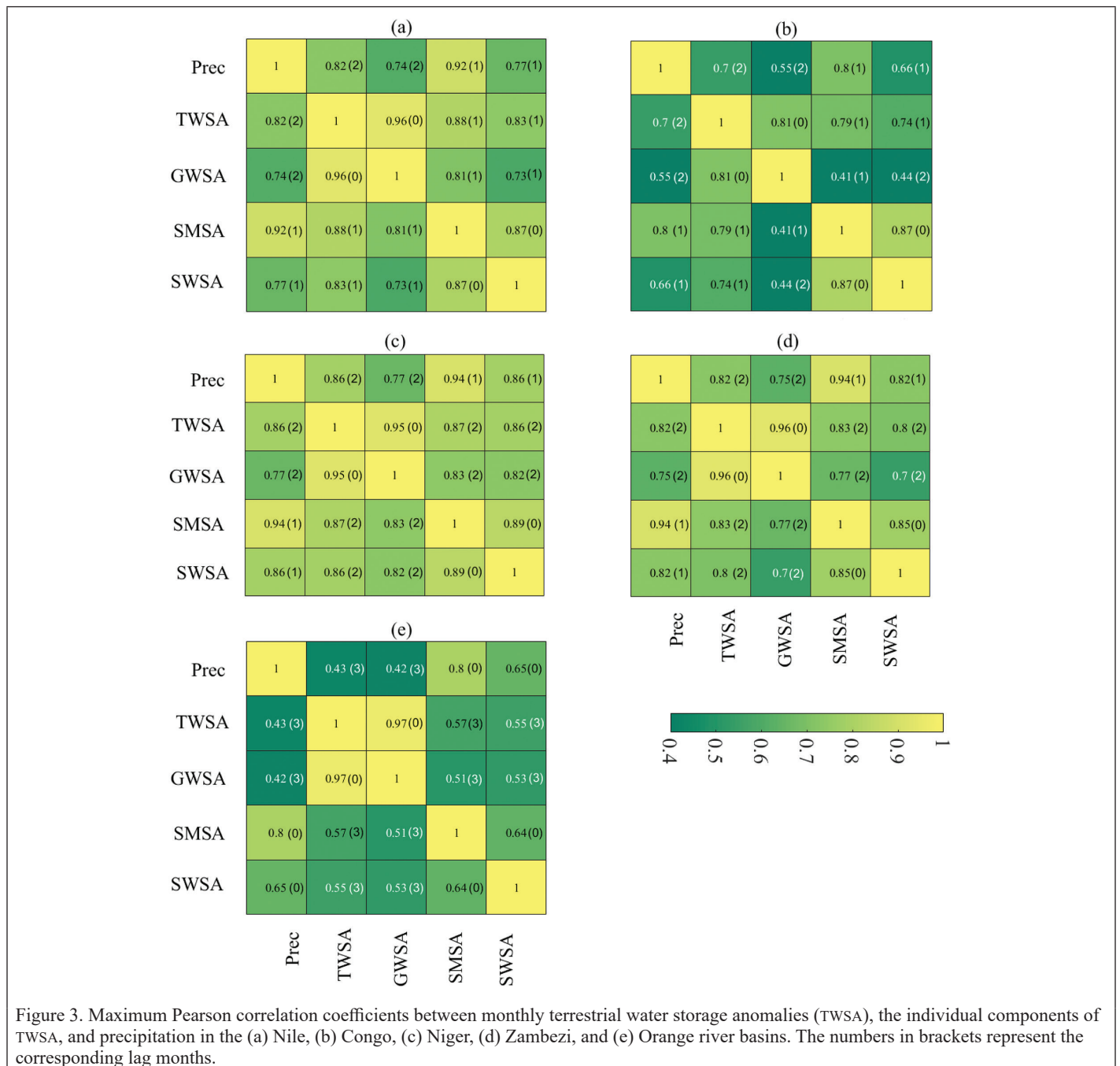
components of the TWSA and precipitation, the largest correlation coefficients were observed corresponding to 2 to 3 months of lag in terms of GWSA and 0 to 1 month in terms of SWSA and SMSA, respectively. The lags between GWSA, SMSA, and SWSA against precipitation can be arranged as GWSA > SMSA ≥ SWSA. These findings further supported the assertion of precipitation as a key driver of water storage, with immense control over the hydrological cycle in these basins.

In each basin, the lags between TWSA, individual components of TWSA, and precipitation are attributed mainly to each basin's peculiar geographical and climatological characteristics.

Figure 4 illustrates the calculated component contribution ratio (CCR) of GWSA, SMSA, and SWSA for the five major rivers in Africa. The results revealed that the highest contribution to total water storage variability over the five river basins was induced mainly by the GWS anomaly accounting (56%, 61%, 47%, 64%, and 78%), followed by SMSA (34%, 32%, 25%, 26%, and 18%) and SWSA (10%, 21%, 14%, 10%, and 4%) for the Nile, Congo, Niger, Zambezi, and Orange basins, respectively. Furthermore, SMSA and SWSA peaks and troughs are not necessarily coincident with the peaks and troughs of TWSA, as shown in Figures 2 and 3. This difference is attributed mainly to the different time lags between precipitation falling and the response of the single TWS components against the precipitation. These findings denote that different TWS components exhibit different amplitude, phase, and contributions to TWS change. This further confirms that different components contribute distinctly to TWS changes over the understudied basins. Given their unique contributions to the shift in TWS, it is natural to wonder whether these water components react differently to the incidence of drought over those basins. Further answers and analysis are provided in the following section.

Deficit of Terrestrial Water Components in the Major Basins of Africa

Figures 5 and 6 demonstrate the time series of the derived terrestrial water components storage deficit (WCSD) (including GWSD, SMSD, and SWSD) and terrestrial water storage deficit indices (WCSDI) (including GWSDI, SMSDI, and SWSDI) from January 2003 to December 2016 for the five major African basins. According to Figure 5, the overall correlation between GWSD and WSD for the five basins ranged from 0.91 to 0.99. SMSD and SWSD followed different patterns from that of GWSD during different periods in the time series. For example, over the Congo basin (Figure 5b), from January 2009 to January 2013, GWSD recorded a declining trend of −1.03 mm, whereas SMSD and SWSD exhibited rising trends of 0.3 mm and 0.15 mm, respectively.

To better understand the drought dynamics over the considered basins in this study, WCSD was also utilized as an indicator to identify drought events based on 3 months or more of continuous negative deficits (from January 2003 to December 2016), as shown in Figure 7. The results clearly show that different WCSD indicators detected varied onset, duration, and drought occurrences during the study period. For example, over the Nile basin (Figure 7a), groundwater storage deficit (GWSD) exhibited six drought events, whereas SMSD and SWSD exhibited 12 and 7 events, respectively, between January 2003 and December 2016. Moreover, a noticeable prolonged drought state in terms of groundwater storage (GWSD) was observed from January 2003 to February 2007, January 2003 to December 2009, January 2003 to July 2008, and January 2003 to January 2006 over the Nile, Niger, Zambezi, and Orange basins, respectively, separated by nearly one wetting month. The drought trends depicted from (Figure 7a, 7c, 7d, and 7e) are consistent with GWSDI (Figure 6a, 6c, 6d, and 6e). The late response of GWS to recharge from SWS and/or the increased groundwater withdrawal can support this finding. Furthermore, the Niger basin had the most prolonged GWS drought state among all the basins recording 7 years. Previous work by Ferreira *et al.* (2018) on a water storage (TWS) drought signal over West Africa (including the Niger basin) found a long drier period between 2003 and 2008. These findings are consistent with the results presented in this study. According to the analysis of the 2003–2008 period presented in this article, the water storage (TWS) based drought trend is related to groundwater storage, where most of the TWS (i.e., 61%) in the Niger basin is induced mainly by GWS (Figures 4 and 7c). Ferreira *et al.* (2018) reported that
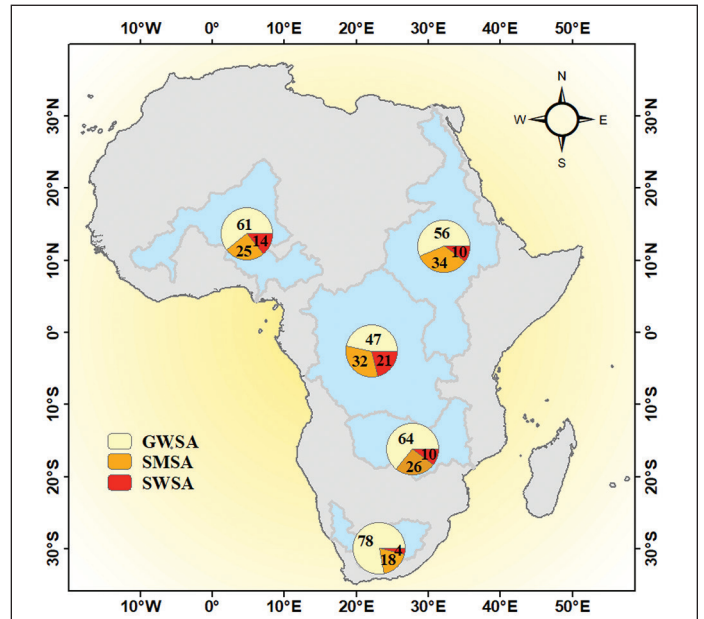
Figure 4. Component contribution ratios of groundwater storage anomalies (GWSA), soil moisture storage anomalies (SMSA), and surface water storage anomalies (SWSA) to the total water storage anomalies (TWSA) in the major river basins of Africa.
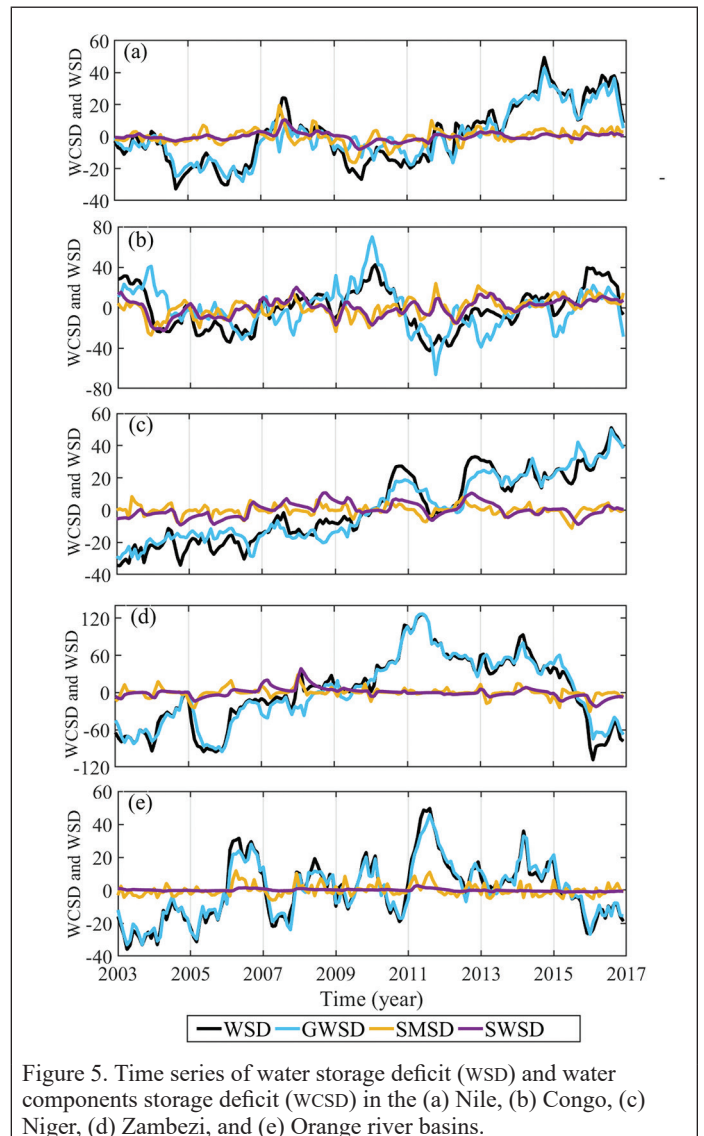
Figure 5. Time series of water storage deficit (WSD) and water components storage deficit (WCSD) in the (a) Nile, (b) Congo, (c) Niger, (d) Zambezi, and (e) Orange river basins.

the rainfall increasing trend between 2003 and 2008 over West Africa is associated with a drought period. They attributed this to the unsustainable influencing of rainfall recovery to the water-storage increase across West Africa, in the early 2000s. Consequently, the occurrence of the long GWS drought state in the Niger basin may be attributed to the minimal or late influences of surface water on the groundwater storage in the early 2000s.

The results also demonstrate that SWSD and SWSDI over the Orange basin (Figures 6e and 7e) exhibited a long drier period from March 2013 to December 2016 except for February and June 2013. This finding is in line with an early study conducted over the South African drying signal (Munday and Washington 2019). The latter linked the decline in precipitation with local surface temperature change since increased subsidence is linked to clearer skies and higher net solar radiation. Also, the reduction in precipitation magnitude is correlated to the changing patterns of tropical sea surface temperatures. Furthermore, the exceeding demand for surface water may cause the surface water shortage, where the water of the Orange basin is heavily utilized, and most of the riparian states rely on the Orange basin's water resources for commercial crop irrigation; in addition, 29 dams are operated over the river (Mgquba and Majozi 2020), which may cause large water abstractions.

The results acquired from WCSD and WCSDI analysis concluded that different water components responded differently to drought events over the basins in this study. Thus, these parameters can be considered for a more realistic and reliable drought evaluation over the major African basins.
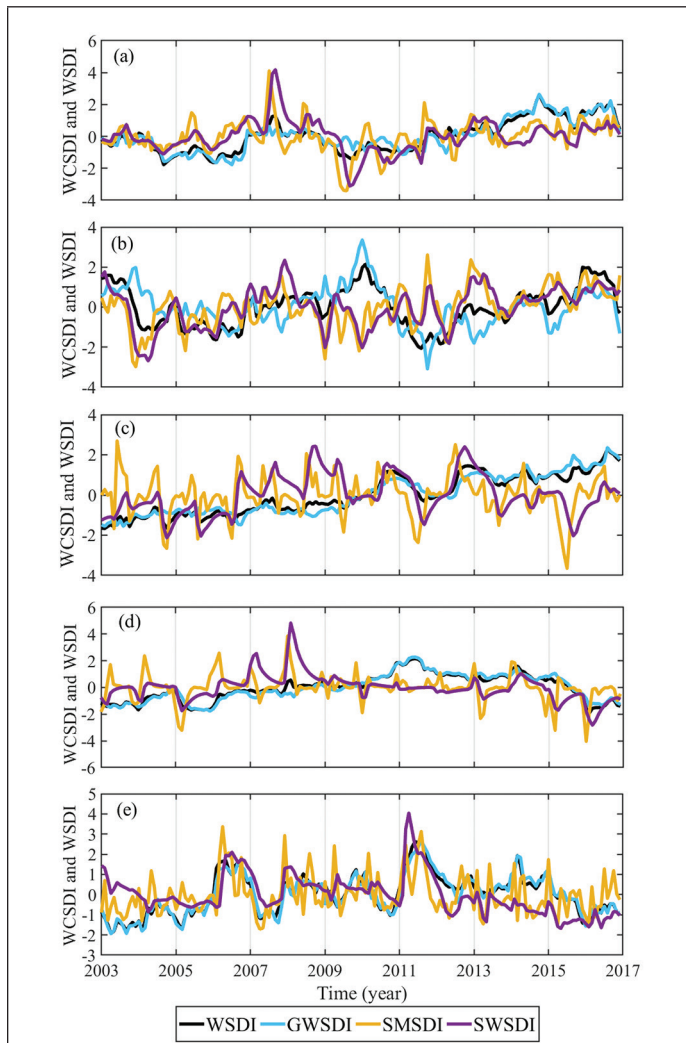
Figure 6. Time series of water storage deficit index (WSDI) and water components storage deficit index (WCSDI) in the (a) Nile, (b) Congo, (c) Niger, (d) Zambezi, and (e) Orange river basins.
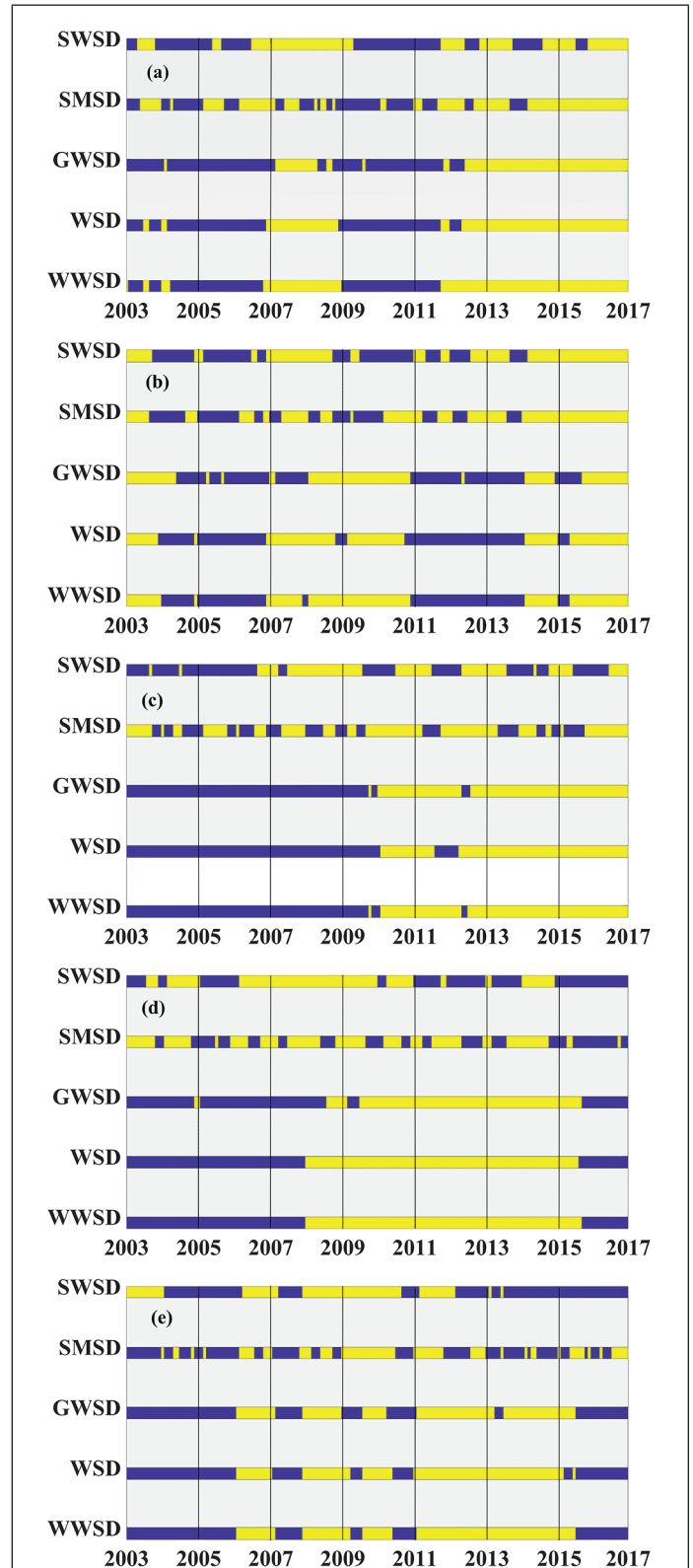
Figure 7. Temporal extents of identified drought events based on water storage deficit (WSD), water components storage deficit (WCSD), and weighted water storage deficit (WWSD) in the (a) Nile, (b) Congo, (c) Niger, (d) Zambezi, and (e) Orange river basins. The yellow values denote wet month, while the dark blue values represent drought month.

Evaluation of WWSD Relative to WSD

As previously shown, different water components play different roles in response to drought events over the basins in the study. The findings of this article have implications for how to provide a more realistic drought evaluation considering the individual TWS components and their relative contributions to the drought index. Therefore, to further demonstrate the rationality behind utilizing WWSD in this study, the performance of WWSD and WSD in terms of drought events identification has been assessed an is shown in Figure 7. Despite both indicators appearing to behave similarly, the data show some discrepancies in the observed onset and drought duration between WWSD and WSD. For example, in the Nile basin (Figure 7a), WWSD recorded one drought between April 2004 and October 2006, whereas WSD monitored the drought from March 2004 to November 2006. In the Congo basin (Figure 7b), WSD detected a drought event from November 2008 to January 2009; however, WWSD failed to identify this event. This result indicates that WWSD has varied sensitivity to drought events compared to WSD. These discrepancies, however, are explained by the weight given to a single TWS component in the WWSD. In conclusion, these findings suggest that accounting the influencing roles of these components storage in drought index are expected to provide more accurate drought characteristics estimation over major basins in Africa.
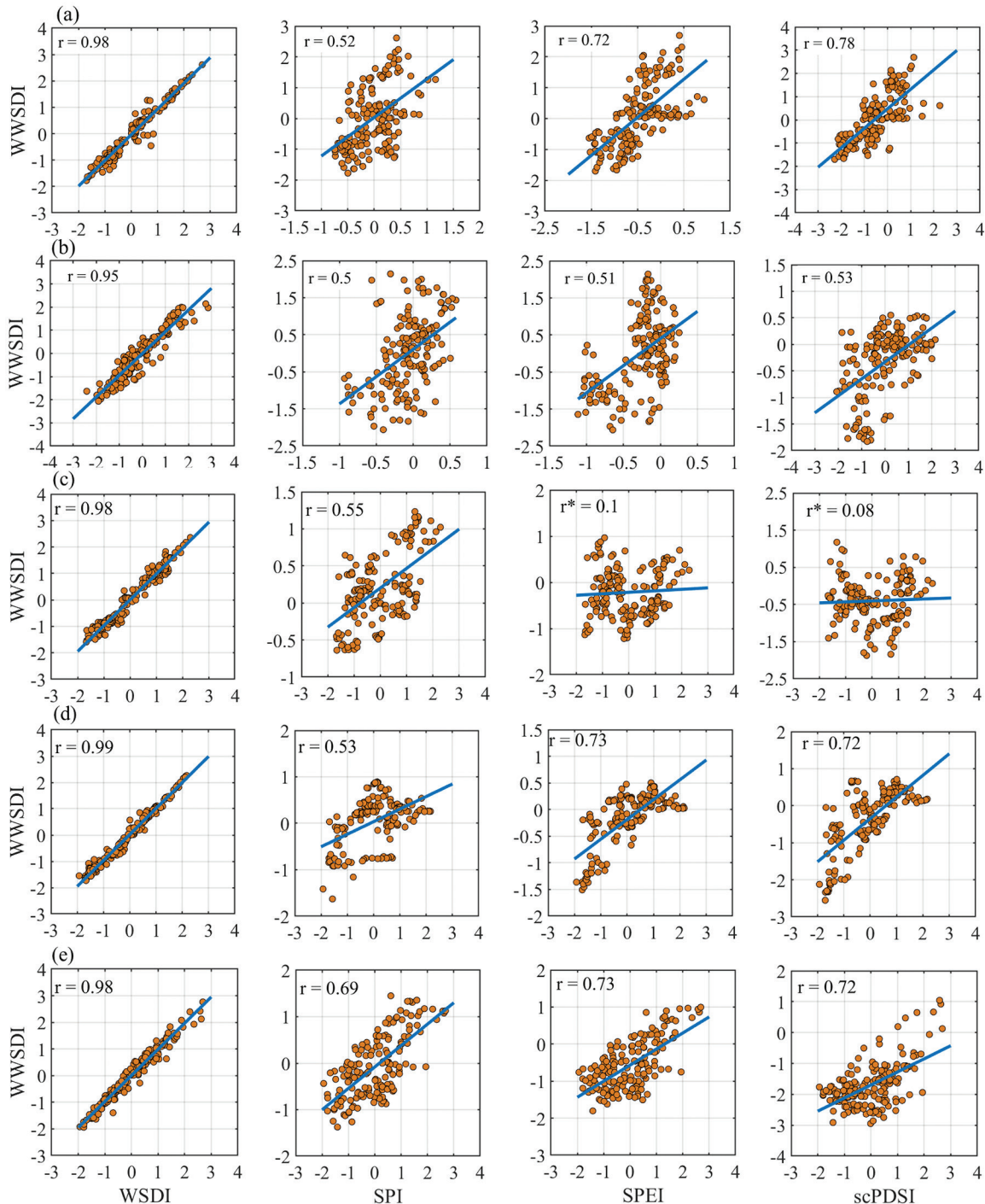
Figure 8. Scatterplots of correlation between the Weighted Water Storage Deficit Index (WWSDI) and Water Storage Deficit Index (WSDI), the Standardized Precipitation Index (SPI), the Standardized Precipitation Evapotranspiration Index (SPEI), and the self-calibrated Palmer Drought Severity Index (scPDSI) for the (a) Nile, (b) Congo, (c) Niger, (d) the Zambezi, and (e) Orange river basins. An asterisk indicates that the correlation is not significant.

WWSDI Identification of Droughts

In this study, the efficacy of WWSDI was identified by making comparisons with WSDI and other commonly used drought indices (i.e., SPI, SPEI, and scPDSI). The scatterplots in Figure 8 represent the correlation between WWSDI and WSDI, SPI, SPEI, and scPDSI over the five African river basins.

High positive correlations between WWSDI and WSDI are observed over the Nile, Congo, Niger, Zambezi, and Orange basins estimated at 0.98, 0.95, 0.98, 0.99, and 0.98, respectively. This strong relation between WWSDI and WSDI is due to their high sensitivity to GRACE TWS and the inclusion of TWS in their calculation procedures. However, the differences in correlation are attributed to the consideration of the weight of a single TWS component in WWSDI. WSDI is based on a single variable (GRACE TWSA); on the other hand, WWSDI is based on combining the TWS estimation from GRACE and WGHM using the CCR of individual TWS compartments as the weight. However, despite the fact that WWSDI and WSDI operate quite similarly, there is a distinction, as discussed in the previous section.

When comparing the WWSDI with other commonly used drought indices, we discovered that WWSDI is significantly correlated with SPI at a 0.05 significance level. The highest positive correlation (r = 0.69) between the two indices was observed in the Orange basin, while the lowest was detected in the Congo basin. WWSDI exhibited a significant correlation with the SPEI and scPDSI in the Nile, Congo, Zambezi, and Orange basins but a weak correlation in the Niger basin (Figure 8c).

In order to undertake a more thorough study, we further evaluated the temporal trends of these time series in Figure 9 in light of the fact that the association between the WWSDI and SPI, SPEI, and scPDSI was strongest in some situations while being less in others. As shown in Figure 9, the performance of WWSDI and its response to climate change correspond to the peaks and troughs of SPI, SPEI, and scPDSI over most basins. For example, all indicators showed that the biggest troughs occurred in the Orange basin in 2003 and across the Nile and Zambezi basins in 2006. However, in several cases, WWSDI was not fitting well with SPI, SPEI, and scPDSI; for example, the drought identified by WWSDI in 2004 over the Niger basin was not detected by SPI, SPEI, and scPDSI. The variations in relationships among SPI, SPEI, scPDSI, and WWSDI are most likely due to the differences in hydrological components and algorithms. For example, the high correlation between the scPDSI against WWSDI in the Nile basin reflects the significant influence of soil moisture on the TWS. Some recent studies also reported the significant correlation between soil moisture and TWS over the Nile basin (e.g., Abd-Elbaky and Jin 2019). In contrast, the weak correlation of SPEI and scPDSI with WWSDI in the Niger basin reveals that TWS was not much affected by evapotranspiration and soil moisture. In this context, the Niger basin was previously characterized as having a long-term high reduction in water storage between 2002 and 2008 (Ferreira *et al.* 2018), which corroborates our findings (Figure 7c). Thus, the availability of the stored water was less in the Niger basin, which affects the weak correlation of WWSDI against SPEI and scPDSI. Overall, WWSDI showed a good consistency with SPI, SPEI, and scPDSI in drought monitoring over most of the basins, which verifies the reliability of WWSDI in this study.

Analysis of Droughts in the Major Basins of Africa

Figure 10 displays the WWSDI-obtained droughts events for the major African basins from January 2003 to December 2016. Table 5 represents the magnitude, intensity, and duration characteristics of WWSDI for all the basins. The magnitude is calculated as accumulated WWSDI, and the intensity is calculated as the ratio of magnitude to duration (i.e., magnitude/duration) (Zargar *et al.* 2011; Wang *et al.* 2020).

Four drought events were detected in the Nile basin for 73 months during 2003, 2004–2006, and 2009–2011. In addition, two wet events occurred during 2006–2008 and 2011–2016; however, wet events became frequent after 2011. The most severe droughts (intensity of −1.15) occurred during 2004–2006 period, which is in line with the conclusions of previous studies conducted on the Nile basin (Hasan *et al.* 2021; Nigatu *et al.* 2021). The second and third severe drought events that took place during the 2009–2011 and 2003 regimes are consistent with the findings of Nigatu *et al.* (2021). However, in the current study, the results indicate that the identified drought episodes using WWSDI exhibited less magnitude than what was reported by Nigatu *et al.* (2021), who used WSDI. Moreover, the current study witnessed more recovery periods, particularly during the 2014–2016 period, than that of Nigatu *et al.* (2021). These differences can be attributed to the GRACE data period and to the fact that treating the weight of different TWS components equally may overestimate the severity and duration of drought conditions in the Nile basin. In the Congo basin, six drought events over 79 months were observed during the 2004, 2005–2006, 2007, 2010–2012, 2013–2014, and 2015 periods; in addition, five wet events were identified during the 2003–2004, 2008, 2009–2010, 2014, and 2015–2016 periods. The years 2010–2012 exhibited the highest frequency of droughts (with an intensity of −1.23). Our findings are in line with those of who observed the big drought occurrences that occurred over the Congo basin in 2005, 2006, and 2012. In the Niger basin, two prolonged drought episodes for 84 months were detected during 2003–2007 and 2007–2009; in addition, two significant wet events were observed between 2010–2011 and 2012–2016. However, after the 2009 period, there was a transition from dry to wet conditions. The severest drought event (intensity of −1.02) occurred during the 2003–2007 period, which is consistent with the findings of Ferreira *et al.* (2018), who carried out a study on the Niger basin. In the Zambezi basin, three drought events for 76 months were observed during the 2003–2004, 2005–2007, and 2015–2016 periods. Moreover, extended wet periods with water gain that began gradually in
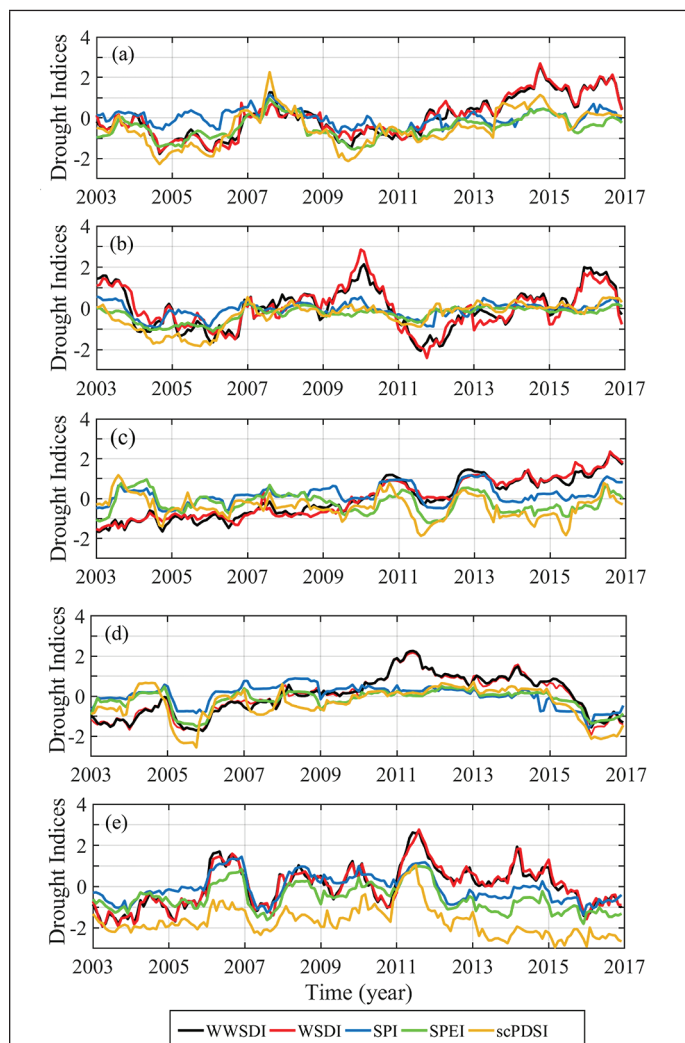
Figure 9. Time series of the Weighted Water Storage Deficit Index (WSDI), the Water Storage Deficit Index (WSDI), the Standardized Precipitation Index (SPI), the Standardized Precipitation Evapotranspiration Index (SPEI), and the self-calibrated Palmer Drought Severity Index (scPDSI) for the (a) Nile, (b) Congo, (c) Niger, (d) Zambezi, and (e) Orange river basins.
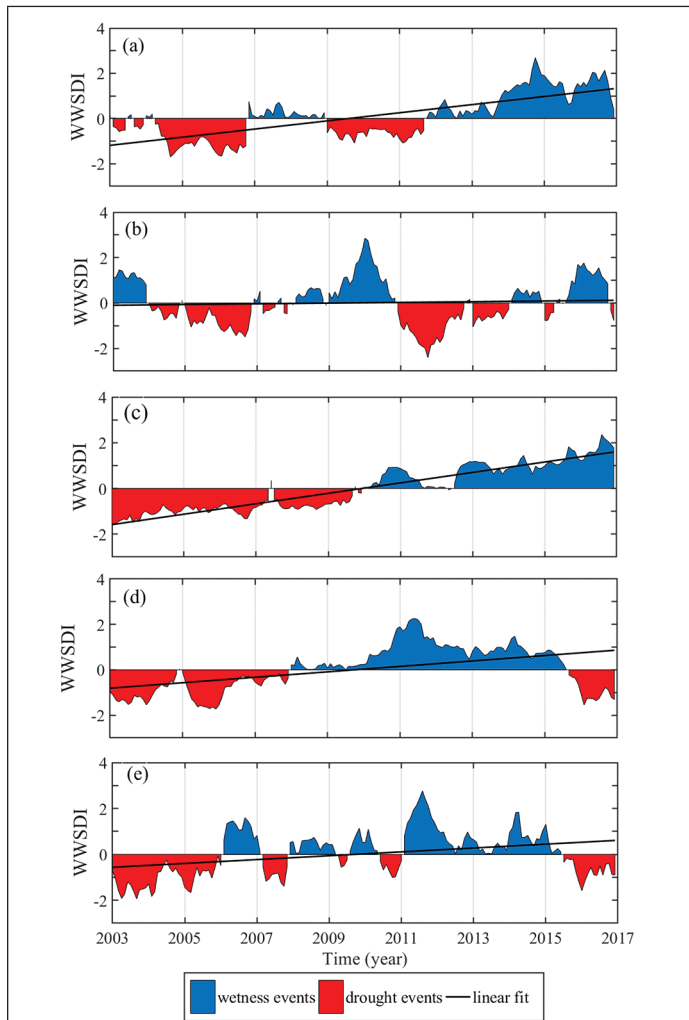
Figure 10. Drought events during 2003–2016 based on the Weighted Water Storage Deficit Index (WWSDI) for the (a) Nile, (b) Congo, (c) Niger, (d) Zambezi, and (e) Orange river basins.

Table 5. Drought characteristics in the major river basins in Africa identified by the Weighted Water Storage Deficit Index (WWSDI).

River Basin	No.	Period	Magnitude	Intensity	Duration
Nile	1	Feb 2003–Jun 2003	−2.39	−0.48	5
	2	Sep 2003–Dec 2003	−1.45	−0.36	4
	3	Apr 2004–Oct 2006	−35.78	−1.15	31
	4	Jan 2009–Sep 2011	−22.36	−0.68	33
Congo	1	Jan 2004–Nov 2004	−4.25	−0.39	11
	2	Jan 2005–Nov 2006	−24.85	−1.08	23
	3	Mar 2007–Jul 2007	−1.55	−0.31	5
	4	Dec 2010–Oct 2012	−28.40	−1.23	23
	5	Jan 2013–Jan 2014	−8.01	−0.62	13
	6	Jan 2015–Apr 2015	−2.38	−0.60	4
Niger	1	Jan 2003–May 2007	−54.01	−1.02	54
	2	Jul 2007– Dec 2009	−19.64	−0.65	30
Zambezi	1	Jan 2003– Dec 2004	−24.34	−1.02	24
	2	Jan 2005– Dec 2007	−28.62	−0.79	36
	3	Sep 2015– Dec 2016	−15.7	−0.98	16
Orange	1	Jan 2003– Jan 2006	−40.07	−1.08	37
	2	Mar 2007–Nov 2007	−8.50	−0.95	9
	3	Apr 2009–Jul 2009	−1.30	−0.32	4
	4	Jun 2010–Jan 2011	−5.05	−0.63	8
	5	Jul 2015– Dec 2016	−12.89	−0.72	18

2008 and greatly escalated from 2010 until the second half of 2015 were found. The severest drought event (intensity of −1.02) occurred during the 2003–2004 period. In their retrospective analysis of the Zambezi basin, Hulsman *et al.* (2021) equally confirmed that drought events occurred in the 2003–2004, 2005–2007, and 2015–2016 periods. In the Orange basin, five drought events over a total of 76 months were identified during the 2003–2006, 2007, 2009, 2010–2011, and 2015–2016 periods. In addition, four wet events were observed during the 2006, 2007–2008, 2009–2010, and 2011–2015 periods. The severest drought event (intensity of −1.08) occurred during 2003–2006. Additionally, the identified drought events over the region in 2004, 2005, 2007, 2011, and 2013 are in agreement with the findings of Masih *et al.* (2014).

The deviations in our drought evaluation results, along with those of previous studies, could be attributed to the period of the data sets and the utilized index method (WWSD). Our results indicated long-term drought occurrence from 2003 to 2006 over the Nile basin, from 2003 to 2009 over the Niger basin, and from 2003 to 2008 over the Zambezi basin, with the inclusion of few wetting months. This article's findings confirmed a general wetting tendency for the Nile, Niger, Zambezi, and Orange basins. Also, a mild trend (close to 0 mm) over the Congo basin was observed. The onset of the drought recovery period was consistent with the precipitation trends over the five river basins. However, considering the impacts of temperature increases, Africa's vulnerability to large-scale droughts may continue to increase (Ahmadalipour and Moradkhani 2018). The weather circulations in Africa have also been strongly influenced by large-scale atmospheric modes, such as the Indian Ocean Dipole (Anyah *et al.* 2018; Ni *et al.* 2018).

Discussion

Since GRACE observations can track changes in large-scale water storage, they are an essential tool in hydro-climatological investigations. Although established drought indices based on GRACE TWS (such as the WSDI and DSI) can identify vertically integrated water storage deficits, it can be challenging to estimate how much groundwater, surface water, or soil moisture deficits contribute to the overall water loss (Emerton *et al.* 2016). Thus, they reflect only integrated drought conditions, including groundwater drought. Furthermore, under the influence of climate change, the change characteristics (e.g., magnitude, variability, and duration) of each component are quite different (Wang *et al.* 2022). As a result, rather than evaluating all components as a whole, it is required to study the influence of each component separately in order to better comprehend the effects of climate change. In this study, a comprehensive drought index (WWSDI) was applied to evaluate drought events over the five large basins in Africa. The constructed index considers the contribution of a single component of the TWS deficit (i.e., surface, soil moisture, and groundwater) to the total water loss. The WWSDI has been successfully applied to the Yangtze basin as a case study scenario (Wang *et al.* 2020). Contextually, we determined a significant consistency among WWSDI and GRACE WSDI, SPI, SPEI, and scPDSI over the five African basins. This may indicate solid evidence on the applicability and capability of WWSDI over the river basins of Africa. Our research revealed that various TWS components contributed differently to TWS change and responded differently to drought patterns across all basins. Findings also provides more granular and differentiated information that can help improve researchers' knowledge of the hydrological factors and how they contribute to the overall characteristics of drought occurrences in the region. Therefore, it is seen to be more trustworthy to develop drought indices from GRACE when considering water components individually and in a differently weighted manner.

In order to provide decision makers with unique information for planning and management, we have, for the first time, evaluated the deficiency change of TWS components and their reaction to climate change in vast African basins. However, until this study was conducted, analysis of water components in major African river basins was uncommon or rare. We acknowledge that some shortcomings and uncertainties remain existed in this study. First, the WWSDI time series is only 13 years, which is insufficient to conclude a robust finding from a climatic perspective; however, longer-term data (at least 30 years) are needed to determine the baseline of the occurrence and severity

of water storage deficits (Liu *et al.* 2020). Furthermore, analysis of the severity of drought events based on three or more continuous negative values of WWSDI is not suitable for monitoring all drought events, particularly short-term drought (Wu *et al.* 2021). Additionally, it worth noting that using linear interpolation to fill the GRACE time series' missing values would also induce errors in drought estimation (Andam-Akorful *et al.* 2015; Sun *et al.* 2018). However, despite this approach being simple and widely used to handle missing data, other construction techniques, such as artificial neural networks, may provide more accurate data in the future (Ahmed *et al.* 2019).

Second, using WGHM outputs to separate water components from GRACE TWS might be subject to large uncertainty (Wang *et al.* 2020). Regarding the former, most of the existing global models, including WGHM and even local land surface models, are uncalibrated and unable to predict TWS components accurately, specifically groundwater storage (Hosseini-Moghari *et al.* 2020). This is mainly because of the intricate interplay between the aquifer and surface water hydrology. Nevertheless, Ferreira *et al.* (2020) introduced a unique reconstruction method that combines remotely sensed and modeled data in order to estimate the water compartments from TWS. This method may also improve the precision of WWSDI. Although GRACE measurements are found to be effective to monitor large- or global-scale drought, the resolutions of the GRACE observations are associated with certain limitations for use at the subbasin scale or submonthly time periods (Kumar *et al.* 2016; Li *et al.* 2019). Data assimilation techniques have been proposed in future studies to improve the limitations of the GRACE data and WWSDI estimates by assimilating the GRACE/FO observation into hydrological models. Thus, finer drought maps than of GRACE scale (around 150 000 km2 at midlatitudes) could be generated, which is crucial for accurate drought monitoring.

Conclusion

In recent decades, severe droughts have affected many river basins worldwide, causing environmental and social damage. Prioritizing adaptation measures requires drought evaluation over large river basins around the world. In this study, we generated the WWSDI based on combined TWS from GRACE and WGHM utilizing the CCR of each component as their weight to assess the occurrences of drought throughout the major African basins from January 2003 to December 2016. The main findings of the study are summarized as follows:

- Precipitation is the primary hydrologic input for the TWS change, and the distribution of both parameters showed a significant seasonal change in the five river basins.
- Regarding CCR, SMS and SWS rank the second and third, while GWS change ranks the first and accounts for 56%, 61%, 47%, 64%, and 78% of TWS change in the Nile, Congo, Niger, Zambezi, and Orange basins, respectively. These results showed that different water components contribute distinctly to TWS change over those basins.
- According to WCSD and WCSDI distribution, different water components play different roles in response to drought events in the basins. The WSDI, SPI, SPEI, and scPDSI are correlated significantly against WWSDI over the Nile, Congo, Zambezi, and Orange basins. In the Niger basin, SPI is significantly correlated with WWSDI. Overall, our findings indicate that the WWSDI can successfully detect drought events over major basins in Africa.
- Based on WWSDI, the most severe droughts occurred in 2006, 2012, 2006, 2006, and 2003 in the Nile, Congo, Niger, Zambezi, and Orange basins, respectively. A significant wetting tendency was detected over the Nile, Niger, Zambezi, and Orange basins, while a mild trend was observed in the Congo basin.

The study of this nature may be helpful to policymakers and managers with seeking to promote sustainable water resource management and development

References

Abd-Elbaky, M. and S. Jin. 2019. Hydrological mass variations in the Nile River Basin from GRACE and hydrological models. *Geodesy and Geodynamics* 10:430–438.

Abiodun, B. J.; N. Makhanya, B. Petja, A. A. Abatan, P. G. Oguntunde. 2019. Future projection of droughts over major river basins in Southern Africa at specific global warming levels. *Theoretical and Applied Climatology.*, 137, 1785–1799.

AghaKouchak, A., D. Feldman, M. Hoerling, T. Huxman, J. Lund. 2015. Water and climate: Recognize anthropogenic drought. *Nature.*, 524, 409–411.

Ahmadalipour, A. and H. Moradkhani. 2018. Multi-dimensional assessment of drought vulnerability in Africa: 1960–2100. *Science of the Total Environment* 644:520–535.

Ahmed, M., M. Sultan, T. Elbayoumi, and P. Tissot. 2019. Forecasting GRACE data over the africanwatsheds using artificial neural networks. *Remote Sensing* 11:1769.

Andam-Akorful, S. A., V. G. Ferreira, J. L. Awange, E. Forootan, and X. F. He. 2015. Multi-model and multi-sensor estimations of evapotranspiration over the Volta Basin, West Africa. *International Journal of Climatology* 35:3132–3145.

Anyah, R. O., E. Forootan, J. L. Awange, and M. Khaki. 2018. Understanding linkages between global climate indices and terrestrial water storage changes over Africa using GRACE products. *Science of the Total Environment* 635:1405–1416.

Awange, J. L.; V. G. Ferreira, E. Forootan, Khandu, S. A. Andam-Akorful, N. O. Agutu, X. F. He. 2016. Uncertainties in remotely sensed precipitation data over Africa. *International Journal of Climatology.*, 36, 303–323.

Cui, A., J. Li, Q. Zhou, R. Zhu, H. Liu, G. Wu, Q. Li. 2021. Use of a multiscalar GRACE-based standardized terrestrial water storage index for assessing global hydrological droughts. *Journal of Hydrology.*, 603, 126871.

Dobardzic, S., C. G. Dengel, A. M. Gomes, J. Hansen, M. Bernardi, M. Fujisawa, and J. Intsiful. 2019. *2019 State of Climate Services: Agriculture and Food Security.* Geneva: World Meteorological Organization.

Emerton, R. E., E. M. Stephens, F. Pappenberger, T. C. Pagano, A. H. Weerts, A. W. Wood, P. Salamon, J. D. Brown, N. Hjerdt, C. Donnelly, C. A. Baugh, and H. L. Cloke. 2016. Continental and global scale flood forecasting systems. *Wiley Interdisciplinary Reviews: Water* 3:391–418.

Ferreira, V., Z. Asiah, J. Xu, Z. Gong, and S. Andam-Akorful. 2018. Land water-storage variability over West Africa: Inferences from space-borne sensors. *Water* 10:380.

Ferreira, V. G., B. Yong, M. J. Tourian, C. E. Ndehedehe, Z. Shen, K. Seitz, and K. Dannouf. 2020. Characterization of the hydro-geological regime of Yangtze River basin using remotely-sensed and modeled products. *Science of the Total Environment* 718:137354.

Forootan, E., M. Khaki, M. Schumacher, V. Wulfmeyer, N. Mehrnegar, A.I.J.M. van Dijk, L. Brocca, S. Farzaneh, F. Akinluyi, G. Ramillien, C. K. Shum, J. Awange, and A. Mostafaie. 2019. Understanding the global hydrological droughts of 2003–2016 and their relationships with teleconnections. *Science of the Total Environment* 650:2587–2604.

Hasan, E., A. Tarhule, and P. E. Kirstetter. 2021. Twentieth and twenty-first century water storage changes in the Nile River Basin from GRACE/GRACE-FO and modeling. *Remote Sensing* 13:953.

Hassan, A. A. and S. Jin. 2014. Lake level change and total water discharge in East Africa Rift Valley from satellite-based observations. *Global and Planetary Change* 117:79–90.

Hosseini-Moghari, S. M., S. Araghinejad, K. Ebrahimi, Q. Tang, and A. AghaKouchak. 2020. Using GRACE satellite observations for separating meteorological variability from anthropogenic impacts on water availability. *Scientific Reports* 10:1–12.

Huang, Z., P.J.F. Yeh, Y. Pan, J. J. Jiao, H. Gong, X. Li, A. Güntner, Y. Zhu, C. Zhang, and L. Zheng. 2019. Detection of large-scale groundwater storage variability over the karstic regions in Southwest China. *Journal of Hydrology* 569:409–422.

Huffman, G. J., R. F. Adler, D. T. Bolvin, G. Gu, E. J. Nelkin, K. P. Bowman, Y. Hong, E. F. Stocker, and D. B. Wolff. 2007. The TRMM Multisatellite Precipitation Analysis (TMPA): Quasi-global, multiyear, combined-sensor precipitation estimates at fine scales. *Journal of Hydrometeorology* 8:38–55.

Hulsman, P., H.H.G. Savenije, and M. Hrachowitz. 2021. Satellite-based drought analysis in the Zambezi River Basin: Was the 2019 drought the most extreme in several decades as locally perceived? *Journal of Hydrology: Regional Studies* 34:100789.

IPCC. 2018. An IPCC special report on the impacts of global warming of 1.5 °C above preindustrial levels and related global greenhouse gas emission pathways. *Special Report, Intergovernmental Panel on Climate Change*, 175–311.

IPCC. 2022. Contribution of Working Group II to the Sixth Assessment Report of the Intergovernmental Panel on Climate Change. Cambridge University Press. In Press., 1–225.

Jiao, W., L. Wang, and M. F. McCabe. 2021. Multi-sensor remote sensing for drought characterization: Current status, opportunities and a roadmap for the future. *Remote Sensing of Environment* 256:112313.

Jin, S. and T. Zhang. 2016. Terrestrial water storage anomalies associated with drought in southwestern USA from GPS observations. *Surveys in Geophysics* 37:1139–1156.

Jin, S., L. J. Zhang, and B. D. Tapley. 2011. The understanding of length-of-day variations from satellite gravity and laser ranging measurements. *Geophysical Journal International* 184:651–660.

Khaki, M., E. Forootan, M. Kuhn, J. Awange, L. Longuevergne, and Y. Wada. 2018. Efficient basin scale filtering of GRACE satellite products. *Remote Sensing of Environment* 204:76–93.

Khorrami, B. and O. Gunduz. 2021. An enhanced water storage deficit index (EWSDI) for drought detection using GRACE gravity estimates. *Journal of Hydrology*., 603, 126812.

Kumar, S. V., B. F. Zaitchik, C. D. Peters-Lidard, M. Rodell, R. Reichle, B. Li, M. Jasinski, D. Mocko, A. Getirana, G. De Lannoy, M. H. Cosh, C. R. Hain, M. Anderson, K. R. Arsenault, Y. Xia, and M. Ek. 2016. Assimilation of gridded GRACE terrestrial water storage estimates in the North American land data assimilation system. *Journal of Hydrometeorology* 17:1951–1972.

Leblanc, M. J., P. Tregoning, G. Ramillien, S.O. Tweed, and A. Fakes. 2009. Basin-scale, integrated observations of the early 21st century multiyear drought in southeast Australia. *Water Resources Research* 45:1–4.

Li, B., M. Rodell, S. Kumar, H. K. Beaudoing, A. Getirana, B. F. Zaitchik, L. G. de Goncalves, C. Cossetin, S. Bhanja, A. Mukherjee, S. Tian, N. Tangdamrongsub, D. Long, J. Nanteza, J. Lee, F. Policelli, I. B. Goni, D. Daira, M. Bila, G. Lannoy, D. Mocko, S. Steele-Dunne, H. Save, S. Bettaetdpur. 2019. Global GRACE data assimilation for groundwater and drought monitoring: Advances and challenges. *Water Resources Research* 55:7564–7586.

Liu, X., X. Feng, P. Ciais, B. Fu, B. Hu, and Z. Sun. 2020. GRACE satellite-based drought index indicating increased impact of drought over major basins in China during 2002–2017. *Agricultural and Forest Meteorology* 291:108057.

Lopez, T., A. Al Bitar, S. Biancamaria, A. Güntner, and A. Jäggi. 2020. On the use of satellite remote sensing to detect floods and droughts at large scales. *Surveys in Geophysics* 41:1461–1487.

Masih, I., S. Maskey, F.E.F. Mussá, and P. Trambauer. 2014. A review of droughts on the African continent: A geospatial and long-term perspective. *Hydrology and Earth System Sciences* 18:3635–3649.

Mekonnen, K., A. M. Melesse, and T. A. Woldesenbet. 2022. How suitable are satellite rainfall estimates in simulating high flows and actual evapotranspiration in MelkaKunitre catchment, Upper Awash Basin, Ethiopia? *Science of the Total Environment* 806:150443.

Mgquba, S. K. and S. Majozi. 2020. Climate change and its impacts on hydro-politics in transboundary basins: A case study of the orange-senqu river basin. *Journal of Water and Climate Change* 11:150–165.

Modanesi, S., C. Massari, S. Camici, L. Brocca, and G. Amarnath. 2020. Do satellite surface soil moisture observations better retain information about crop-yield variability in drought conditions? *Water Resources Research* 56:e2019WR025855.

Müller Schmied, H., D. Caceres, S. Eisner, M. Flörke, C. Herbert, C. Niemann, T. Asali Peiris, E. Popat, F. Theodor Portmann, R. Reinecke, M. Schumacher, S. Shadkam, C. E. Telteu, T. Trautmann, and P. Döll. 2021. The global water resources and use model WaterGAP v2.2d: Model description and evaluation. *Geoscientific Model Development* 14:1037–1079.

Munday, C. and R. Washington. 2019. Controls on the diversity in climate model projections of early summer drying over southern Africa. *Journal of Climate* 32:3707–3725.

Ndehedehe, C. E.; J. L. Awange, M. Kuhn, N. O. Agutu, Y. Fukuda. 2017. Climate teleconnections influence on West Africa's terrestrial water storage. *Hydrological Processes*., 31, 3206–3224.

Ndehedehe, C. E., J. L. Awange, N. O. Agutu, and O. Okwuashi. 2018. Changes in hydro-meteorological conditions over tropical West Africa (1980–2015) and links to global climate. *Global and Planetary Change* 162:321–341.

Ndehedehe, C. E.; R. O. Anyah, D. Alsdorf, N. O. Agutu, V. G. Ferreira. 2019. Modelling the impacts of global multi-scale climatic drivers on hydro-climatic extremes (1901–2014) over the Congo basin. *Science of The Total Environment*., 651, 1569–1587.

Ndehedehe, C. E., V. G. Ferreira, A. O. Onojeghuo, N. O. Agutu, E. Emengini, and A. Getirana. 2020. Influence of global climate on freshwater changes in Africa's largest endorheic basin using multi-scaled indicators. *Science of the Total Environment* 737:139643.

Ni, S., J. Chen, C. R. Wilson, J. Li, X. Hu, and R. Fu. 2018. global terrestrial water storage changes and connections to ENSO events. *Surveys in Geophysics* 39:1–22.

Nigatu, Z. M., D. Fan, W. You, and A. M. Melesse. 2021. Hydroclimatic extremes evaluation using GRACE/GRACE-FO and multidecadal climatic variables over the Nile River Basin. *Remote Sensing* 13:651.

Oguntunde, P. G.; G. Lischeid, B. J. Abiodun. 2018. Impacts of climate variability and change on drought characteristics in the Niger River Basin, West Africa. *Stochastic Environmental Research and Risk Assessment*., 32, 1017–1034.

Omer, A., M. Zhuguo, Z. Zheng, and F. Saleem. 2020. Natural and anthropogenic influences on the recent droughts in Yellow River Basin, China. *Science of the Total Environment* 704:135428.

Papa, F., J. F. Crétaux, M. Grippa, E. Robert, M. Trigg, R. M. Tshimanga, B. Kitambo, A. Paris, A. Carr, A. S. Fleischmann, M. de Fleury, P. G. Gbetkom, B. Calmettes, and S. Calmant. 2022. Water resources in Africa under global change: Monitoring surface waters from space. *Surveys in Geophysics* 4:1–51.

Running, S., Q. Mu, M. Zhao, and A. Moreno. 2017. MOD16A2—MODIS/Terra Net Evapotranspiration 8-Day L4 Global 500m SIN Grid V006 [Data set]. *NASA EOSDIS Land Processes DAAC* 1.5:34.

Sarfo, I., B. Shuoben, L. Beibei, S.O.Y. Amankwah, E. Yeboah, J. E. Koku, E. K. Nunoo, and C. Kwang. 2022. Spatiotemporal development of land use systems, influences and climate variability in southwestern Ghana (1970–2020). *Environment, Development and Sustainability* 24:9851–9883.

Satish Kumar, K.; E. Venkata Rathnam, V. Sridhar. 2021. Tracking seasonal and monthly drought with GRACE-based terrestrial water storage assessments over major river basins in South India. *Science of The Total Environment*., 763, 142994.

Schlosser, C. A., K. Strzepek, X. Gao, C. Fant, É. Blanc, S. Paltsev, H. Jacoby, J. Reilly, and A. Gueneau. 2014: The future of global water stress: An integrated assessment. *Earth's Future* 2:341–361.

Sun, Z., X. Zhu, Y. Pan, J. Zhang, and X. Liu. 2018. Drought evaluation using the GRACE terrestrial water storage deficit over the Yangtze River Basin, China. *Science of the Total Environment* 634:727–738.

Thomas, A. C.; J. T. Reager, J. S. Famiglietti, M. Rodell. 2014. A GRACE-based water storage deficit approach for hydrological drought characterization. *Geophysical Research Letters*., 41, 1537–1545.

United Nations Environment Programme. 2010. Africa water atlas, 1, 1–336.

Vicente-Serrano, S. M., S. Beguería, L. Gimeno, L. Eklundh, G. Giuliani, D. Weston, A. El Kenawy, J. I. López-Moreno, R. Nieto, T. Ayenew, D. Konte, J. Ardö, and G.G.S. Pegram. 2012. Challenges for drought mitigation in Africa: The potential use of geospatial data and drought information systems. *Applied Geography* 34:471–486.

Wang, J., Y. Chen, Z. Wang, and P. Shang. 2020. Drought evaluation over Yangtze River basin based on weighted water storage deficit. *Journal of Hydrology* 591:125283.

Wang, L., J. Wang, L. Wang, L. Zhu, and X. Li. 2022. Terrestrial water storage regime and its change in the endorheic Tibetan Plateau. *Science of the Total Environment* 815:152729.

Wells, N., S. Goddard, and M. J. Hayes. 2004. A self-calibrating Palmer Drought Severity Index. *Journal of Climate* 17:2335–2351.

West, H., N. Quinn, and M. Horswell. 2019. Remote sensing for drought monitoring and impact assessment: Progress, past challenges and future opportunities. *Remote Sensing of Environment* 232:111291.

Wu, T., W. Zheng, W. Yin, and H. Zhang. 2021. Spatiotemporal characteristics of drought and driving factors based on the GRACE-derived total storage deficit index: A case study in Southwest China. *Remote Sensing* 13:79.

Yang, P., J. Xia, C. Zhan, Y. Qiao, and Y. Wang. 2017. Monitoring the spatio-temporal changes of terrestrial water storage using GRACE data in the Tarim River basin between 2002 and 2015. *Science of the Total Environment* 595:218–228.

Zargar, A., R. Sadiq, B. Naser, and F. I. Khan. 2011. A review of drought indices. *Environmental Reviews* 19:333–349.

Zhang, B., E. Zhang, L. Liu, S. A. Khan, T. van Dam, Y. Yao, M. Bevis, and V. Helm. 2018. Geodetic measurements reveal short-term changes of glacial mass near Jakobshavn Isbræ (Greenland) from 2007 to 2017. *Earth and Planetary Science Letters* 503:216–226.

Zhang, Y., B.I.N. He, L. Guo, and D. Liu. 2019. Differences in response of terrestrial water storage components to precipitation over 168 global river basins. *Journal of Hydrometeorology* 20:1981–1999.

Lightweight Parallel Octave Convolutional Neural Network for Hyperspectral Image Classification

Dan Li, Hanjie Wu, Yujian Wang, Xiaojun Li, Fanqiang Kong, and Qiang Wang

Abstract

Although most deep learning-based methods have achieved excellent performance for hyperspectral image (HSI) classification, they are often limited by complex networks and require massive training samples in practical applications. Therefore, designing an efficient, lightweight model to obtain better classification results under small samples situations remains a challenging task. To alleviate this problem, a novel, lightweight parallel octave convolutional neural network (LPOCNN) for HSI classification is proposed in this paper. First, the HSI data is preprocessed to construct two three-dimensional (3D) patch cubes with different spatial and spectral scales for each central pixel, removing redundancy and focusing on extracting spatial features and spectral features, respectively. Next, two non-deep parallel branches are created for the two inputs, which design octave convolution rather than classical 3D convolution to facilitate light weighting of the model. Then two-dimensional convolutional neural network is used to extract deeper spectral-spatial features when fusing spectral-spatial features from different parallel layers. Moreover, the spectral-spatial attention is designed to promote the classification performance even further by adaptively adjusting the weights of different spectral-spatial features according to their contribution to classification. Experiments show that our suggested LPOCNN acquires a significant advantage on classification performance over other competitive methods under small sample situations.

Introduction

Hyperspectral image (HSI) is acquired by an imaging spectrometer with high spectral resolution and contains multiple dense and continuous narrow band his. HSI is a three-dimensional cube that records both spatial and rich spectral information of ground objects and accurately reflects the spatial and spectral characteristics of the target (Vantaram *et al.* 2015; Zabalza *et al.* 2015; Zhang *et al.* 2019). Therefore, the advantage of providing rich spectral-spatial information makes HSI play a rather important role in various fields, such as land cover classification (Hosseini *et al.* 2012; Khan *et al.* 2018), mineral exploration (Du *et al.* 2016; Peyghambari and Zhang 2021), military reconnaissance (Bitar *et al.* 2019), and environmental detection (Ghamisi *et al.* 2018; Yu *et al.* 2021a). In these above HSI applications, there is such a fundamental problem as HSI classification (Chen *et al.* 2014; Fauvel *et al.* 2013; He *et al.* 2018; Prabukumar *et al.* 2018), aiming to classify all the pixels in HSI to confirm their true categories.

In the past decades, various traditional HSI classifiers based on manually extracted features have been introduced. However, HSI classification faces a challenge called "curse of dimensionality" because

of the high-dimensional nature of HSI. To address the above challenge, researchers propose a series of dimensionality reduction methods for HSI classification, e.g., principal component analysis (PCA) (Kang *et al.* 2017), the maximum noise fraction (He *et al.* 2019), and band selection (Wang *et al.* 2017). These dimensionality reduction algorithms mentioned above map the high-dimensional HSI to the lower-dimensional feature space while retaining distinguishability between different land-cover classes. In general, there are two main classes of traditional HSI classifiers according to whether they use spatial context information: (1) HSI classification methods based on spectral information only, e.g., random forest (Crawford *et al.* 2004; Ham *et al.* 2005; Xia *et al.* 2016b), extreme learning machine (Yu *et al.* 2021b), and support vector machines (SVM) (Heydari and Mountrakis 2019; Tarabalka *et al.* 2010; Xia *et al.* 2016a; Yan *et al.* 2013); (2) HSI classification methods based on spectral-spatial information, e.g., extended morphological profiles (Dalla Mura *et al.* 2011; Wu *et al.* 2017), SVM with composite kernels (SVMCK) (Camps-Valls *et al.* 2006; Marconcini *et al.* 2009; Peng *et al.* 2015), the joint sparse representation classifiers (Cao *et al.* 2019), and 3D-Gabor phase coding classifiers (Chen *et al.* 2021). However, all these classification algorithms mentioned above require hand-designed feature extraction strategies to obtain easily distinguishable features, and the performance of these classification algorithms also depends on the researchers' experience working in the field of HSI classification. Therefore, designing an effective traditional hyperspectral classification algorithm takes a lot of time.

Recently, deep learning-based methods (Audebert *et al.* 2019; Guo and Zhu 2021; Liu *et al.* 2017; Ma *et al.* 2015) have demonstrated excellent practical achievements for HSI classification since they can automatically learn nonlinear deep semantic features of complex data without manually designing feature extraction strategies. The stacked autoencoder (SAE) (Chen *et al.* 2014) pioneers his exploration of deep learning algorithms for HSI classification, followed closely by deep belief networks (DBN) (Chen *et al.* 2015). However, the classification results achieved are limited when applying SAE and DBN to HSI classification, because they require the input data format to be one-dimensional, resulting in a large amount of discarded useful information. To solve this problem, convolutional neural network (CNN) (Chen *et al.* 2017; Hu *et al.* 2015; Liu *et al.* 2018; Yu *et al.* 2018) is applied to HSI classification by researchers. It can automatically extract deep spectral and spatial features with multiple convolutional layers and achieve good classification results when applied to HSI classification. At first, researchers apply two-dimensional CNN (2DCNN) (Bhatti *et al.* 2022; Salman and Yuksel 2016; Song *et al.* 2018) to HSI classification, and then propose three-dimensional CNN (3DCNN) (Feng *et al.* 2019; Kang and Kim 2021; Liu *et al.* 2018) that is more suitable for three-dimensional hyperspectral images. 3DCNN can select a 3D block around the central pixel as the input of this network and can explore 3D spectral-spatial features of HSI concurrently. Nevertheless, there is a problem of gradient disappearance when training deeper 2DCNN or 3DCNN. To alleviate this problem, residual learning is introduced into CNN-based HSI classification networks. The spectral–spatial residual network (SSRN)

Dan Li, Hanjie Wu, Yujian Wang, and Fanqiang Kong are with the College of Astronautics, Nanjing University of Aeronautics and Astronautics, Nanjing 210016, China (wuhanjie@nuaa.edu.cn).

Xiaojun Li is with the National Key Laboratory Science and Technology Space Microwave, China Academic Space Technology, Xian 710018, China.

Qiang Wang is with the Control Science and Engineering, Harbin Institute of Technology, Harbin 150001, China.

(Zhong *et al.* 2018) is proposed to address the pitfall of gradient disappearance by introducing residual learning into the 3DCNN. Pu *et al.* (2021) applies graph convolution networks to HSI classification, which can act directly on hyperspectral maps and use their structural information. However, there is still a challenge of how to convert hyperspectral images into graph structures and uncover the connections between different nodes in the graph. Lei *et al.* (2021) propose deep convolutional capsule neural network, which introduces the capsule structure into convolutional neural networks to retain useful location information for classification tasks that is lost in traditional CNNs.

Currently, a new convolution strategy is proposed by Chen *et al.* (2019), which is octave convolution. They consider that not only images in the natural world comprise low-frequency and high-frequency channels, but also the feature map in CNN comprises both low-frequency channels and high-frequency channels where the former contains global information about the image and the latter contains detailed information about the image. Xu *et al.* (2020) therefore applies octave convolution to HSI classification, effectively alleviating the spatial redundancy problem by dividing the frequency of the image and then halving the low-frequency information in the image. But this approach still demands massive training samples due to using multi-scale convolutional networks which adds numerous network parameters. Zhu *et al.* (2021) introduce the attention mechanism into the residual network to emphasize the features that contribute more to the classification. Despite the promising classification performance achieved by the deep learning-based methods described above, they still have a disadvantage of requiring massive training samples when used for real-world scenarios. These deep networks above need to tune numerous parameters, so massive labeled samples are necessary to train these deep networks. However, obtaining labeled samples for hyperspectral images can be very expensive in practice, which means that we only have a very limited number of labeled samples available. These methods will have overfitting problems under small sample situations due to so few training samples and too many network parameters, which leads to undesirable classification results. Therefore, it is still a challenging task to design an efficient lightweight network to alleviate the requirement for the number of labeled samples and to obtain better classification results under small sample situations.

In this paper, a novel lightweight parallel octave convolutional neural network (LPOCNN) for HSI classification is proposed. First, the HSI data is preprocessed to construct two 3D patch cubes with different spatial and spectral scales for each central pixel, removing redundancy and focusing on extracting spatial features and spectral features respectively. Next, two non-deep parallel branches are created for the two inputs, which design octave convolution rather than classical 3D convolution to facilitate light weighting of the model. Then 2DCNN is used to extract deeper spectral-spatial features when fusing spectral-spatial features from different parallel layers. Moreover, we also design the spectral-spatial attention to promote the classification performance even further, by adaptively adjusting the weights of different spectral-spatial features according to their contribution to classification. Eventually, fused and adjusted discriminative features enter fully connected networks to get the final classification results. Experiments are conducted on three publicly available hyperspectral data sets and the results show that our suggested LPOCNN acquires a significant advantage on classification performance over other competitive methods under small sample situations.

The major contributions in our work are outlined below:
(1) We construct two 3D inputs with different spatial and spectral scales for the two parallel branches, removing redundancy and focusing on extracting spatial and spectral features separately.
(2) To alleviate the requirement for massive, labeled samples, two non-deep parallel branches are created for the two inputs, which design octave convolution rather than one single deep convolutional branch to facilitate the light weighting of the model.
(3) Also in the feature fusion stage, we design the spectral-spatial attention to promote the classification performance even further,

by adaptively adjusting the weights of different spectral-spatial features according to their contribution to classification.

The remaining sections of the article are structured below. 2DCNN, 3DCNN, and attention mechanism are described in the section "Related Works" to review related work. The flowchart and the specific process of our suggested LPOCNN method are presented in the section "Proposed Methods". The classification results for three publicly available HSI data sets are given in the section "Experiments and Analysis". The conclusion of our work is offered in the last section.

Related Works

2D and 3D Convolution

With their superior performance in the field of computer vision, convolutional neural networks (Gu *et al.* 2018; Liu *et al.* 2015; Makantasis *et al.* 2015) are increasingly applied in visual image processing. In practical applications, there are two most representative structures of convolutional neural networks, 2DCNN (Karim *et al.* 2018) and 3DCNN (Ben Hamida *et al.* 2018) , which can be illustrated in Figure 1. And the formulas of 2D convolution and 3D convolution can be expressed as follows:

$$q_{ij}^{xy} = f\left(\sum_m \sum_{h=1}^{H} \sum_{w=1}^{W} k_{ijm}^{hw} q_{(i-1)m}^{(x+h)(y+w)} + b_{ij} \right) \qquad (1)$$

$$q_{ij}^{xyz} = f\left(\sum_m \sum_{h=1}^{H} \sum_{w=1}^{W} \sum_{r=1}^{R} k_{ijm}^{hwr} q_{(i-1)m}^{(x+h)(y+w)(z+r)} + b_{ij} \right) \qquad (2)$$

where m denotes the index of the feature map in layer $(i–1)$. H, W, and R represent the size of the convolution kernel, k_{ijm}^{hw} denotes the weight of the jth convolution kernel at position (h, w, r) on the mth feature map in layer i, and b_{ij} means the bias.

From Figure 1, we can clearly see that 2D convolution operation only considers the spatial correlation of each feature map in the image, so it lacks the information of the relationship between channels. In contrast, 3D convolution overcomes the shortcomings of 2D convolution and is able to simultaneously extract the 3D features by 3D convolution kernels, but makes the model complex and requires more computational cost. Therefore, using only 3DCNN or 2DCNN is not the best choice for 3D inputs such as hyperspectral images.

Attention Mechanism

Attention mechanism (Chen *et al.* 2016; Liang *et al.* 2019; Xu *et al.* 2018) is a mimicry of the human visual attention mechanism, which is essentially a resource allocation mechanism. Human visual attention can receive a region on a picture at high resolution and perceive its surrounding regions at low resolution. In other words, human eyes find a target region to focus on with a quick scan of global images and then allocates more attention to this region, aiming to acquire more insightful information about the target but ignore other irrelevant information. Attention mechanism is inspired by this and aims to automatically learn locally important features in an image through a deep network. Attention mechanism models the interdependencies between features and then uses a neural network to generate a mask. The values on the mask represent the weight of various areas on feature maps, and
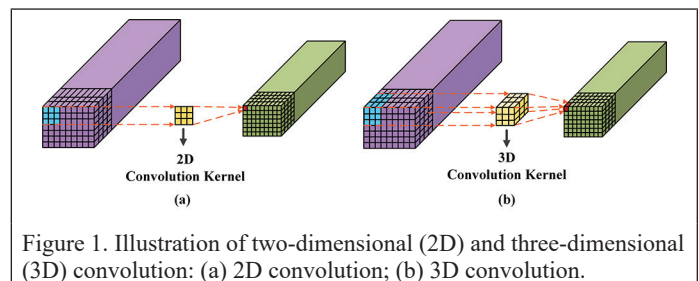

Figure 1. Illustration of two-dimensional (2D) and three-dimensional (3D) convolution: (a) 2D convolution; (b) 3D convolution.

then the importance of different regions on feature maps is adaptively reclassified based on the weight values.

Proposed Methods

The flowchart of our proposed method is shown in Figure 2, and the main steps are briefly described as follows.

Construction of Inputs with Different Scale

To fully mine the spatial and spectral information contained in original HSI data set, two inputs with different scale are constructed for each pixel. Suppose the HSI data set be denoted as $\chi \in \mathbb{R}^{H \times W \times D}$, where H, W, and D mean the spatial height, spatial width and the number of spectral bands, respectively. The details of how to construct two inputs with different scale are explained below.

(1) Dimensionality reduction. The PCA method is firstly applied on the original HSI data set to remove redundancy and reduce computing complexity. By PCA, two data sets with different number of the reduced spectral dimension are obtained, where $\gamma \in \mathbb{R}^{H \times W \times D_1}$ and $\gamma \in \mathbb{R}^{H \times W \times D_2}$, R_1, R_2 are the number of reduced spectral dimension in γ and λ, respectively.

(2) Two inputs with different scale. Suppose that γ contains l pixels $X = [x_1, x_2, \ldots, x_l] \in \mathbb{R}^{1 \times 1 \times R_1}$. For a pixel x_i in X, $i = 1, \ldots, l$, its corresponding 3D patch cubes $S_e \in \mathbb{R}^{A_1 \times A_1 \times R_1}$ can be formed by neighboring cubes centered at the pixel x_i, where A_1 is the width of the 3D patch cube S_e. Similarly, suppose that λ contains l pixels $Y = [y_1, y_2, \ldots, y_l] \in \mathbb{R}^{1 \times 1 \times R_2}$. For a pixel x_j in Y, $j = 1, \ldots, l$, its corresponding 3D patch cubes $S_a \in \mathbb{R}^{A_2 \times A_2 \times R_2}$ can be formed by neighboring cubes centered at the pixel x_j, where A_2 is the width of 3D patch cube S_a. Moreover, as shown in Figure 2, it is notable that S_e has more spectral dimensions, but it has a smaller spatial window, aiming to focus more on extracting the spectral information. In contrast, S_a has a larger spatial window, but it has fewer spectral dimensions aiming to focus more on extracting spatial information.

Therefore, we construct two 3D patch cubes with different spatial and spectral scales for each central pixel, removing redundancy and focusing on extracting spatial features and spectral features, respectively.

Non-Deep Parallel Branches with Octave Convolution

We consider that the feature map in CNN comprises both low-frequency channels and high-frequency channels just like natural images, where the former contains global information about the image and the latter contains detailed information about the image. However, the features in the low-frequency part are basically smoother, so the low-frequency feature map does not need the same spatial dimension as the high-frequency map to express the information of the image. In other words, when using traditional convolution, the high-frequency feature map

contains quite a bit more information than the low-frequency feature map under the same spatial perception field, which indicates that there is redundant information in the low-frequency feature map. Therefore, as shown in Figure 2, we design two non-deep parallel branches while using octave convolution instead of traditional 3D convolution, to compress the spatial dimension for low-frequency feature map to reduce network parameters.

(1) Octave-Convolution-Based Spectral Branch: As shown in Figure 2, for S_e with more spectral dimensions, we design a branch of 3D octave convolution, aiming to reduce the model complexity while concentrating on mining spectral features. The major steps are specified in following description.

Step 1: For $S_e \in \mathbb{R}^{A_1 \times A_1 \times R_1}$, we separate S_e into the high-frequency component $S_e^h \in \mathbb{R}^{A_1 \times A_1 \times R_1}$ and the low-frequency component $S_e^l \in \mathbb{R}^{a \times a \times R_1}$ by using two different scales of 3D convolution. The specific process can be calculated as follows:

$$S_e^h = f_{3D}(S_e * W_{h \Rightarrow h} + b_{h \Rightarrow h}) \tag{3}$$

$$S_e^l = f_{3D}(\text{Avgpool}(S_e, a) * W_{h \Rightarrow l} + b_{h \Rightarrow l}) \tag{4}$$

where f_{3D} represents the 3D convolution, $\text{Avgpool}(S_e, a)$ denotes the average pooling that reduces the spatial size to $a \times a$. $W_{h \Rightarrow h}$ and $W_{h \Rightarrow l}$ are two different scales of convolution kernels respectively. $b_{h \Rightarrow h}$ and $b_{h \Rightarrow l}$ are the bias of two different 3D convolutions, respectively.

Step 2: After obtaining the high-frequency components S_e^h, we continue the frequency decomposition of S_e^h by using 3D convolution and average pooling, to obtain further high-frequency components $f_e(h \Rightarrow h) \in \mathbb{R}^{A_1 \times A_1 \times R_1}$ and low-frequency components $f_e(h \Rightarrow l) \in \mathbb{R}^{a \times a \times R_1}$. The specific process can be formulated as:

$$f_e(h \Rightarrow h) = f_{3D}(S_e^h * W_{h \Rightarrow h} + b_{h \Rightarrow h}) \tag{5}$$

$$f_e(h \Rightarrow l) = f_{3D}(\text{Avgpool}(S_e^h, a) * W_{h \Rightarrow l} + b_{h \Rightarrow l}) \tag{6}$$

Similarly, after obtaining the low-frequency components S_e^l, we apply upsampling and 3D convolution to S_e^l, to obtain further high-frequency components $f_e(l \Rightarrow h) \in \mathbb{R}^{A_1 \times A_1 \times R_1}$ and low-frequency components $f_e(l \Rightarrow l) \in \mathbb{R}^{a \times a \times R_1}$, respectively. The specific process can be formulated as:

$$f_e(l \Rightarrow h) = \text{upsample}(f_{3D}(S_e^l * W_{l \Rightarrow h} + b_{l \Rightarrow h}), A_1) \tag{7}$$

$$f_e(l \Rightarrow h) = f_{3D}(S_e^l * W_{l \Rightarrow l} + b_{l \Rightarrow l}) \tag{8}$$
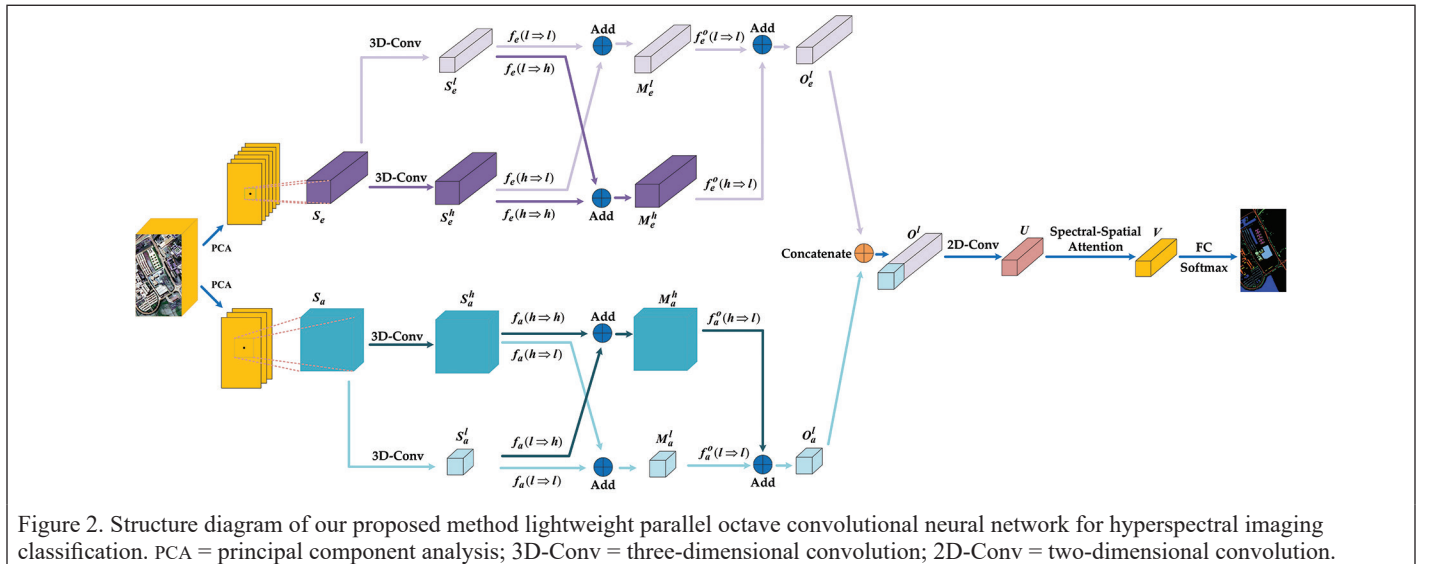

Figure 2. Structure diagram of our proposed method lightweight parallel octave convolutional neural network for hyperspectral imaging classification. PCA = principal component analysis; 3D-Conv = three-dimensional convolution; 2D-Conv = two-dimensional convolution.

where upsample($\cdot$, A_1) denotes the up-sampling operation using the nearest interpolation method to expand the spatial size to $A_1 \times A_1$. $W_{h \Rightarrow h}$ and $W_{h \Rightarrow l}$ are two different scales of convolution kernels, respectively, $b_{h \Rightarrow h}$ and $b_{h \Rightarrow l}$ are the corresponding bias, respectively.

Step 3: We take into account the need to update not only intra-frequency information but also inter-frequency information. Therefore, the two high-frequency components $f_e(h \Rightarrow h)$ and $f_e(l \Rightarrow l)$ are added to facilitate the fusion of high-frequency information between frequencies, obtaining the new high-frequency components $M_e^h \in \mathbb{R}^{A_1 \times A_1 \times R_1}$. And the two low-frequency components $f_e(h \Rightarrow l)$ and $f_e(l \Rightarrow l)$ are added to facilitate the fusion of low-frequency information between frequencies, obtaining the new low-frequency components $M_e^l \in \mathbb{R}^{a \times a \times R_1}$. The process can be expressed by the equation:

$$M_e^h = f_e(h \Rightarrow h) + f_e(l \Rightarrow h) \quad (9)$$

$$M_e^l = f_e(h \Rightarrow l) + f_e(l \Rightarrow l) \quad (10)$$

Next, we continue applying the average pooling and the 3D convolution to M_e^h, aiming to obtain $f_e^o(h \Rightarrow l) \in \mathbb{R}^{a \times a \times R_1}$ with the reduced spatial size. Meanwhile, we apply the 3D convolution to M_e^l and obtain $f_e^o(l \Rightarrow l) \in \mathbb{R}^{a \times a \times R_1}$. Finally, $f_e^o(h \Rightarrow l)$ and $f_e^o(l \Rightarrow l)$ are added to acquire final low-frequency feature maps $O_e^l \in \mathbb{R}^{a \times a \times R_1}$. The process can be expressed by the equation:

$$f_e^o(h \Rightarrow l) = f_{3D}(\text{Avgpool}(M_e^h, a) * W_{h \Rightarrow l} + b_{h \Rightarrow l}) \quad (11)$$

$$f_e^o(l \Rightarrow l) = f_{3D}(M_e^l * W_{l \Rightarrow l} + b_{l \Rightarrow l}) \quad (12)$$

$$O_e^l = f_e^o(h \Rightarrow l) + f_e^o(l \Rightarrow l) \quad (13)$$

(2) Octave-Convolution-Based Spatial Branch: For S_a with larger spatial window, we design a branch of 3D octave convolution, aiming to reduce the model complexity while concentrating on mining spatial features. As shown in Figure 2, the process of S_a is similar to that of S_e. Likewise, we also obtain the low-frequency feature map $O_a^l \in \mathbb{R}^{a \times a \times R_1}$.

Finally, O_e^l and O_a^l are concatenated to facilitate the integration of spectral and spatial features, obtaining the output $O_e^l \in \mathbb{R}^{a \times a \times (R_1 + R_1)}$ after connecting the two branches. Actually, the design of non-deep parallel network instead of deep network facilitates the light weighting of the model, which improves the generalization performance of the model to obtain better classification accuracy under small samples situations.

Spectral -Spatial Attention

After acquiring the output O^l, we use 2D convolution to fuse spectral-spatial features from different parallel layers. In the 2D convolution, it is noteworthy that we use the convolution kernel with size {1 × 1} instead of the commonly used convolution kernel with size {3 × 3}, which reduces the number of input channels with fewer parameters. Therefore, we obtain the output U after the 2D convolution. Moreover, we design the spectral-spatial attention after 2DCNN to promote the classification performance even further by adaptively adjusting corresponding weights of different spectral-spatial features according to their contribution to classification. The spectral-spatial attention mechanism is presented in Figure 3.
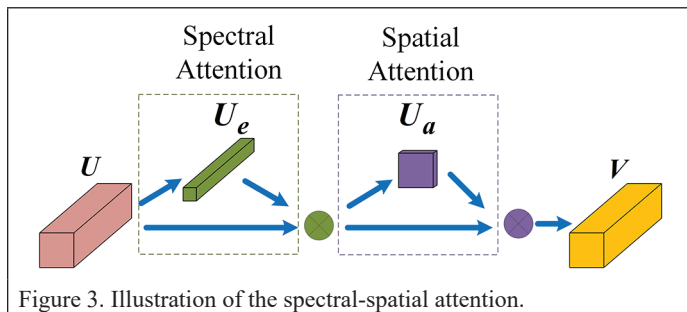
Figure 3. Illustration of the spectral-spatial attention.

As shown in Figure 3, after the spectral-spatial attention, we can obtain the output $V = U \otimes U_e \otimes U_a$. And the obtaining of U_e and U_a can be expressed by the equation:

$$U_e = \text{sigmoid}(f_{2D}(f_{2D}(U_e^{avg} * W_1 + b_1) * W_2 + b_2) + f_{2D}(f_{2D}(U_e^{max} * W_1 + b_1) * W_2 + b_2) \quad (14)$$

$$U_a = \text{sigmoid}(f_{2D}((U_e^{avg}, U_e^{max}) * W_3 + b_3) \quad (15)$$

where U_e^{max} and U_e^{avg} represent the feature maps gained by the global max pooling and the global average pooling over the spatial dimension respectively, squeezing the spatial dimension. U_a^{max} and U_a^{avg} represent the feature maps gained by the global max pooling and the global average pooling over the channel dimension respectively, squeezing the channel dimension. f_{2D} represents the 2D convolution, and W_1, W_2, W_3 indicate the convolution kernel. b_1, b_2, and b_3 represent the corresponding bias.

Finally, the discriminative spectral–spatial features V adjusted by the spectral-spatial attention enter the fully connected network to get the final classification results.

Experiments and Analysis

In this chapter, the classification performance of the suggested LPOCNN method is evaluated on three real HSI data sets. We first briefly introduce the three applied HSI data sets and then describe the accompanying experimental configurations. Next, we analyze the impact of the main parameters of the suggested LPOCNN method on classification performance. Finally, the superiority of the suggested LPOCNN method is verified by comparing it with various competitive classification methods.

Data Set Description

Indian Pines (IP), University of Pavia (UP), and Salinas (SA) are the HSI data sets adopted in our experiment. Figures 4, 5, and 6 show their false-color images and ground-truth images, respectively. Tables 1–3 list the ground-truth category of these three HSI data sets, and their brief descriptions are shown as follows.
(1) IP: The IP data set is captured by the AVIRIS sensor at the agricultural experimentation area in Indiana. This scene contains 16 representative ground truth classes. The spatial dimension of IP data set is 145 × 145, and it contains 224 bands in the spectral range from 400 to 2500 nm. In our experiments, 24 bands with noise are discarded.
(2) UP: The UP data set is captured by a spectrograph sensor in northern Italy. This scene contains nine representative ground truth classes. The spatial dimension of UP data set is 610 × 340, and it contains 115 bands in the spectral range from 4300 to 8600 nm. In our experiments, 12 bands with noise are discarded.
(3) SA: The SA data set is captured by a hyperspectral sensor in California. This scene contains 16 representative ground truth classes. The spatial dimension of SA data set is 512 × 217, and it contains 224 bands. In our experiments, 20 bands with noise are discarded.

Experimental Configuration

All our experiments are implemented on hardware devices with a Nvidia GeForce RTX2060 GPU and an AMD Ryzen 7 4800H CPU. Pytorch 1.2.0 and Windows 10 systems are used as the software environment for the experiments.

Specifically, in all our experiments, the training set for each HSI data set is created by randomly selecting only five labeled samples from each category, and the remaining samples are served as the testing set. Detailed divisions of the training and testing sets for each HSI data set are listed in Tables 1–3. In our experiments, we use the overall accuracy (OA), average accuracy (AA), Kappa coefficient (Kappa), and accuracy of per class to comprehensively evaluate the classification performance of each model.

Analysis of Parameters

In the suggested LPOCNN method, the three main parameters, learning rate, spectral dimension, and spatial size, have significant impacts on classification performance. We analyze the classification results when
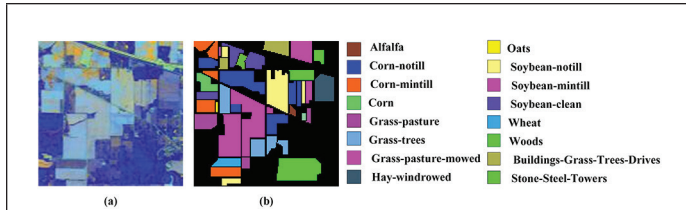
Figure 4. Indian Pines; (a) The false-color image; (b) The ground-truth image.
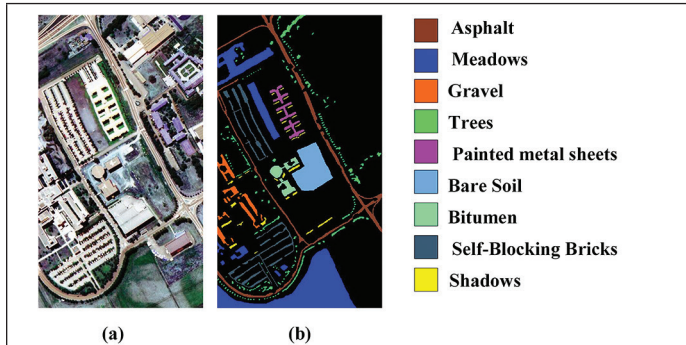
Figure 5. University of Pavia; (a) The false-color image; (b) The ground-truth image.
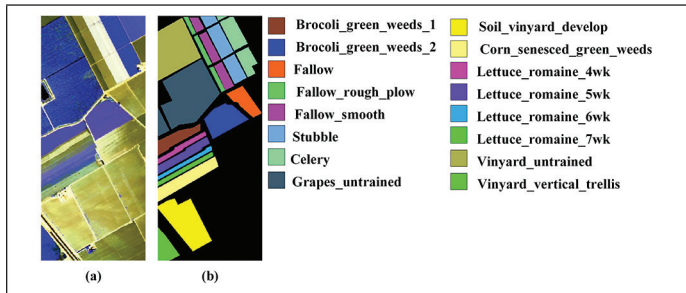
Figure 6. Salinas; (a) The false-color image; (b) The ground-truth image.

Table 1. Number of training and testing samples for Indian Pines (IP).

Class	Name	Train	Test	Total
1	Alfalfa	5	41	46
2	Corn-notill	5	1423	1428
3	Corn-mintill	5	825	830
4	Corn	5	232	237
5	Grass-pasture	5	478	483
6	Grass-trees	5	725	730
7	Grass-pasture-mowed	5	23	28
8	Hay-windrowed	5	473	478
9	Oats	5	15	20
10	Soybean-notill	5	967	972
11	Soybean-mintill	5	2450	2455
12	Soybean-clean	5	588	593
13	Wheat	5	200	205
14	Woods	5	1260	1265
15	Buildings-Grass-Trees-Drives	5	381	386
16	Stone-Steel-Towers	5	88	93
Total		80	10 169	10 249

Table 2. Number of training and testing samples for University of Pavia (UP).

Class	Name	Train	Test	Total
1	Asphalt	5	6626	6631
2	Meadows	5	18 644	18 649
3	Gravel	5	2094	2099
4	Trees	5	3059	3064
5	Painted metal sheets	5	1340	1345
6	Bare Soil	5	5024	5029
7	Bitumen	5	1325	1330
8	Self-Blocking Bricks	5	3677	3682
9	Shadows	5	942	947
Total		45	42 731	42 776

Table 3. Number of training and testing samples for Salinas (SA).

Class	Name	Train	Test	Total
1	Brocoli_green_weeds_1	5	2004	2009
2	Brocoli_green_weeds_2	5	3721	3726
3	Fallow	5	1971	1976
4	Fallow_rough_plow	5	1386	1394
5	Fallow_smooth	5	2673	2678
6	Stubble	5	3954	3959
7	Celery	5	3574	3579
8	Grapes_untrained	5	11 266	11 271
9	Soil_vinyard_develop	5	6198	6203
10	Corn_senesced_green_weeds	5	3273	3278
11	Lettuce_romaine_4wk	5	1063	1068
12	Lettuce_romaine_5wk	5	1922	1927
13	Lettuce_romaine_6wk	5	911	916
14	Lettuce_romaine_7wk	5	1065	1070
15	Vinyard_untrained	5	7263	7268
16	Vinyard_vertical_trellis	5	1802	1807
Total		80	54 049	54 129

these three main parameters vary, to demonstrate their respective effects on the final accuracy.

(1) Learning rate: Since the learning rate controls the convergence speed and convergence ability during the model training, we evaluate the impacts of the learning rate on classification performance in the suggested LPOCNN method. In the following experiments, we consider the set of learning rates {0.00005, 0.0001, 0.0003, 0.0005, 0.001, 0.003, 0.005, 0.01}, to observe the influence of learning rates on classification performance for all the three HSI data sets. The experimental results are presented in Figure 7.

From Figure 7, we can observe that the OA increases gradually with the learning rate ranging from 0.00005 to 0.001 for all the three HSI data sets. However, as the learning rate continues to increase from 0.001 to 0.01, the classification accuracy for these three data sets decreases rapidly. The main reason is that if the learning rate is too small, the loss function changes very slowly, which can greatly increase the convergence complexity of the network and can easily get trapped in local minima. However, if the learning rate is too large, it may cause the model to cross the global optimum directly or even not converge. Based on the above experimental results, the learning rate is fixed to 0.001 for all the three HSI data sets to obtain the optimal classification performance.

(2) Spectral dimension: Since S_e contains more spectral information and less spatial information, we evaluate the effect of spectral dimension of S_e on the classification performance in our proposed method. In our experiments, we consider the set of spectral dimension {80, 90, 100, 110, 120, 130, 140} for IP and SA, and {5, 10, 15, 20, 25, 30, 35} for UP, to observe the influence of spectral dimension on classification performance. The experimental results are presented in Figure 8.

As can be seen from Figure 8, OA gradually increases with the spectral dimension ranging from 80 to 110 for IP and SA, and from 5 to 20 for UP. However, the classification accuracy of these three data sets gradually decreases as the spectral dimension grows further. The main reason is that initially, as the spectral dimension increases, more and more spectral information available for classification is retained. However, if the spectral dimension grows further, some

Figure 7. Effects analysis of the learning rate in our proposed method.

Figure 8. Effects analysis of the spectral dimension in our proposed method.

Figure 9. Effects analysis of the spatial size in our proposed method.

noisy information will also be retained, thus reducing the classification accuracy. Moreover, a larger spectral dimension will further increase the computational complexity of the model. Based on the above experimental results, the spectral dimension of S_e is fixed to 110 for IP and SA, 20 for UP to obtain the optimal classification performance. Specially, since S_a contains less spectral information, the spectral dimension of S_a is preset to 11 for all the three HSI data sets, ensuring the basic spectral information and reducing computation complexities.

(3) Spatial size: Since S_a contains more spatial information and less spectral information, we evaluate the impact of the spatial size of S_a on the classification performance in the suggested LPOCNN method. In the following experiments, we consider the set of spatial size $\{19 \times 19, 21 \times 21, 23 \times 23, 25 \times 25, 27 \times 27, 29 \times 29, 31 \times 31\}$ to observe the influence of spatial size on classification performance for all the three HSI data sets. The experimental results are presented in Figure 9.

From Figure 9, we can observe that OA gradually increases with the spatial size ranging from 19 to 25 for all the three HSI data sets. However, as the spatial size continues to increase from 25 to 31, the classification accuracy for these three data sets gradually decreases. The main reason for this is that at first, as the spatial size increases, the spatial structure information available for classification becomes more and more adequate. However, if the spatial size is too large, pixels that are not in the same class as the central pixel will also be included more often, which reduces the classification accuracy. Based on the above experimental results, the spatial size of S_a is fixed to 25×25 for all the three HSI data sets to obtain the optimal classification performance. Specially, since S_e contains less spatial information, the spatial size of is preset to 11×11 for all three HSI data sets, reducing computation complexities and guaranteeing the basic spatial structure information.

Comparisons to the State-of-the-Art Methods

In this section, we provide a comparison of our proposed LPOCNN method with six advanced methods: a traditional method SVM, and five deep learning-based methods, SSRN, hybrid spectral CNN (HybridSN) (Roy *et al.* 2020), residual spectral-spatial attention network (RSSAN), dual-channel capsule generation adversarial network (DcCapsGAN) (Jianing *et al.* 2022), and cross-scale graph prototypical network (X-GPN) (Xi *et al.* 2022). SVM is a traditional method for HSI classification using only spectral features. SSRN introduces 3D convolution to concurrently mine spectral-spatial features for 3D HSI. HybridSN is a hybrid convolutional network using 3D-2DCNN to extract joint spectral-spatial features. RSSAN uses the attention mechanisms to emphasize features that contribute more to the classification. We also compare it with the latest deep learning-based method X-GPN, which introduces graph convolutional networks to address the problems of model overfitting and performance degradation. Specially, to validate the advantages of the suggested LPOCNN method under small sample situation, we also compare it with DcCapsGAN, which enhances the classification performance under small samples situations by combining CapsNet with generative adversarial network. The parameters in SVM, SSRN, HybridSN, RSSAN, DcCapsGAN, and X-GPN for these comparisons above are set to their optimal values.

In this section, the division of training and testing samples is controlled to be consistent for all the above classification methods, as shown in Tables 1–3. In addition, for all the three HSI data sets, the quantitative average classification results of all compared methods are presented in Tables 4–6, and the corresponding classification maps of each classification method are depicted in Figures 10–12, respectively.

As can be seen from Tables 4–6, the suggested LPOCNN method achieves the best classification results compared to the other competing models. In addition, our proposed method still achieves 76.64% OA for IP, 81.59% OA for UP, and 91.71% OA for SA, with only five training samples per class, which validates the superiority of our proposed method. Although the latest deep learning-based method X-GPN introduces graph convolutional networks to address the problem of model overfitting and performance degradation under small samples situations, and the DcCapsGAN method also aims to improve the HSI classification accuracy under small samples situations, the suggested
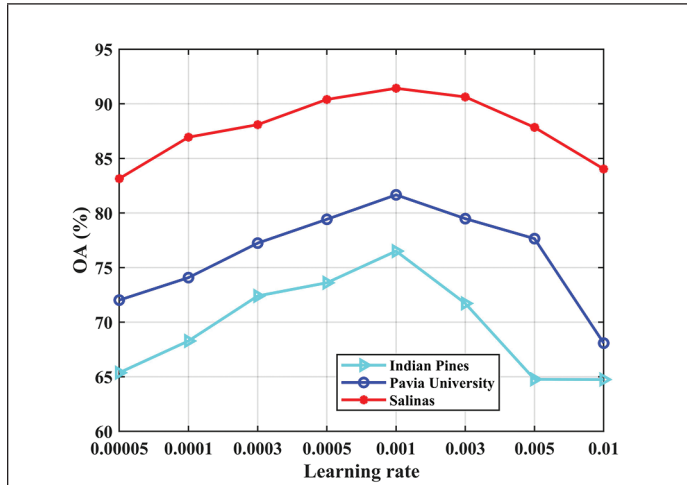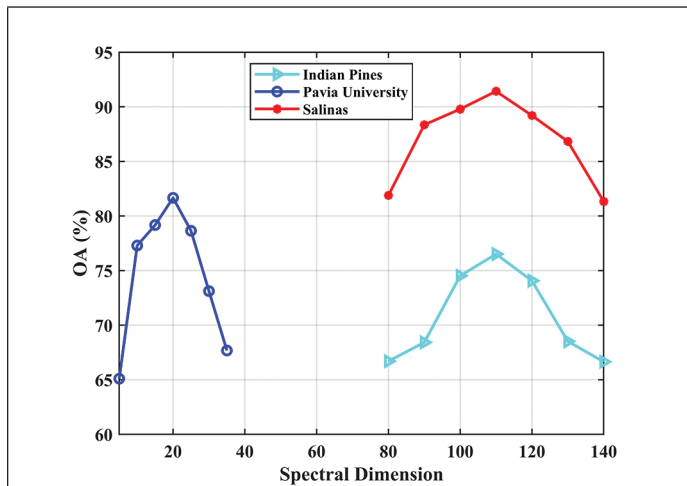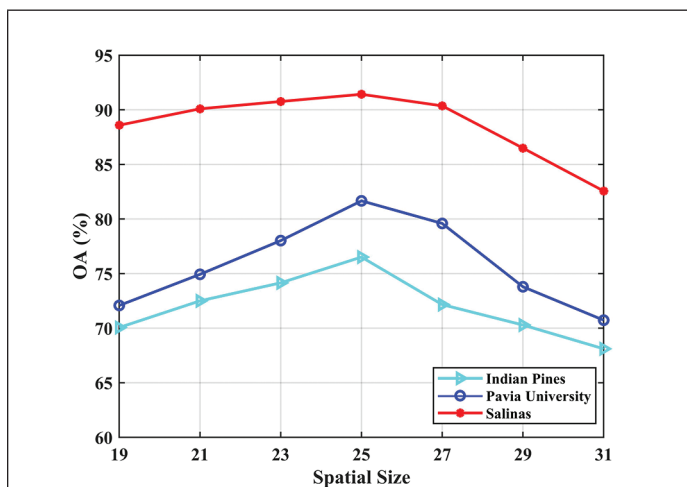
LPOCNN method still shows superior classification accuracy than them. The main reason is that our method constructs two 3D patch cubes with different spatial and spectral scales for each central pixel, removing redundancy and focusing on extracting spatial features and spectral features, respectively. Under small samples situations, extracting more adequate spectral-spatial information is very effective in improving the classification accuracy. In addition, to alleviate the requirement for the number of labeled samples, our method design two non-deep parallel branches, while using octave convolution instead of traditional 3D convolution in a two-branch structure to reduce the network parameters. This design of parallel shallow network instead of deep network in our method facilitates the light weighting of the model, which improves the generalization performance of the model to obtain better classification accuracy under small sample situations. Meanwhile, in the feature fusion stage, we design the spectral-spatial attention to promote the classification performance even further, by adaptively adjusting the weights of different spectral-spatial features according to their contribution to classification. As can be seen in Figures 10–12, the suggested

LPOCNN method achieves more accurate classification maps compared to other competing models, which also shows its superior classification performance. In addition, the computational efficiency of all the above methods is tested for the three HSI data sets. It can be seen from Tables 4–6 that the computation time of our suggested LPOCNN method is much less than that of other deep learning-based methods for all the three data sets. The main reason is that these deep learning-based methods require training numerous parameters because of complex networks, resulting in more computational time consumption. But in our proposed LPOCNN method, two non-deep parallel branches are created for the two inputs, which design octave convolution rather than classical 3D convolution to facilitate light weighting of the model. Therefore, taking into account the classification performance and computation time, our method shows a clear superiority over various competitive classification methods.

Ablation Study
In this subsection, we compare the LPOCNN method with three other classification methods for the ablation analysis of our proposed
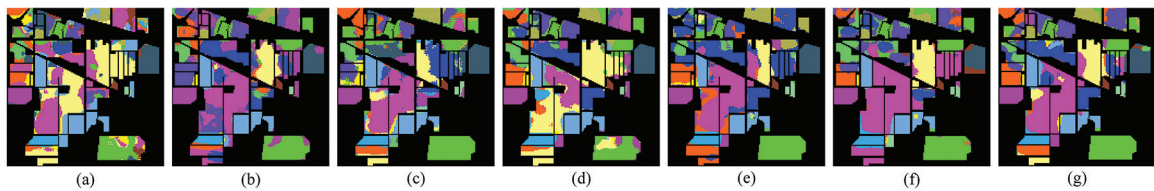
Figure 10. Classification maps obtained by each method for Indian Pines (IP): (a) SVM, (b) SSRN, (c) HybridSN, (d) RSSAN, (e) DcCapsGAN, (f) X-GPN, (g) Proposed Method. SVM = support vector machines; SSRN = spectral–spatial residual network; HybridSN = hybrid spectral convolutional neural network; RSSAN = residual spectral-spatial attention network; DcCapsGAN = dual-channel capsule generation adversarial network; X-GPN = cross-scale graph prototypical network.
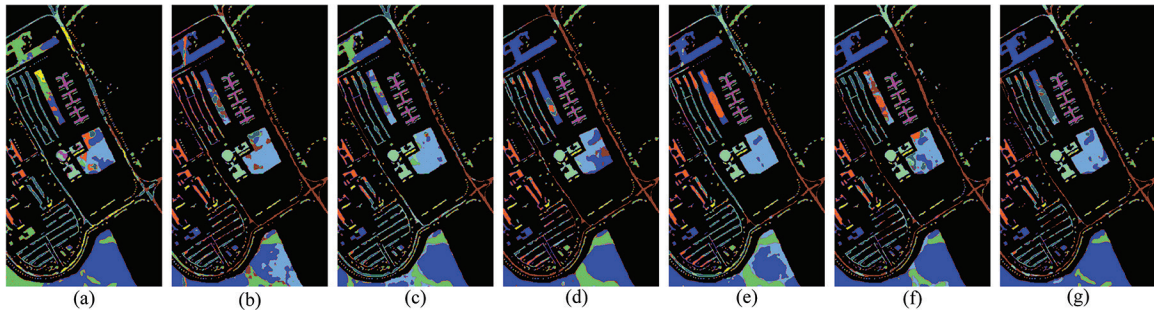
Figure 11. Classification maps obtained by each method for University of Pavia (UP): (a) SVM, (b) SSRN, (c) HybridSN, (d) RSSAN, (e) DcCapsGAN, (f) X-GPN, (g) Proposed Method. SVM = support vector machines; SSRN = spectral–spatial residual network; HybridSN = hybrid spectral convolutional neural network; RSSAN = residual spectral-spatial attention network; DcCapsGAN = dual-channel capsule generation adversarial network; X-GPN = cross-scale graph prototypical network.

Figure 12. Classification maps obtained by each method for Salinas (SA): (a) SVM, (b) SSRN, (c) HybridSN, (d) RSSAN, (e) DcCapsGAN, (f) X-GPN, (g) Proposed Method. SVM = support vector machines; SSRN = spectral–spatial residual network; HybridSN = hybrid spectral convolutional neural network; RSSAN = residual spectral-spatial attention network; DcCapsGAN = dual-channel capsule generation adversarial network; X-GPN = cross-scale graph prototypical network.

Table 4. Classification results obtained by each method for Indian Pines (IP). The results shown in bold format represent the optimal value in each row.

Class	SVM	SSRN	HybridSN	RSSAN	DcCapsGAN	X-GPN	Our
1	83.21 ± 9.23	94.33 ± 3.95	92.11 ± 2.43	46.12 ± 18.54	**100.00** ± 0.00	98.39 ± 2.08	97.78 ± 2.99
2	27.86 ± 7.34	51.59 ± 10.21	35.85 ± 10.26	63.88 ± 9.82	49.98 ± 0.28	52.48 ± 15.46	**66.55** ± 11.13
3	37.43 ± 11.26	51.65 ± 7.05	31.93 ± 17.06	64.05 ± 12.17	44.66 ± 0.14	57.07 ± 17.89	**70.76** ± 11.42
4	59.28 ± 12.43	88.98 ± 9.50	85.59 ± 9.15	44.23 ± 11.61	47.01 ± 0.52	88.92 ± 12.60	**89.78** ± 11.46
5	68.02 ± 8.41	64.26 ± 10.46	**86.74** ± 9.19	78.67 ± 9.89	64.98 ± 0.23	81.70 ± 7.48	80.53 ± 8.26
6	72.50 ± 13.47	62.88 ± 14.11	93.61 ± 5.61	91.02 ± 6.31	84.02 ± 0.11	**95.89** ± 3.11	93.88 ± 5.36
7	90.24 ± 6.68	98.87 ± 2.12	**100.00** ± 0.00	32.11 ± 15.40	**100.00** ± 0.00	98.52 ± 4.67	**100.00** ± 0.00
8	67.68 ± 14.91	96.61 ± 4.27	**99.86** ± 0.08	97.64 ± 4.11	79.95 ± 0.19	90.11 ± 11.58	96.37 ± 7.58
9	91.45 ± 12.84	95.71 ± 6.26	99.92 ± 0.12	25.78 ± 16.39	**100.00** ± 0.00	99.15 ± 2.29	**100.00** ± 0.00
10	54.02 ± 12.55	58.07 ± 5.25	61.1 ± 11.97	58.21 ± 8.71	62.45 ± 0.35	63.64 ± 12.74	**75.98** ± 6.29
11	35.98 ± 9.74	53.11 ± 11.38	53.98 ± 16.54	**68.98** ± 7.76	64.83 ± 0.21	50.26 ± 14.65	65.19 ± 10.83
12	34.62 ± 9.02	70.10 ± 8.27	**82.74** ± 2.74	52.04 ± 15.39	49.54 ± 0.41	66.01 ± 15.92	67.81 ± 12.53
13	87.78 ± 5.32	94.99 ± 7.12	98.63 ± 1.03	88.33 ± 14.33	98.99 ± 0.06	96.88 ± 7.17	**99.23** ± 1.50
14	61.39 ± 7.89	71.38 ± 12.39	73.83 ± 7.42	**95.37** ± 4.62	94.75 ± 0.26	74.15 ± 16.82	89.59 ± 6.36
15	29.1 ± 6.14	74.22 ± 8.11	69.84 ± 13.95	65.26 ± 13.85	36.89 ± 0.82	**85.07** ± 11.28	83.69 ± 11.87
16	89.44 ± 5.07	98.64 ± 1.89	97.98 ± 3.27	71.17 ± 16.01	**98.76** ± 0.36	98.69 ± 3.42	98.31 ± 3.19
OA	48.23 ± 5.85	63.54 ± 4.94	63.68 ± 5.06	66.95 ± 4.79	66.71 ± 0.08	67.16 ± 4.17	**76.64** ± 3.31
AA	61.88 ± 4.03	76.59 ± 3.82	79.01 ± 3.49	65.18 ± 3.31	73.55 ± 0.11	81.06 ± 1.41	**85.89** ± 1.79
Kappa	42.76 ± 5.91	59.07 ± 5.37	59.33 ± 6.13	63.47 ± 5.24	62.18 ± 0.05	62.93 ± 4.46	**73.78** ± 3.60
Computational time (s)	8.47	534.56	51.34	824.69	2431.68	1291.77	33.74

SVM = support vector machines; SSRN = spectral–spatial residual network; HybridSN = hybrid spectral convolutional neural network; RSSAN = residual spectral-spatial attention network; DcCapsGAN = dual-channel capsule generation adversarial network; X-GPN = cross-scale graph prototypical network.

Table 5. Classification results obtained by each method for University of Pavia (UP). The results shown in bold format represent the optimal value in each row.

Class	SVM	SSRN	HybridSN	RSSAN	DcCapsGAN	X-GPN	Our
1	50.02 ± 12.74	54.95 ± 10.64	57.90 ± 7.41	75.46 ± 10.37	36.58 ± 5.33	61.38 ± 13.95	**78.13** ± 12.34
2	44.37 ± 13.05	57.04 ± 12.09	63.39 ± 9.11	77.35 ± 12.05	75.02 ± 0.68	70.10 ± 12.70	**83.24** ± 10.10
3	61.89 ± 15.65	71.68 ± 9.47	61.65 ± 8.60	69.04 ± 14.26	78.09 ± 1.49	75.59 ± 10.41	**86.81** ± 7.16
4	87.12 ± 10.18	93.54 ± 5.82	81.71 ± 5.59	95.97 ± 4.47	**98.30** ± 0.09	81.88 ± 5.26	84.23 ± 10.19
5	96.31 ± 7.07	99.49 ± 0.78	99.82 ± 0.09	99.85 ± 0.95	**100.00** ± 0.00	99.87 ± 0.19	99.94 ± 0.17
6	53.07 ± 12.85	72.21 ± 14.09	80.94 ± 5.66	79.13 ± 14.83	53.98 ± 0.41	74.13 ± 15.88	**81.44** ± 11.38
7	73.26 ± 19.11	94.36 ± 2.71	**99.09** ± 1.92	92.45 ± 8.20	97.96 ± 0.57	96.47 ± 3.93	94.37 ± 5.80
8	49.17 ± 13.97	72.53 ± 11.87	74.80 ± 6.36	**79.76** ± 16.61	70.01 ± 3.13	71.55 ± 16.22	61.75 ± 12.63
9	94.11 ± 6.86	86.80 ± 6.58	92.55 ± 4.27	86.90 ± 4.79	**100.00** ± 0.00	81.72 ± 11.82	87.94 ± 10.97
OA	54.16 ± 6.41	67.08 ± 5.81	70.17 ± 6.15	79.94 ± 6.03	70.09 ± 1.12	72.50 ± 5.26	**81.59** ± 3.49
AA	67.71 ± 4.06	78.07 ± 4.01	79.55 ± 3.74	83.98 ± 3.68	78.88 ± 0.71	79.18 ± 2.71	**84.20** ± 2.19
Kappa	45.05 ± 6.14	59.47 ± 5.93	62.89 ± 6.76	73.78 ± 6.59	63.15 ± 1.14	65.61 ± 5.83	**76.37** ± 4.02
Computational time (s)	38.11	221.77	42.62	659.75	1088.61	775.06	34.43

SVM = support vector machines; SSRN = spectral–spatial residual network; HybridSN = hybrid spectral convolutional neural network; RSSAN = residual spectral-spatial attention network; DcCapsGAN = dual-channel capsule generation adversarial network; X-GPN = cross-scale graph prototypical network.
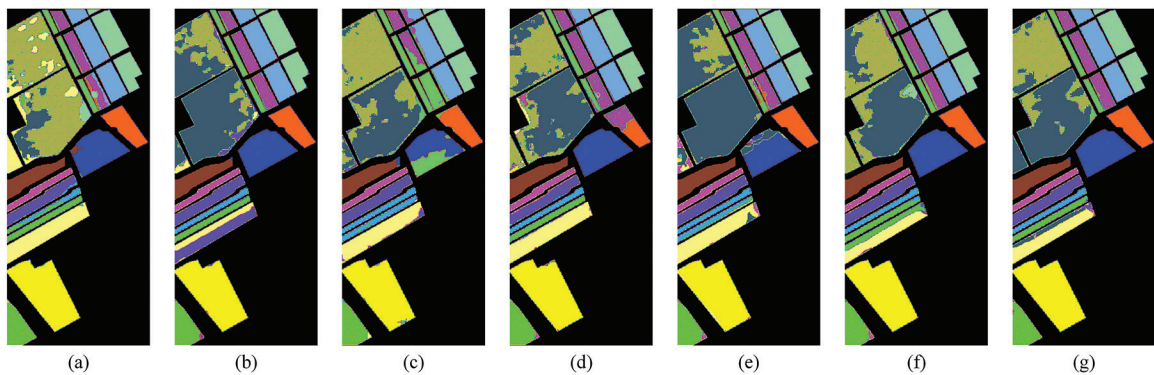
Table 6. Classification results obtained by each method for Salinas (SA). The results shown in bold format represent the optimal value in each row.

Class	SVM	SSRN	HybridSN	RSSAN	DcCapsGAN	X-GPN	Our
1	96.95 ± 1.58	98.69 ± 1.22	97.15 ± 2.43	98.21 ± 3.59	96.98 ± 2.16	98.79 ± 3.04	**98.87** ± 2.21
2	96.06 ± 2.50	93.62 ± 6.38	99.89 ± 0.28	99.32 ± 1.21	**99.94** ± 0.11	98.30 ± 3.21	98.95 ± 2.06
3	70.12 ± 15.47	71.19 ± 15.51	99.07 ± 3.11	95.94 ± 1.86	**100.00** ± 0.00	95.11 ± 13.83	99.15 ± 2.52
4	98.52 ± 3.24	98.86 ± 0.24	99.23 ± 1.26	96.02 ± 3.62	**99.79** ± 0.06	99.20 ± 0.85	97.95 ± 2.65
5	94.41 ± 6.77	96.52 ± 1.96	88.74 ± 5.85	**96.96** ± 2.17	96.42 ± 0.22	91.72 ± 8.19	94.89 ± 3.67
6	98.98 ± 0.41	99.23 ± 0.28	80.22 ± 4.97	99.63 ± 0.52	**100.00** ± 0.00	98.26 ± 3.05	99.07 ± 1.98
7	98.47 ± 2.05	97.43 ± 3.60	99.57 ± 1.04	98.81 ± 1.24	**99.75** ± 0.18	96.20 ± 9.81	98.97 ± 0.99
8	59.64 ± 16.67	61.49 ± 14.62	69.91 ± 12.96	82.05 ± 4.88	62.77 ± 0.48	67.38 ± 14.88	**83.97** ± 11.00
9	96.31 ± 0.88	96.02 ± 2.66	99.45 ± 0.81	99.27 ± 0.72	**99.88** ± 0.05	99.51 ± 1.27	99.65 ± 0.73
10	77.04 ± 5.19	82.95 ± 4.78	44.25 ± 18.71	**89.95** ± 4.03	79.65 ± 0.23	79.89 ± 14.92	88.45 ± 10.89
11	94.25 ± 2.87	92.31 ± 7.10	99.64 ± 1.12	93.10 ± 3.11	98.10 ± 0.17	**99.93** ± 0.08	99.70 ± 0.70
12	82.69 ± 21.23	92.88 ± 7.53	63.72 ± 18.24	97.72 ± 4.27	**99.86** ± 0.06	90.62 ± 6.38	94.75 ± 6.98
13	97.56 ± 0.84	98.06 ± 1.14	48.68 ± 22.16	93.04 ± 6.59	**99.62** ± 0.04	93.45 ± 12.47	98.08 ± 3.18
14	90.11 ± 6.29	92.47 ± 2.66	89.10 ± 6.68	92.44 ± 9.68	**99.51** ± 0.09	93.19 ± 6.85	92.50 ± 6.64
15	59.97 ± 14.30	65.62 ± 10.24	66.63 ± 13.23	65.51 ± 10.22	40.09 ± 1.72	70.95 ± 15.74	**76.88** ± 11.92
16	84.83 ± 6.69	82.78 ± 6.56	92.34 ± 4.33	**99.47** ± 1.10	97.64 ± 0.10	94.65 ± 6.17	96.25 ± 4.93
OA	80.62 ± 2.18	83.06 ± 2.32	81.12 ± 3.52	86.45 ± 2.27	82.15 ± 0.20	86.27 ± 2.24	**91.71** ± 1.42
AA	87.23 ± 1.95	88.76 ± 1.60	83.78 ± 1.95	93.59 ± 1.22	91.87 ± 0.17	90.71 ± 0.91	**94.88** ± 0.96
Kappa	79.69 ± 2.40	82.11 ± 2.38	78.95 ± 3.71	85.86 ± 2.63	81.06 ± 0.21	84.71 ± 2.43	**90.78** ± 1.57
Computational time (s)	50.14	547.84	84.55	957.68	2598.43	1378.59	72.90

SVM = support vector machines; SSRN = spectral–spatial residual network; HybridSN = hybrid spectral convolutional neural network; RSSAN = residual spectral-spatial attention network; DcCapsGAN = dual-channel capsule generation adversarial network; X-GPN = cross-scale graph prototypical network.

Table 7. Results of the ablation analysis for Indian Pines (IP) data set.

Class	A	A+ SS-Attention	A+ Octave	LPOCNN
1	99.05 ± 1.28	96.95 ± 2.54	97.22 ± 1.85	97.78 ± 2.99
2	35.88 ± 17.11	50.56 ± 15.27	65.94 ± 9.48	66.55 ± 11.13
3	47.34 ± 13.29	68.90 ± 11.84	50.24 ± 15.27	70.76 ± 11.42
4	41.63 ± 9.64	97.36 ± 9.81	97.80 ± 13.24	89.78 ± 11.46
5	83.09 ± 7.17	67.02 ± 10.97	70.82 ± 6.51	80.53 ± 8.26
6	99.04 ± 10.08	91.67 ± 7.21	95.69 ± 9.48	93.88 ± 5.36
7	83.33 ± 8.52	99.95 ± 0.45	100 ± 0.00	100 ± 0.00
8	70.89 ± 12.26	60.68 ± 10.34	96.21 ± 7.46	96.37 ± 7.58
9	100 ± 0.00	90.02 ± 14.84	100 ± 0.00	100 ± 0.00
10	74.90 ± 5.31	61.95 ± 12.19	57.48 ± 10.08	75.98 ± 6.29
11	28.31 ± 18.84	48.34 ± 20.07	60.16 ± 16.41	65.19 ± 10.83
12	43.46 ± 10.16	56.78 ± 12.69	89.71 ± 15.42	67.81 ± 12.53
13	98.87 ± 0.98	99.18 ± 1.45	99.06 ± 2.35	99.23 ± 1.5
14	70.34 ± 8.43	77.77 ± 14.87	93.94 ± 7.14	89.59 ± 6.36
15	76.96 ± 15.29	97.87 ± 5.03	90.16 ± 11.47	83.69 ± 11.87
16	97.26 ± 8.24	98.12 ± 4.16	96.39 ± 6.35	98.31 ± 3.19
OA	55.72 ± 5.91	64.99 ± 5.77	73.98 ± 4.01	76.64 ± 3.31
AA	71.89 ± 5.04	78.95 ± 4.81	85.05 ± 1.85	85.89 ± 1.79
Kappa	51.49 ± 6.16	61.20 ± 5.89	70.69 ± 4.76	73.78 ± 3.60

LPOCNN = lightweight parallel octave convolutional neural network; OA = overall accuracy; AA = average accuracy; Kappa = Kappa coefficient.

Table 8. Results of the ablation analysis for University of Pavia (UP) data set.

Class	A	A+ SS-Attention	A+ Octave	LPOCNN
1	44.57 ± 12.47	76.02 ± 9.85	21.92 ± 16.31	78.13 ± 12.34
2	47.89 ± 9.19	74.10 ± 12.91	86.60 ± 8.64	83.24 ± 10.10
3	75.35 ± 5.82	97.13 ± 2.08	91.96 ± 5.47	86.81 ± 7.16
4	82.50 ± 9.08	94.50 ± 1.56	79.31 ± 13.36	84.23 ± 10.19
5	99.58 ± 0.25	99.92 ± 0.24	99.87 ± 0.10	99.94 ± 0.17
6	97.21 ± 11.36	44.81 ± 16.27	81.25 ± 10.56	81.44 ± 11.38
7	99.77 ± 4.71	99.45 ± 1.14	97.80 ± 4.42	94.37 ± 5.80
8	84.44 ± 5.81	16.94 ± 15.21	73.34 ± 6.13	61.75 ± 12.63
9	74.07 ± 16.95	85.06 ± 8.96	89.86 ± 14.62	87.94 ± 10.97
OA	63.96 ± 5.12	70.43 ± 4.81	75.40 ± 4.06	81.59 ± 3.49
AA	78.37 ± 4.37	76.42 ± 3.66	80.21 ± 3.17	84.20 ± 2.19
Kappa	56.97 ± 5.34	61.99 ± 4.98	68.62 ± 4.54	76.37 ± 4.02

LPOCNN = lightweight parallel octave convolutional neural network; OA = overall accuracy; AA = average accuracy; Kappa = Kappa coefficient.

Table 9. Results of the ablation analysis for Salinas (SA) data set.

Class	A	A+ SS-Attention	A+ Octave	LPOCNN
1	93.07 ± 5.02	98.14 ± 2.96	98.69 ± 3.16	98.87 ± 2.21
2	99.92 ± 1.83	99.97 ± 1.20	98.76 ± 2.52	98.95 ± 2.06
3	99.78 ± 1.95	99.02 ± 0.96	99.91 ± 1.97	99.15 ± 2.52
4	97.84 ± 4.26	97.99 ± 5.21	99.64 ± 1.24	97.95 ± 2.65
5	92.67 ± 6.08	95.70 ± 3.09	87.87 ± 4.08	94.89 ± 3.67
6	79.82 ± 7.37	99.95 ± 1.64	98.95 ± 3.71	99.07 ± 1.98
7	77.68 ± 6.82	99.83 ± 0.47	99.97 ± 0.82	98.97 ± 0.99
8	81.44 ± 3.17	60.15 ± 12.98	66.46 ± 16.27	83.97 ± 11.00
9	99.53 ± 0.65	99.26 ± 1.28	99.11 ± 1.19	99.65 ± 0.73
10	66.74 ± 14.18	73.85 ± 12.24	87.65 ± 8.83	88.45 ± 10.89
11	99.67 ± 0.55	99.47 ± 0.62	99.23 ± 0.44	99.70 ± 0.70
12	86.22 ± 4.98	65.31 ± 8.33	95.99 ± 4.38	94.75 ± 6.98
13	98.68 ± 1.83	98.98 ± 2.36	99.04 ± 1.08	98.08 ± 3.18
14	57.13 ± 11.69	59.19 ± 9.94	79.70 ± 15.91	92.50 ± 6.64
15	58.67 ± 8.26	89.77 ± 6.76	90.97 ± 7.72	76.88 ± 11.92
16	95.17 ± 3.82	85.97 ± 7.24	87.78 ± 8.68	96.25 ± 4.93
OA	83.36 ± 3.43	85.87 ± 2.06	89.37 ± 1.75	91.71 ± 1.42
AA	86.50 ± 1.72	88.91 ± 1.35	93.11 ± 1.19	94.88 ± 0.96
Kappa	81.38 ± 3.64	84.38 ± 2.27	88.21 ± 1.92	90.78 ± 1.57

LPOCNN = lightweight parallel octave convolutional neural network; OA = overall accuracy; AA = average accuracy; Kappa = Kappa coefficient.

method. Among these three compared methods, the first one is method (A), which removes both the octave convolution module and the spectral-spatial attention module in LPOCNN method, and the second one is method (A+ SS-Attention), which adds the spectral-spatial attention module to method A, and the third one is method (A+ Octave), which adds the octave convolution module to method A. As can be seen in Tables 7–9, firstly, method (A+ SS-Attention) shows a promising improvement on classification accuracy relative to method A for all the three HSI data sets. This proves that the spectral-spatial attention can promote the classification performance by adaptively adjusting corresponding weights of different spectral-spatial features according to their contribution to classification. In addition, the classification accuracy of method (A+ Octave) for all the three HSI data sets is much higher than that of method A. This proves that the utilization of octave convolution facilitates the light weighting of the model and can obtain better classification accuracy under small samples situations. Moreover, our proposed LPOCNN method takes full advantage of the octave convolution module and the spectral-spatial attention module and achieves the highest classification accuracy. The above ablation study quite comprehensively verifies that different modules of our proposed LPOCNN method are effective in improving the classification performance.

Analysis of the Number of Training Samples

Finally, to further validate the superiority of our proposed method under small sample situation, we test the impacts of the number of training samples on the classification performance. For all the three HSI data sets, we set the number of training samples for each class to 3, 7, and 9, respectively.

As can be observed from Figure 13, the suggested LPOCNN method still achieves the best classification accuracy with these three sampling strategies. Specially, the superiority of our proposed method over other competing methods is greater when the number of training samples is smaller. Thus, our suggested LPOCNN method is very advantageous over other competitive classification methods under small sample situations.

Conclusions

This paper proposes a novel lightweight parallel octave convolutional neural network (LPOCNN) for HSI classification. The HSI data is first preprocessed to construct two different inputs for each central pixel, focusing on extracting spatial features and spectral features respectively. Next, two non-deep parallel branches with octave convolution are created for the two inputs to facilitate light weighting of the model. Moreover, the spectral-spatial attention is designed to promote the classification performance even further, by adaptively adjusting the weights of different spectral-spatial features according to their
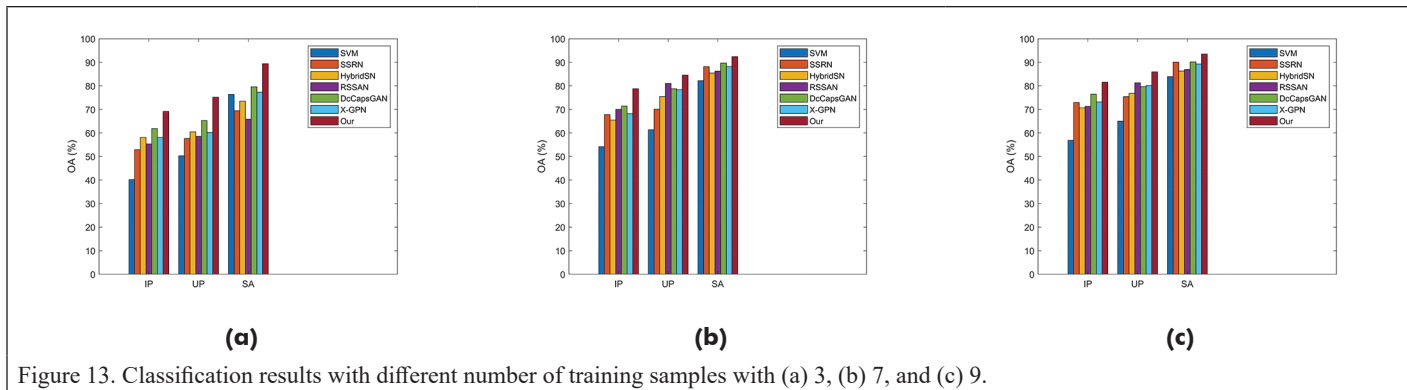
Figure 13. Classification results with different number of training samples with (a) 3, (b) 7, and (c) 9.

contribution to classification. Eventually, fused and adjusted discriminative features enter fully connected networks to finish the classification work. Experiments are conducted on three publicly available hyperspectral data sets and the results show that our suggested LPOCNN acquires a significant advantage on classification performance over other competitive methods under small sample situations. In our future work, we would like to design novel lightweight models that promote the classification performance even further under small samples situations.

References

Audebert, N., B. Le Saux and S. Lefevre. 2019. Deep learning for classification of hyperspectral data. *IEEE Geoscience and Remote Sensing Magazine* 7(2):159–173.

Ben Hamida, A., A. Benoit, P. Lambert and C. Ben Amar. 2018. 3-d deep learning approach for remote sensing image classification. *IEEE Transactions on Geoscience and Remote Sensing* 56(8):4420–4434.

Bhatti, U. A., Z. Y. Yu, J. Chanussot, Z. Zeeshan, L. W. Yuan, W. Luo, S. A. Nawaz, M. A. Bhatti, Q. ul Ain and A. Mehmood. 2022. Local similarity-based spatial-spectral fusion hyperspectral image classification with deep CNN and Gabor filtering. *IEEE Transactions on Geoscience and Remote Sensing* 60.

Bitar, A. W., L. F. Cheong and J. P. Ovarlez. 2019. Sparse and low-rank matrix decomposition for automatic target detection in hyperspectral imagery. *IEEE Transactions on Geoscience and Remote Sensing* 57(8):5239–5251.

Camps-Valls, G., L. Gomez-Chova, J. Munoz-Mari, J. Vila-Frances and J. Calpe-Maravilla. 2006. Composite kernels for hyperspectral image classification. *IEEE Geoscience and Remote Sensing Letters* 3(1):93–97.

Cao, C. H., L. Deng, W. Duan, F. Xiao, W. C. Yang and K. Hu. 2019. Hyperspectral image classification via compact-dictionary-based sparse representation. *Multimedia Tools and Applications* 78(11):15011–15031.

Chen, L., Y. Zhang and L. Wang. 2021. Hyperspectral image classification based on SOP-SRL band selection and 3d Gabor filtering. *Journal of Harbin Engineering University* 42(8):1230–1236.

Chen, L. C., Y. Yang, J. Wang, W. Xu and A. L. Yuille. 2016. Attention to scale: Scale-aware semantic image segmentation. Pages 3640–3649 in *Proceedings 2016 IEEE Conference on Computer Vision and Pattern Recognition (CVPR)*, held in Las Vegas, Nev., 27–30 June 2016.

Chen, S. J., Y. H. Hu, S. L. Xu, L. Li and Y. Z. Cheng. 2014. Classification of hyperspectral remote sensing imagery by k-nearest-neighbor simplex based on adaptive c-mutual proportion standard deviation metric. *Journal of Applied Remote Sensing* 8.

Chen, Y. P., H. Q. Fan, B. Xu, Z. C. Yan, Y. Kalantidis, M. Rohrbach, S. C. Yan and J. S. Feng. 2019. Drop an octave: Reducing spatial redundancy in convolutional neural networks with octave convolution. Pages 3434–3443 in *Proceedings IEEE/CVF International Conference on Computer Vision (ICCV)*, Seoul, South Korea, 27 Oct.–2 Nov. 2019.

Chen, Y. S., Z. H. Lin, X. Zhao, G. Wang and Y. F. Gu. 2014. Deep learning-based classification of hyperspectral data. *IEEE Journal of Selected Topics in Applied Earth Observations and Remote Sensing* 7(6):2094–2107.

Chen, Y.S., X. Zhao and X.P. Jia, 2015. Spectral-spatial classification of hyperspectral data based on deep belief network. *IEEE Journal of Selected Topics in Applied Earth Observations and Remote Sensing* 8(6):2381–2392.

Chen, Y. S., L. Zhu, P. Ghamisi, X. P. Jia, G. Y. Li and L. Tang. 2017. Hyperspectral images classification with Gabor filtering and convolutional neural network. *IEEE Geoscience and Remote Sensing Letters* 14(12):2355–2359.

Crawford, M. M., J. S. Ham, Y. C. Chen and J. D. Ghosh. 2004. Random forests of binary hierarchical classifiers for analysis of hyperspectral data. Pages 337–345 in *Proceedings IEEE Workshop on Advances in Techniques for Analysis of Remotely Sensed Data held in Honor of David A Landgrebe*, NASA Goddard Space Flight Visitor Ctr, Greenbelt, Md.

Dalla Mura, M., A. Villa, J. A. Benediktsson, J. Chanussot and L. Bruzzone. 2011. Classification of hyperspectral images by using extended morphological attribute profiles and independent component analysis. *IEEE Geoscience and Remote Sensing Letters* 8(3):542–546.

Du, B., R. Zhao, L. P. Zhang and L. F. Zhang, 2016. A spectral-spatial based local summation anomaly detection method for hyperspectral images. *Signal Processing* 124:115–131.

Fauvel, M., Y. Tarabalka, J. A. Benediktsson, J. Chanussot and J. C. Tilton. 2013. Advances in spectral-spatial classification of hyperspectral images. *Proceedings of the IEEE* 101(3):652–675.

Feng, F., S. T. Wang, C. Y. Wang and J. Zhang. 2019. Learning deep hierarchical spatial-spectral features for hyperspectral image classification based on residual 3d-2d CNN. *Sensors* 19(23).

Ghamisi, P., E. Maggiori, S. T. Li, R. Souza, Y. Tarabalka, G. Moser, A. De Giorgi, L. Y. Fang, Y. S. Chen, M. M. Chi, S. B. Serpico and J. A. Benediktsson. 2018. New frontiers in spectral-spatial hyperspectral image classification the latest advances based on mathematical morphology, Markov random fields, segmentation, sparse representation, and deep learning. *IEEE Geoscience and Remote Sensing Magazine* 6(3):10–43.

Gu, J. X., Z. H. Wang, J. Kuen, L. Y. Ma, A. Shahroudy, B. Shuai, T. Liu, X. X. Wang, G. Wang, J. F. Cai and T. Chen. 2018. Recent advances in convolutional neural networks. *Pattern Recognition* 77:354–377.

Guo, A.J.X. and F. Zhu. 2021. Improving deep hyperspectral image classification performance with spectral unmixing. *Signal Processing* 183.

Ham, J., Y. C. Chen, M. M. Crawford and J. Ghosh. 2005. Investigation of the random forest framework for classification of hyperspectral data. *IEEE Transactions on Geoscience and Remote Sensing* 43(3):492–501.

He, L., J. Li, C. Y. Liu and S. T. Li. 2018. Recent advances on spectral-spatial hyperspectral image classification: An overview and new guidelines. *IEEE Transactions on Geoscience and Remote Sensing* 56(3):1579–1597.

He, N. J., M. E. Paoletti, J. M. Haut, L. Y. Fang, S. T. Li, A. Plaza and J. Plaza. 2019. Feature extraction with multiscale covariance maps for hyperspectral image classification. *IEEE Transactions on Geoscience and Remote Sensing* 57(2):755-769.

Heydari, S. S. and G. Mountrakis. 2019. Meta-analysis of deep neural networks in remote sensing: A comparative study of mono-temporal classification to support vector machines. *ISPRS Journal of Photogrammetry and Remote Sensing* 152:192–210.

Hosseini, R. S., S. Homayouni and R. Safari. 2012. Modified algorithm based on support vector machines for classification of hyperspectral images in a similarity space. *Journal of Applied Remote Sensing* 6.

Hu, W., Y. Y. Huang, L. Wei, F. Zhang and H. C. Li. 2015. Deep convolutional neural networks for hyperspectral image classification. *Journal of Sensors*. https://doi.org/10.1155/2015/258619.

Jianing, W., G. Siying, H. Runhu, L. Linhao, Z. Xiangrong and J. Licheng. 2022. Dual-channel capsule generation adversarial network for hyperspectral image classification. *IEEE Transactions on Geoscience and Remote Sensing* 60:16.

Kang, B. and S. Kim. 2021. Analysis of the influence of 3d-cnn on spatial random information in hyperspectral image classification. Pages 1123–1126 in *Proceedings 21st International Conference on Control, Automation and Systems (ICCAS)*, South Korea.

Kang, X. D., X. L. Xiang, S. T. Li and J. A. Benediktsson. 2017. PCA-based edge-preserving features for hyperspectral image classification. *IEEE Transactions on Geoscience and Remote Sensing* 55(12):7140–7151.

Karim, F., S. Majumdar, H. Darabi and S. Chen. 2018. LSTM fully convolutional networks for time series classification. *IEEE Access* 6:1662–1669.

Khan, M. J., H. S. Khan, A. Yousaf, K. Khurshid and A. Abbas. 2018. Modern trends in hyperspectral image analysis: A review. *IEEE Access* 6:14118–14129.

Lei, R. M., C. J. Zhang, W. C. Liu, L. Zhang, X. Y. Zhang, Y. C. Yang, J. W. Huang, Z. X. Li and Z. Y. Zhou. 2021. Hyperspectral remote sensing image classification using deep convolutional capsule network. *IEEE Journal of Selected Topics in Applied Earth Observations and Remote Sensing* 14:8297–8315.

Liang, L., J. D. Cao, X. Y. Li and A. N. You. 2019. Improvement of residual attention network for image classification. Pages 529–539 in *Proceedings 9th International Conference on Intelligence Science and Big Data Engineering (IScIDE)*, Nanjing, Peoples R China.

Liu, B., X. C. Yu, A. Z. Yu and G. Wan. 2018. Deep convolutional recurrent neural network with transfer learning for hyperspectral image classification. *Journal of Applied Remote Sensing* 12(2).

Liu, P., H. Zhang and K. B. Eom. 2017. Active deep learning for classification of hyperspectral images. *IEEE Journal of Selected Topics in Applied Earth Observations and Remote Sensing* 10(2):712–724.

Liu, S. Y. and W. H. Deng. 2015. Very deep convolutional neural network based image classification using small training sample size. Pages 730–734 in *Proceedings 3rd IAPR Asian Conference on Pattern Recognition (ACPR)*, Kuala Lumpur, Malaysia.

Liu, X. F., Q. Q. Sun, Y. Meng, M. Fu and S. Bourennane. 2018. Hyperspectral image classification based on parameter-optimized 3d-cnns combined with transfer learning and virtual samples. *Remote Sensing* 10(9).

Ma, X. R., J. Geng and H. Y. Wang. 2015. Hyperspectral image classification via contextual deep learning. *Eurasip Journal on Image and Video Processing*. https://doi.org/10.1186/s13640-015-0071-8.

Makantasis, K., K. Karantzalos, A. Doulamis and N. Doulamis. 2015. Deep supervised learning for hyperspectral data classification through convolutional neural networks. Pages 4959–4962 in *Proceedings IEEE International Geoscience and Remote Sensing Symposium (IGARSS)*, Milan, Italy.

Marconcini, M., G. Camps-Valls and L. Bruzzone. 2009. A composite semisupervised SVM for classification of hyperspectral images. *IEEE Geoscience and Remote Sensing Letters* 6(2):234–238.

Peng, J. T., Y. C. Zhou and C.L.P. Chen. 2015. Region-kernel-based support vector machines for hyperspectral image classification. *IEEE Transactions on Geoscience and Remote Sensing* 53(9):4810–4824.

Peyghambari, S. and Y. Zhang. 2021. Hyperspectral remote sensing in lithological mapping, mineral exploration, and environmental geology: An updated review. *Journal of Applied Remote Sensing* 15(3).

Prabukumar, M., S. Sawant, S. Samiappan and L. Agilandeeswari. 2018. Three-dimensional discrete cosine transform-based feature extraction for hyperspectral image classification. *Journal of Applied Remote Sensing* 12(4).

Pu, S. L., Y. F. Wu, X. Sun and X. T. Sun. 2021. Hyperspectral image classification with localized graph convolutional filtering. *Remote Sensing* 13(3).

Roy, S. K., G. Krishna, S. R. Dubey and B. B. Chaudhuri. 2020. Hybridsn: Exploring 3-d-2-d CNN feature hierarchy for hyperspectral image classification. *IEEE Geoscience and Remote Sensing Letters* 17(2):277–281.

Salman, M. and S. E. Yuksel. 2016. Hyperspectral data classification using deep convolutional neural networks. Pages 2129–2132 in *Proceedings 24th Signal Processing and Communication Application Conference (SIU)*, Zonguldak, Turkey.

Song, W. W., S. T. Li, L. Y. Fang and T. Lu. 2018. Hyperspectral image classification with deep feature fusion network. *IEEE Transactions on Geoscience and Remote Sensing* 56(6):3173–3184.

Tarabalka, Y., M. Fauvel, J. Chanussot and J. A. Benediktsson. 2010. SVM- and MRF-based method for accurate classification of hyperspectral images. *IEEE Geoscience and Remote Sensing Letters* 7(4):736–740.

Vantaram, S. R., S. Piramanayagam, E. Saber and D. Messinger. 2015. Spatial segmentation of multi/hyperspectral imagery by fusion of spectral-gradient-textural attributes. *Journal of Applied Remote Sensing* 9.

Wang, L., H. C. Li, B. Xue and C. I. Chang. 2017. Constrained band subset selection for hyperspectral imagery. *IEEE Geoscience and Remote Sensing Letters* 14(11):2032–2036.

Wu, Y., L. J. Zheng, D. H. Xie, R. F. Zhong and Q. Chen. 2017. Classification of high-resolution multispectral satellite remote sensing images using extended morphological attribute profiles and independent component analysis. In *Proceedings 9th International Conference on Digital Image Processing (ICDIP)*, 2017, Hong Kong, Peoples R China, 19–22 May 2017. https://doi.org/10.1117/12.2281770.

Xi, B. B., J. J. Li, Y. S. Li, R. Song, Y. C. Xiao, Q. Du and J. Chanussot. 2022. Semisupervised cross-scale graph prototypical network for hyperspectral image classification. *IEEE Transactions on Neural Networks and Learning Systems*. https://doi.org/10.1109/TNNLS.2022.3158280.

Xia, J. S., J. Chanussot, P. J. Du and X. Y. He. 2016a. Rotation-based support vector machine ensemble in classification of hyperspectral data with limited training samples. *IEEE Transactions on Geoscience and Remote Sensing* 54(3):1519–1531.

Xia, J. S., N. Falco, J. A. Benediktsson, J. Chanussot and P. J. Du. 2016b. Class-separation-based rotation forest for hyperspectral image classification. *IEEE Geoscience and Remote Sensing Letters* 13(4):584–588.

Xu, Q., Y. Xiao, D. Y. Wang and B. Luo. 2020. Csa-mso3dcnn: Multiscale octave 3d CNN with channel and spatial attention for hyperspectral image classification. *Remote Sensing* 12(1).

Xu, R. D., Y. T. Tao, Z. Y. Lu and Y. F. Zhong. 2018. Attention-mechanism-containing neural networks for high-resolution remote sensing image classification. *Remote Sensing* 10(10).

Yan, J., K. Zhou, J. Wang, S. Wang, W. Wang and D. Li. 2013. Extraction of hyper-spectral remote sensing alteration information based on SAM and SVM. *Computer Engineering and Application* 49(19):141–146.

Yu, C. Y., F. Li, C. I. Chang, K. Cen and M. Zhao. 2020. Deep 2d convolutional neural network with deconvolution layer for hyperspectral image classification. Pages 149–156 in *Proceedings 7th International Conference on Communications, Signal Processing, and Systems (CSPS)*, Dalian, Peoples R China.

Yu, J., D. Y. Liang, B. Han and H. T. Gao. 2021a. Study on ground object classification based on the hyperspectral fusion images of zy-1(02d) satellite. *Journal of Applied Remote Sensing* 15(4).

Yu, X. M., Y. Feng, Y. L. Gao, Y.B. Jia and S. H. Mei. 2021b. Dual-weighted kernel extreme learning machine for hyperspectral imagery classification. *Remote Sensing* 13(3).

Zabalza, J., J. C. Ren, J. B. Zheng, J. W. Han, H. M. Zhao, S. T. Li and S. Marshall. 2015. Novel two-dimensional singular spectrum analysis for effective feature extraction and data classification in hyperspectral imaging. *IEEE Transactions on Geoscience and Remote Sensing* 53(8):4418–4433.

Zhang, J., L. Chen, X. Liang, L. Zhuo and Q. Tian. 2019. Hyperspectral image secure retrieval based on encrypted deep spectral-spatial features. *Journal of Applied Remote Sensing* 13(1).

Zhong, Z. L., J. Li, Z. M. Luo and M. Chapman. 2018. Spectral-spatial residual network for hyperspectral image classification: A 3-d deep learning framework. *IEEE Transactions on Geoscience and Remote Sensing* 56(2):847–858.

Zhu, M. H., L. C. Jiao, F. Liu, S. Y. Yang and J. N. Wang. 2021. Residual spectral-spatial attention network for hyperspectral image classification. *IEEE Transactions on Geoscience and Remote Sensing* 59(1):449–462.

Call for *PE&RS* Special Issue Submissions

Innovative Methods for Geospatial Data using Remote Sensing and GIS

Internationally comparable data is a global need for managing resources, monitoring current trends and taking actions for sustainable living. Even though there has been a significant progress on geospatial data availability, extensive data gaps are still a major problem for general assessment and supervise the progress through the years. According to United Nations 2022 The Sustainable Development Goals Report, while health and energy sectors have the highest data available, limited data available for climate action.

The COVID-19 crisis has also shown that there are innovative data collection methods utilizing information and computer technologies. However, only 5% of the countries have benefit from remote sensing technologies to measure the impact of COVID-19. Additionally, novel approaches such as artificial intelligence should be used in conjunction with assessments to make sure they are put to use for critical situations.

The recent developments in remote sensing, geographic information systems and ICT have provided a wide accessibility to create geospatial data for various purposes. The proposed special issue focuses on *"Innovative Methods for Geospatial Data using Remote Sensing and GIS" for wide range of applications. This special issue aims to bring researchers to share knowledge and their expertise about innovative methods to contribute to fill data gaps around the world for a better future.*

The proposed special issue aims to contributes ASPRS's key mission on 'Simplify and promote the use of image-based geospatial technologies for the end-user', 'Promote collaboration between end users and geospatial experts to match data and technology to applications and solutions' and 'promote the transfer of geospatial data and information technology to developing nations' by providing innovative methods to create geospatial data using remote sensing and geographic information systems utilizing state-of-the-art developments and solutions.

Deadline for Manuscript Submission—July 1, 2023

Submit your Manuscript to http://asprs-pers.edmgr.com

Guest Editors

Dr. Tolga Bakirman, bakirman@yildiz.edu.tr , *Yildiz Technical University, Department of Geomatic Engineering*, Davutpasa Campus, 34220 Esenler-Istanbul/Turkey

Dr. George Arampatzis, garampatzis@pem.tuc.gr, *Technical University Crete, School of Production Engineering & Management*, 73100 Chania – Crete/Greece

Model-Driven Precise Degradation Analysis Method of Highway Marking Using Mobile Laser Scanning Point Clouds

Ruifeng Ma, Xuming Ge, Qing Zhu, Xin Jia, Huiwei Jiang, Min Chen, and Tao Liu

Abstract

Highway markings (HMs) are representative elements of inventory digitalization in highway scenes. The accurate position, semantics, and maintenance information of HMs provide significant support for the intelligent management of highways. This article presents a robust and efficient approach for extracting, reconstructing, and degrading analyzing HMs in complex highway scenes. Compared with existing road marking extraction methods, not only can extract HMs in presence of wear and occlusion from point clouds, but we also perform a degradation analysis for HMs. First, the HMs candidate area is determined accurately by sophisticated image processing. Second, the prior knowledge of marking design rules and edge-based matching model that leverages the standard geometric template and radiometric appearance of HMs is used for accurately extracting and reconstructing solid lines and nonsolid markings of HMs, respectively. Finally, two degradation indicators are constructed to describe the completeness of the marking contour and consistency within the marking. Comprehensive experiments on two existing highways revealed that the proposed methods achieved an overall performance of 95.4% and 95.4% in the recall and 93.8% and 95.5% in the precision for solid line and nonsolid line markings, respectively, even with imperfect data. Meanwhile, a database can be established to facilitate agencies' efficient maintenance.

Introduction

Three-dimensional (3D) spatial virtual construction technology is of great significance for the development of smart highways. The accurate position and semantics of highway markings (HMs) provide significant support for highway digital operation, maintenance, and intelligent management. Highway marking is a representative element for the digitization of highway inventory and is also necessary to realize highway alignment extraction and modeling (Zhou *et al.* 2021).

In recent years, airborne light detection and ranging (lidar) scanning technologies have been widely used to acquire dense point clouds for various applications, such as 3D city modeling and digital elevation model generation (Guan *et al.* 2014; Yang *et al.* 2017; Zhu *et al.* 2022). However, mobile laser scanning (MLS) efficiently, reliably, and cost-effectively acquires high-density, high-precision, and multi-detail 3D point clouds of corridor scenes (Guan *et al.* 2014; Mi *et al.* 2021; Rastiveis *et al.* 2019; Wang *et al.* 2017; Yan *et al.* 2016; Zai *et al.* 2018), which provides convenience for road surface features (e.g., road marking) extraction and reconstruction for timely road maintenance. An MLS is the integration of several devices, including a laser scanner, a global navigation satellite system (GNSS), an inertial measurement unit (IMU), high-resolution cameras, and a computer control device (Kumar *et al.* 2014). In complex highway scenes, due to severe noise, diverse terrain, and the existence of varying wear, occlusion, robust extraction, and reconstruction of HMs using MLS point clouds still have some unsolved problems in current engineering applications (Jung *et al.* 2019; Mi *et al.* 2021).

A great number of methods discussed in the section "Related Works" have been developed for automatic extraction, classification, and reconstruction based on the geometric features and reflection intensity of the MLS point clouds in corridor scenes, which also improved the automation level of HM extraction to a certain extent. However, most methods including raster-based and point-based both currently use bottom-up strategies, which are sensitive to imperfect raw data and difficult to apply for extracting HMs in complex highway scenes. Moreover, in existing methods, there are few reports on conducting a degradation analysis of the highway markings for further maintenance. This study presents an automatic method for extraction and degradation analysis of HMs by MLS point clouds. The proposed method extracts the candidate area of solid lines and nonsolid markings (including dashed lines and various types of complicated arrow markings) from the intensity feature map generated by pavement point clouds. The prior knowledge of marking design rules and edge-based matching is used for accurately extracting and reconstructing solid lines and nonsolid markings, respectively. Two degradation indicators are constructed to describe the completeness of the marking contour and consistency within the marking, which can be useful for authorities to further assess maintenance. The main contributions of the proposed method are as follows:

(1) A new framework that not only achieves the fine reverse modeling of HMs at the digital dimension but also implemented degradation analysis for actual operation of highway marking is presented.

(2) After projecting the MLS point clouds to feature map, a dynamic threshold segmentation is designed to identify candidates for highway marking. Within the candidate, the model-driven strategy and the road marking design rules are adopted to accurately extract and reconstruct highway marking in terms of good robustness to severe noise, the uneven density of the point clouds, wear, and occlusion of highway markings.

(3) Two degradation indicators from different aspects are constructed to reflect the condition of marking objects for further maintenance.

The remainder of this paper is organized as follows. After introducing the related work in the section "Related Works", we describe the

Ruifeng Ma, Xin Jia, and Tao Liu are with the Faculty of Geomatics, Lanzhou Jiaotong University, Lanzhou, China.

Ruifeng Ma, Xuming Ge, Qing Zhu, Xin Jia, and Min Chen are with the Faculty of Geosciences and Environmental Engineering, Southwest Jiaotong University, Chengdu, China. (xuming.ge@swjtu.edu.cn).

Huiwei Jiang is with the National Geomatics Center of China, Beijing, 100830, China.

Ruifeng Ma is also with the Academician Expert Workstation of Gansu Dayu Jiuzhou Space Information Technology CO., Ltd.

Min Chen is also with the Key Laboratory of Urban Land Resources Monitoring and Simulation, Ministry of Natural Resources, Shenzhen, China.

proposed method in the "Methods" section. We report the results and discussion of experiments and associated analysis in the section "Results and Discussion" and present our conclusions in the final section.

Related Works

Generally, the material of road markings is a highly reflective substance attached to the road of asphalt or concrete. Therefore, road markings have a higher intensity than their surroundings on the road surface and have regular shapes. Accordingly, a variety of methods for road marking extraction are mainly categorized into two classes depending on semantic knowledge (e.g., shape) and MLS intensity properties (Bello *et al.* 2020; Guan *et al.* 2016; Ma *et al.* 2018): (1) raster-based methods and (2) point-based methods. Moreover, we review some work in terms of degradation analysis of road marking. These methods are discussed in the following subsections.

Extraction of Pavement Marking in Point Clouds

Raster-Based Methods

Raster-based methods convert the intensity or range of the point cloud into a two-dimensional (2D) feature image, which is then processed by the sophisticated algorithm of image processing to extract the markings. The point cloud index then uses a featured image of intensity to retrieve the markings from the original point cloud (Cheng *et al.* 2017; Cheng *et al.* 2020;Guo *et al.* 2015; Jung *et al.* 2019; Riveiro *et al.* 2015; Yang *et al.* 2012; Yao and Hu 2014). This method takes advantage of the characteristic that the road has a local near-plane, which treats the road surface as a regular two-dimensional image and extracts road markings quickly and efficiently through image threshold segmentation. However, the MLS point clouds provide an intensity attribute that depends not only on the marking material but also the range and incidence angle of the laser beam (Kashani *et al.* 2015). Therefore, it is difficult to accurately extract markings by relying on only a single threshold value. To solve this problem, the intensity correction and normalization of the original point clouds are performed based on the assumption of a relatively consistent geometry of the point cloud on the road, taking into account the influence of the measured distance and angle of incidence (Fang *et al.* 2019; Guan *et al.* 2015a; Guan *et al.* 2015 b; Jaakkola *et al.* 2008; Kumar *et al.* 2014; Soilán *et al.* 2017; Yan *et al.* 2016; Zhang 2016). Another method that is used to extract markings is by combining the relationship between the intensity and the scanning distance. This method can be used to overcome the issue of uneven intensity and varying density due to the varying scanning modes (Guan, *et al.* 2015 b ; Kumar *et al.* 2014; Soilán *et al.* 2017; Yu *et al.* 2017). Unfortunately, raster-based image methods are prone to causing information loss when converting point clouds into raster images. Moreover, it is difficult to accurately extract complex types of road markings. In addition, Wen *et al.* (2019) present a deep, learning-based framework for road marking extraction, classification, and completion for MLS point cloud. U-Net was adopted to segment the intensity raster image into a binary image with foreground and background. The foreground blocks were further classified into kinds of road marking categories, and a completion operation GAN based was applied for incomplete objects. Chen *et al.* (2021) proposed a dense feature pyramid network-based deep learning model, by considering the particularity and complexity of road marking. However, image-based deep learning methods require many labeled samples, labeling training samples is time-consuming and sometimes even impossible.

Point-Based Methods

Raster-based methods are commonly used to extract road markings by MLS point clouds, but this method is not ideal for accurately extracting markings from complex road sections. Several studies have been conducted to develop a method that can directly extract road markings from point clouds (Chen *et al.* 2009; Ma *et al.* 2019; Soilán *et al.* 2020; Yan *et al.* 2016; Yang *et al.* 2017; Yang *et al.* 2018). Although point-based methods can avoid the drawback of converting point clouds to images, they require a large computational and time cost. To overcome the shortcoming of point-based methods, k-dimensional tree

is introduced to organize the data structure of point clouds to improve efficiency. In addition, according to the MLS scan time, the point cloud is first partitioned into a scan-by-scan line (Chen *et al.* 2009; Yan *et al.* 2016; Yang *et al.* 2018), and then parallel computing is used to improve the efficiency of the algorithm (Che *et al.* 2019). However, the automatic extraction of road markings from the massive MLS point clouds is still a very difficult task. Recently, many studies have been conducted on automatic road marking classification by using deep learning-based neural networks (e.g., PointNet and PointCNN) (Han *et al.* 2021; Li *et al.* 2018; Qi *et al.* 2017; Yao *et al.* 2020) in large-scale scenes, and the performance has enhanced significantly compared with hand-designed feature based methods (Ge *et al.* 2019). However, deep learning-based methods also have some challenges, i.e., (1) deep learning methods are typically data-hungry and require many labeled samples; and (2) more fundamental issues include numerous geometric instances, data imbalance, and extreme scale variations between different categories in large-scale MLS point clouds scenes

Degradation Analysis

The completeness and luminous reflectance of road markings has a significant impact on its function (such as driving safety). It is therefore urgent that the road maintenance department regularly conducts an assessment of markings to ascertain any degradation or damage and perform timely maintenance where necessary. In recent years, a series of methods for degradation analysis and damage assessment based on digital images (Spencer Jr *et al.* 2019) or laser measurement (Zhang *et al.* 2019) have been presented in various studies to enhance the efficiency of road maintenance. Numerous studies have used image-based to efficiently inspect damage or cracks in roads and bridges (Cha *et al.* 2018; Kawano *et al.* 2017; Kheyrollahi and Breckon 2012). Although image-based methods provide satisfactory inspection results for damage under well-lit and are generally less expensive than laser techniques, results obtained by these image-based approaches easily suffered from several factors such as variation of the illumination, weather conditions, and shadow.

Lidar is an alternative technique that is less sensitive to ambient light conditions for carrying out degradation analysis by modeling the relation between intensity and retroreflective luminance (Burghardt *et al.* 2021). In Soilán *et al.* (2022), a methodology was proposed that defines a road marking degradation model, which estimates the coefficient of retroreflected luminance using the intensity attribute of 3D point clouds. Jung *et al.* (2019) proposed a line association process to consider poorly worn lane markings such that the data can help agencies assess the condition of each individual stripe. Guo *et al.* (2015) computed the sum of absolute differences (SAD) value to provide the completeness of the road markings. The user could then undertake repair judgments based on the SAD values.

Methods

The proposed framework is illustrated in Figure 1. The main steps of automatic extraction and reconstruction of HMs in existing highway scenes based on MLS point clouds include (1) preprocessing and pavement extraction; (2) identifying objects of candidate markings; and (3) HM extraction and reconstruction; (4) highway markings degradation analysis.

Point Cloud Preprocessing and Pavement Extraction

Firstly, we carried out the intensity value revised in the preprocessing. To overcome the effect of scanning distance (angle of incidence) on the intensity of point clouds, we use the trajectory obtained by the MLS to correct the intensity value based on the distance from each point to the trajectory to revise pointwise. Then, highway pavement was extracted after projecting point cloud to image based on the various attribute of the point.

Point Cloud Intensity Revision

The point cloud intensity values are corrected pointwise using the distance to the trajectory. According to Korpela *et al.* (2010), the intensity of the point cloud was revised and normalized by the following equation:

$$I_{Ran} = (R/R_{Ref})^a \cdot I_{raw} \tag{1}$$

where I_{Ran} is the range normalized intensity; R is the range; R_{Ref} is a mean reference range; $\alpha \in [2,4]$ is the exponent that is, according to theory, dependent on the target geometry.

Intensity Raster Image Extraction of Pavement

Before extracting a raster image of pavement, it is necessary to filter the point cloud and generate multi-feature maps. To distinguish ground points and nonground points (guardrails, vegetation, vehicles, etc.), we use a bending energy filtering algorithm (Han *et al.* 2014) to filter ground and nonground points to generate multi-feature maps. Figure 2 shows the MLS point clouds collected in the complex environment highway scenes. Figure 3 shows filtering results.

Point cloud conversion to raster means that the 3D point cloud of pavement neglects the influence of elevation and approximates a 2D structure, in which the gray value of the 2D map can be obtained from the attribute characteristics of the point clouds. After point cloud filtering, we exploit a method for extracting pavement based on a multi-feature image (Pan *et al.* 2019). In this method, the intensity, elevation, and point density features of the point clouds are projected onto the 2D plane and generate grayscale feature maps for extracting raster images of pavement. The point clouds acquired by the mobile measuring system (MMS) are $P_i(X_i, Y_i, Z_i, I_i)$, (X_i, Y_i, Z_i) are 3D coordinates of point i,

and I_i is the intensity value. We take the intensity I_i as an example and project P_i onto the plane by neglecting their z coordinate components as follows:

$$(x_i, y_i)_{planar} = s(X_i, Y_i) \tag{2}$$

where (x_i, y_i) are the positions after projection and s is the scale parameter between the point clouds and projected points. We rasterize the point cloud and represent it as a grid:

$$(c_i, r_i) = \left(\frac{x_i - \min(x)}{R_{pixel}}, \frac{y_i - \min(y)}{R_{pixel}} \right) \tag{3}$$

where c_i and r_i are the image coordinates of each grid, and R_{pixel} is the grid size, which determines the size and level of detail of the produced image. When there are no projected points on a grid, 0 is used instead of the reflected intensity; when there are more than one projected point on grid, the pixel value is the average reflected intensity value of all points.

Based on the results of ground and nonground points filtered, the grid size R_{pixel} of the feature map is set according to the point cloud density when collected. The feature image Z_{avg}^{non-g} of nonground points
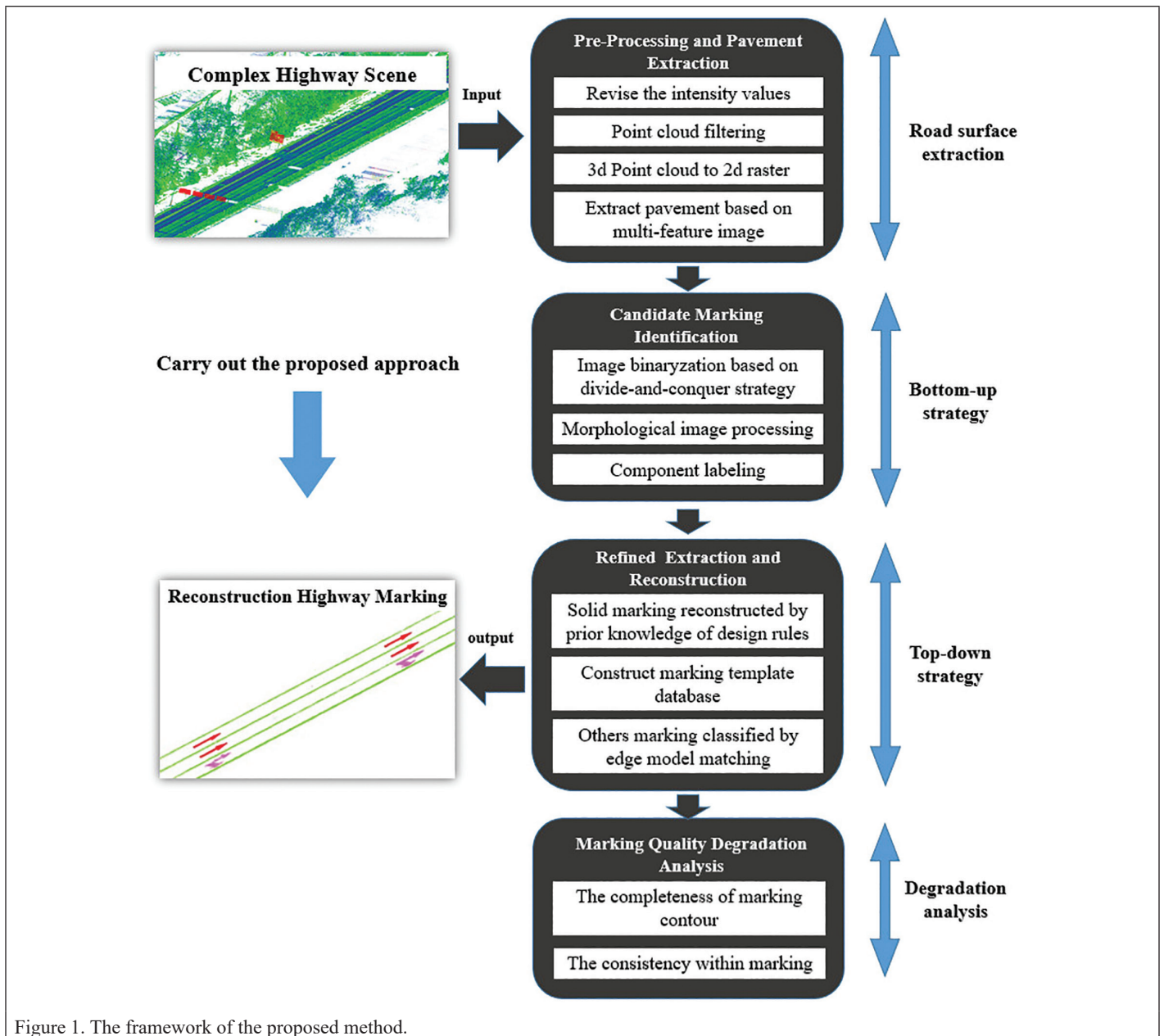

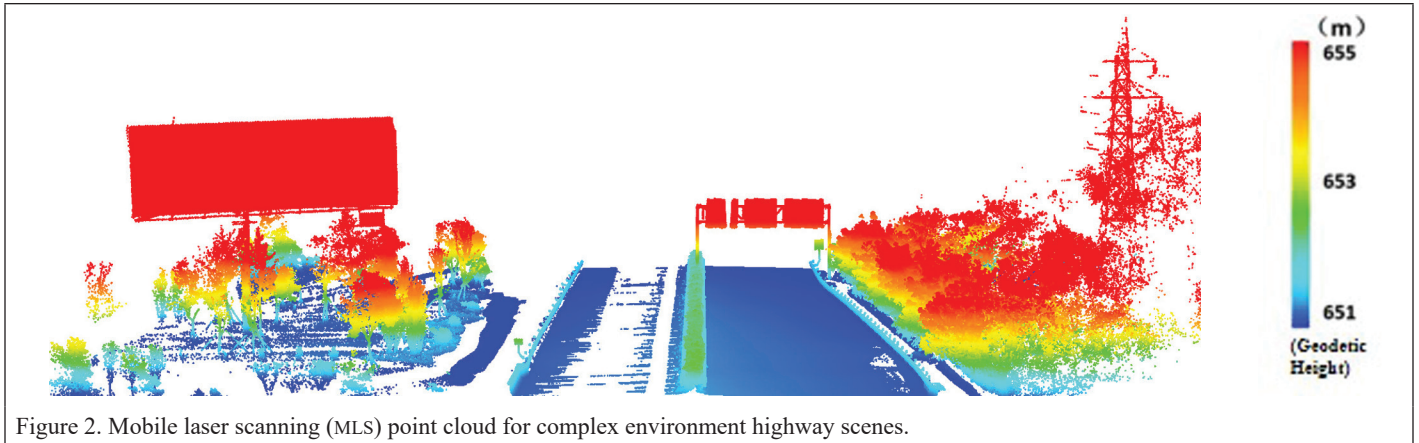Figure 1. The framework of the proposed method.

Figure 2. Mobile laser scanning (MLS) point cloud for complex environment highway scenes.
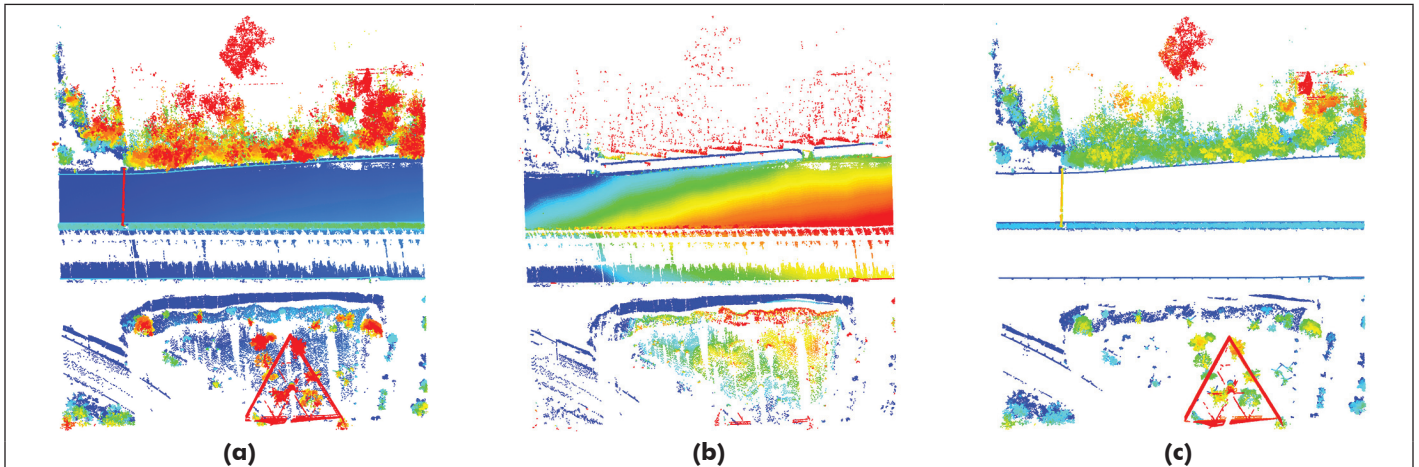

(a)   **(b)**   **(c)**

Figure 3. Point cloud filtering. (a) Original point cloud; (b) Ground points; (c) Nonground points.

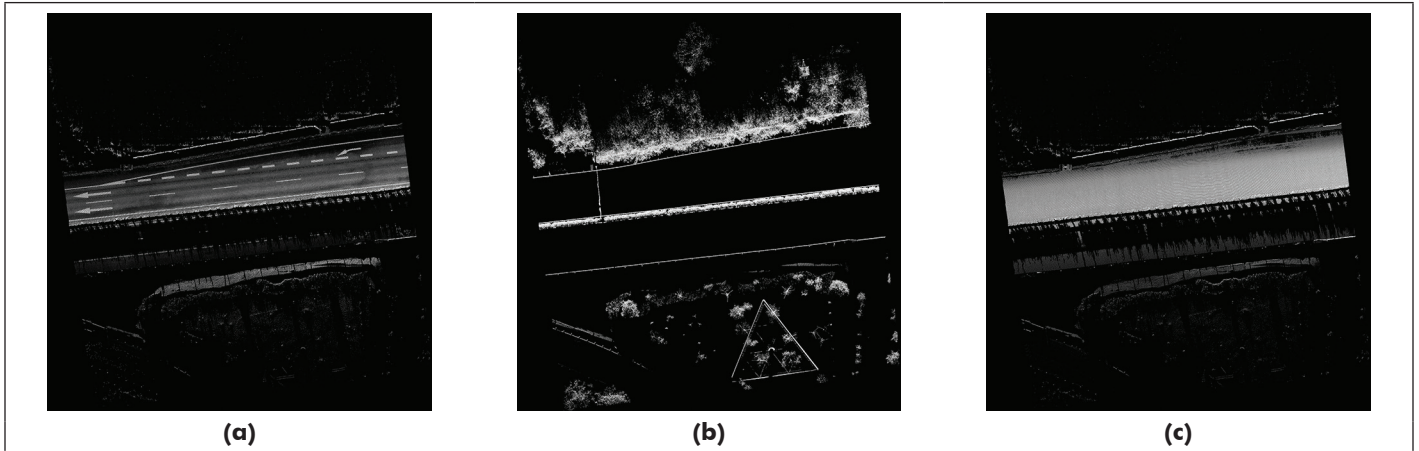**(a)**   **(b)**   **(c)**

Figure 4. Multi-feature raster map. (a) Intensity image of ground points; (b) Elevation image of nonground points; (c) Density image of ground points.

is generated by point elevation, and the feature images I_{avg}^g and D_{avg}^g of ground points are generated by the intensity and number of unit grid points, respectively. Figure 4 shows the generated feature map.

Equations 4 and 5 represent the workflow for extracting pavement intensity images based on the generated multiple feature maps. First, to generate the gradient image of denoised, median filtering and the Sobel operator are used to remove noise and extract edges from the nonground elevation feature map, respectively. Then, the nonground gradient binary map and point density binary map are generated by the nonground elevation gradient image and ground point density image using the max entropy thresholding method, respectively, in which slope and point density are set to 1 when they are greater than the threshold, and the rest are set to 0. Finally, according to the nonground gradient binary and point density binary maps, the nonroad area of

the intensity map was removed, in which the area with a large slope or sparse points was considered the area of nonroad in the ground. According to the results above, the pavement grid of intensity was retrieved on the intensity map of the ground. Moreover, the small-area noise was removed using area filtering, which used the number of pixels as a criterion.

$$\begin{cases} Z_{avg}^{non-g} \odot MF \to Z_{medianF}^{non-g} \odot SO \to Z_{sobel}^{non-g} \odot ME \to Z_{bin}^{non-g} \\ D_{avg}^g \odot ME \to D_{bin}^g \end{cases} \tag{4}$$

$$I_{avg}^g \begin{cases} \text{remove} & \text{if } Z_{bin}^{non-g} = 1 \text{ and } D_{bin}^g = 0 \\ I_{avg}^{road} & \text{others} \end{cases} \tag{5}$$
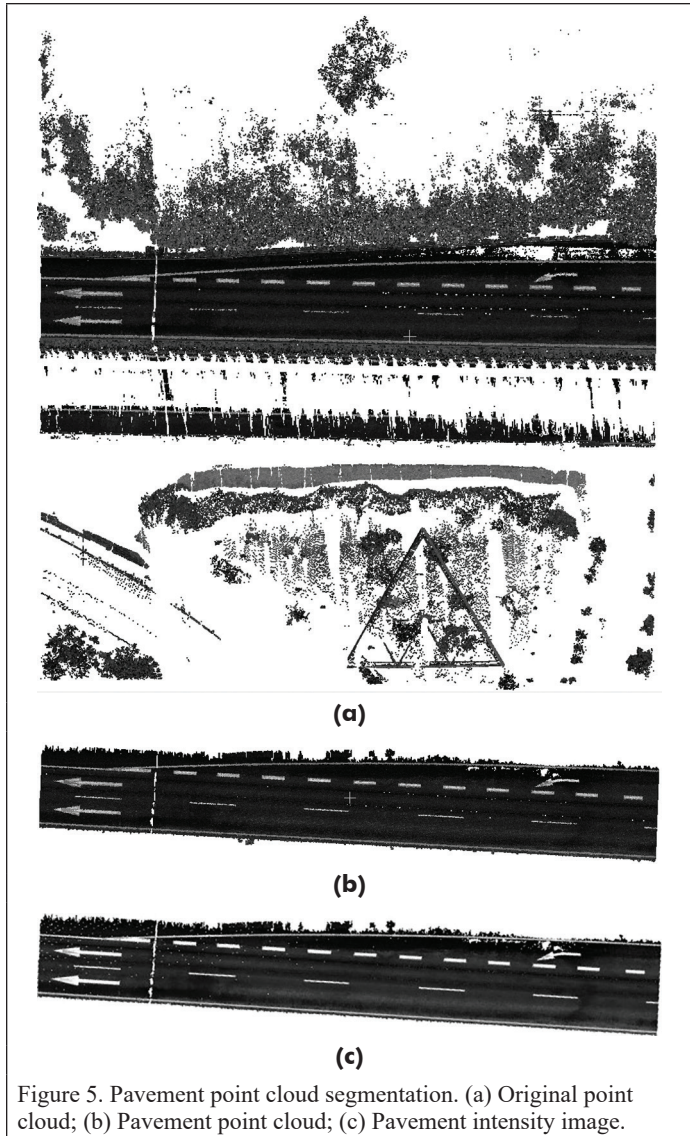
Figure 5. Pavement point cloud segmentation. (a) Original point cloud; (b) Pavement point cloud; (c) Pavement intensity image.

Where $\odot$ is the operator; MF, SO, and ME are the median filter, Sobel operator, and max entropy algorithm, respectively; and $Z_{medianF}^{non-g}$, Z_{sobel}^{non-g}, and Z_{bin}^{non-g} are the nonground elevation images after median filtering, Sobel edge image, and max entropy binary image, respectively. D_{bin}^{g} is the ground intensity image after the max entropy thresholding method; I_{avg}^{road} is the extracted intensity image of pavement. Figure 5 shows the generated pavement intensity map.

Candidate Marking Identification

To overcome the severe noise and wear in existing highways and improve the robustness of the proposed method, we adopt a dynamic threshold segmentation algorithm to segment the pavement image into a binary image, further optimize the results using a morphological operator, and label the object of the extraction result using connected component analysis (CCA). Subsequently, the bounding box of each object is calculated to obtain the coarse positioning of the marking candidate area.

Binary Image Generation for Pavement Images Based on Dynamic Thresholding

The intensity revision of the points is performed by taking into account the distance from the original cloud point to the trajectory according to Equation 1. Although this process overcomes the effects of scanning distance as much as possible, it is not ideal for images with a large area when using the global threshold to obtain a binary image. In this paper, the divide-and-conquer strategy is adopted to overcome drawbacks using the global threshold. First, the image is partitioned into subblocks, and then, the max entropy method is used to automatically obtain the optimal threshold for each subblock. Although the dynamic threshold algorithm is used to preserve the candidate pixel of the road as completely as possible, a mass of nonmarking noise is also preserved. Therefore, we use morphology operators to optimize the results and obtain candidate objects of road markings by shape size.

Morphological Image Processing and Object Clustering

There are also various small size noises in the pavement binary image, and disconnected objects can also be caused by worn markings. To solve this problem, we use the morphological closing operation, which effectively connects different objects in the vicinity and makes the highway marking candidates more complete. Morphological processing can effectively optimize the binary image and connect disconnected and incomplete objects that belong to the same candidate region and make the candidate object more complete (see Figure 6).

After the morphological processing of the binary map, the image object remains an image object, not a candidate object for road
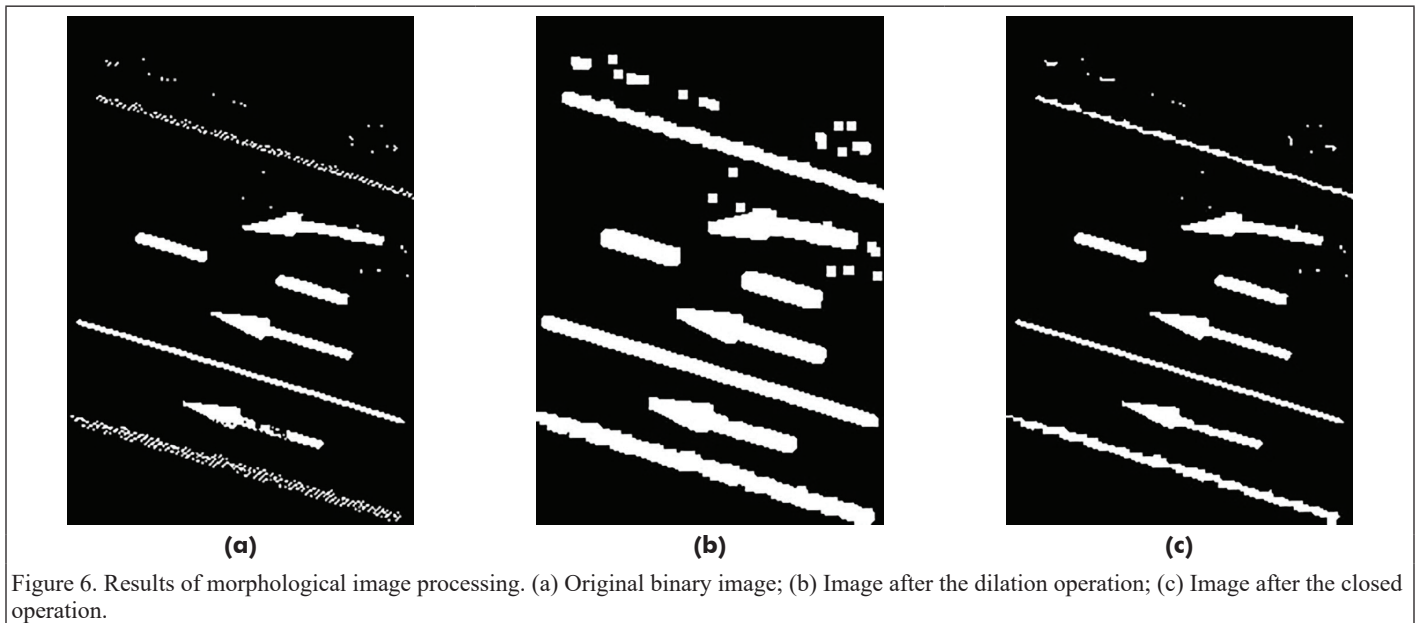

Figure 6. Results of morphological image processing. (a) Original binary image; (b) Image after the dilation operation; (c) Image after the closed operation.
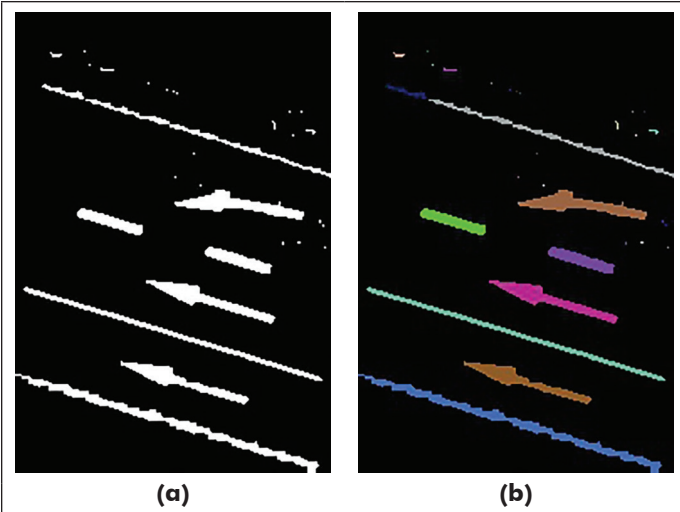
Figure 7. Illustration of object clustering and area filtering. (a) Morphological processing results; (b) Object clustering results.
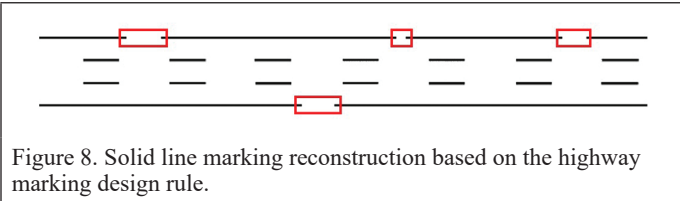

Figure 8. Solid line marking reconstruction based on the highway marking design rule.

marking. To solve this issue, the seed filling algorithm based on the CCA is used to cluster the neighboring image pixels into various candidate objects of HMs. After clustering, there is still small noise, which is removed by setting a certain number of pixel thresholds (area filtering). As shown in Figure 7, different colors represent different clustering objects and different candidate objects for HMs.

Refined Extraction and Reconstruction
After the clustering process has been completed, each image object becomes a candidate object for HMs. However, the HMs have not been extracted accurately and reconstructed. To overcome the flaws of the bottom-up strategy adopted by most existing research, we propose integrating rule-based methods and edge-based matching methods for HM refined extraction and construction.

Rule-Based Extraction and Reconstruction for Solid Line Marking
Solid line markings are lane lines on both sides of a highway that are continuous solid lines. Usually, solid line markings are large HMs; therefore, we use the geometric information to recognize the solid line marking. Some geometric variables are adopted, including minimum bounding box with length a, width b, aspect ratio σ_1, and the ratio of the area of the point cloud to the area of its external rectangle is σ_2. According to the highway specification, the standard width of the solid line is set as $solid_{width}$ and the clustering candidates that also satisfy the following equation are classified as a solid line type.

$$\begin{cases} \sigma_1 > \varphi_1 \\ \sigma_2 > \varphi_2 \\ |solid_{width} - b| < \varphi_3 \cdot solid_{width} \end{cases} \tag{6}$$

where φ_1 is a constraint on the length-width ratio of the minimum bounding box in the candidate object of highway markings, and the solid line highway marking aspect ratio should be set to a larger threshold, namely, set as $\varphi_1 = 8$. φ_2 indicates the restriction on the rectangularity of the clustering; φ_3 reflects the allowed difference in width between the clustered objects and the design dimensions.

The solid line marking was classified by the processing above. The solid line marking is obviously a continuous solid line; however, for

some reasons (wear and occlusion), they are sometimes broken. When breakage occurs, we connect and complete solid line markings based on the highway marking design rules (see Figure 8).

Edge-Based Matching for Precise Extraction and Reconstruction of Nonsolid Marking
After identifying the solid line markings, the remaining candidate objects of the nonsolid markings are grouped into different dashed lines and arrow highway markings. Firstly, the bounding box is extracted according to the clustering object of nonsolid markings (see Figure 10b), and then the intensity map is clipped according to the bounding box of each candidate area, and the small clipped image includes the complete object of nonsolid HMs. Finally, an edge-based matching algorithm is used to refine the extraction and reconstruction for nonsolid line HMs in a small image. Before carrying out matching, we constructed the template database according to the highway markings specification, including several highway templates such as the straight-ahead arrow, left-turn arrow, right-turn arrow, straight ahead or left-turn arrow, and straight ahead or right-turn arrow (see Figure 9). Using the top-down strategy above, only small images need to be searched without blind matching for the whole image, thus improving the efficiency and accuracy of HM extraction. Moreover, the edge-based matching algorithm overcomes the effects of wear and the intensity of noise; therefore, the extraction results are more robust to the intensity of noise. Figure 10 shows the refined extraction and reconstruction results for nonsolid line highway marking.

In the matching process, the template model should be compared to the search image at all locations using a similarity measure. The idea behind the similarity measure is to take the sum of all normalized dot products of gradient vectors of the template image and search the image overall points in the model data set. This results in a score at each point in the search image. This can be formulated as follows.

$$s_{u,v} = \frac{1}{n} \sum_{i=1}^{n} \frac{(Gx_i^T \cdot Gx_{(u+Xi,v+Yi)}^S) + (Gy_i^T \cdot Gy_{(u+Xi,v+Yi)}^S)}{\sqrt{Gx_i^{T^2} + Gy_i^{T^2}} \cdot \sqrt{Gx_{(u+Xi,v+Yi)}^{T^2} + Gy_{(u+Xi,v+Yi)}^{T^2}}} \tag{7}$$

where Gx_i^T and Gy_i^T are the gradient values of the x- and y-directions of the template image, respectively; $Gx_{(u+X_i, v+Y_i)}^S$ and $Gy_{(u+X_i, v+Y_i)}^S$ are the gradient values of the x- and y-directions of the corresponding points of the search image; and n is the number of edge points.

If there is a perfect match between the template model and the search image, this function will return a score of 1. The score corresponds to the portion of the object visible in the search image. If the object is not present in the search image, the score will be 0.

Highway Marking Degradation Analysis
To evaluate the condition of HMs, we quantitatively describe the degradation of HMs in terms of the completeness of the marking contour and the consistency within the marking combining the geometric appearance and radiation information of HMs. According to the section "Edge-Based Matching for Precise Extraction and Reconstruction of Nonsolid Marking", the score of the best edge-based template matching (SEM) is calculated by the similarity measure using the sum of all normalized dot products of gradient vectors and is obtained to estimate the completeness of the marking contour. The more severe the wear or the missing parts occurring on the marking contour, the lower the SEM is. According to the marking intensity map which has a strong relation to the radiation information of marking materials, the consistency within markings is estimated by the score of area-based template matching (SAM), which uses the sum of the normalized difference of squares matching method for calculations. The formula of SAM is modified for the binary map as follows.

$$SAM_{(x,y)} = 1 - \frac{\sum_{x',y'} T(x'+y') - I(x+x', y+y')}{\sqrt{\sum_{x',y'} T(x', y')^2 * \sum_{x',y'} I(x+x', y+y')^2}} \tag{8}$$
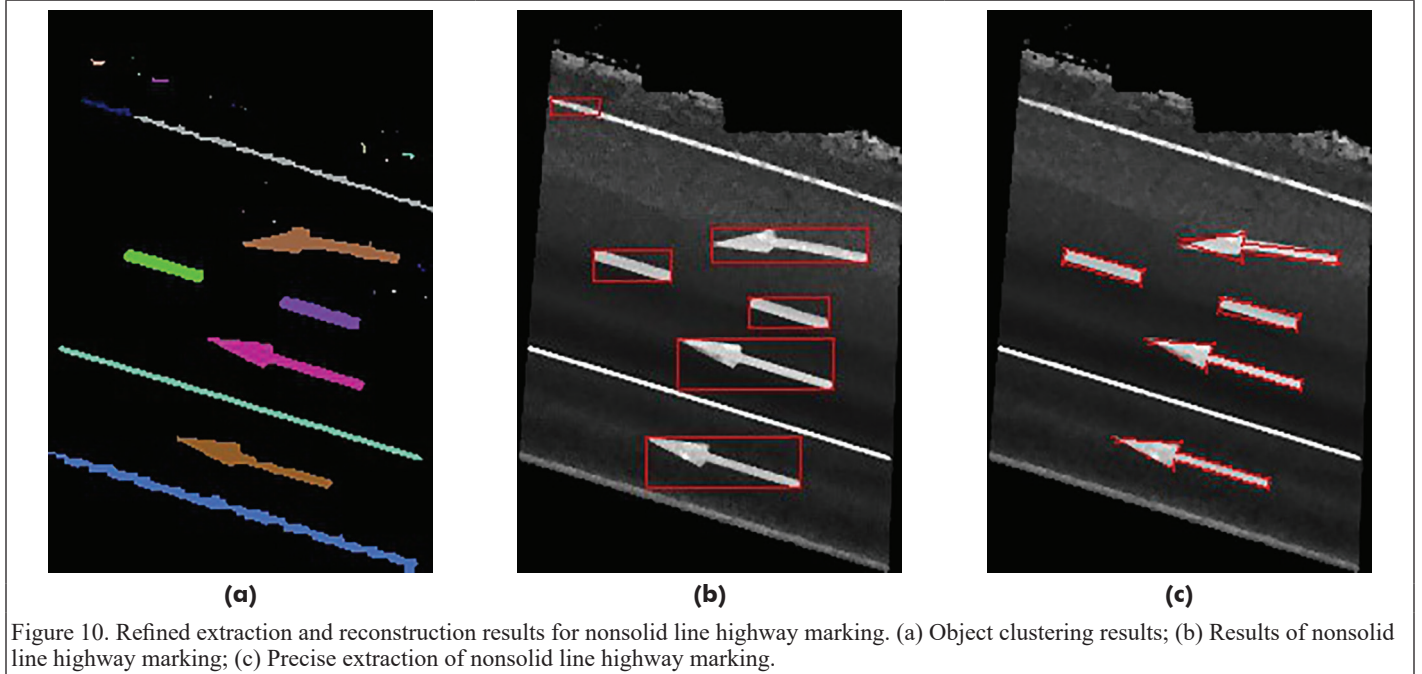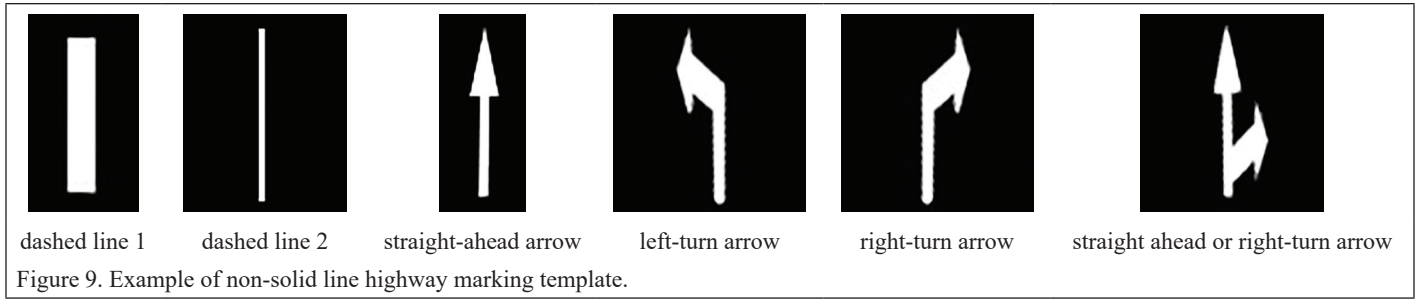
dashed line 1   dashed line 2   straight-ahead arrow   left-turn arrow   right-turn arrow   straight ahead or right-turn arrow

Figure 9. Example of non-solid line highway marking template.

(a)   **(b)**   **(c)**

Figure 10. Refined extraction and reconstruction results for nonsolid line highway marking. (a) Object clustering results; (b) Results of nonsolid line highway marking; (c) Precise extraction of nonsolid line highway marking.

Table 1. Performance index of the mobile laser scanning (MLS) system.

Parameters	Scan Point Frequency	Scanning Frequency	Measuring Distance	Field of View	Distance Measurement Accuracy
Performance index	≥50 million points/second	≥200 Hz	300 m	≥360°	≤6 mm ~40 m

where $T(x' + y')$ and $I(x + y)$ are the template and search image, respectively. The value of SAM matches the results and shows the similarity of the highway marking to the corresponding template. The larger the SAM value is, the better the consistency within the marking. For example, the drop in the SAM value might indicate wear and uneven intensity existing on the marking; simultaneously, and the marking requires repair.

Results and Discussion

Data Set Description
The efficiency of the proposed method was evaluated with two data sets, in which highway point clouds were both collected in Sichuan Province, Southwest China. An overview of the two sites is shown in Figure 12. The length of data sets A and B are 3.964 km and 12.854 km, respectively. Data set A was collected in the alpine and gorge areas, where there is a lot of rain all year round, and the heavy traffic of trucks causes serious wear on the markings. At the same time, there are many curves and highway marking types (see Figure 12a and 12c). Data set B was collected in a town adjoined by a city and country with heavy traffic causing a great many occlusions and wear (see Figure 12b and 12d). Table 2 provides quantitative descriptions of the two data sets. Compared with most existing studies, which have focused on extracting pristine markings on relatively new road surfaces, the highway in the two data sets is very challenging because it is used for a long

Figure 11. (a) Scanner configuration of iScan mobile measuring system (MMS); (b) Enlarged view of panorama and laser scanner; (c) Highway scene point cloud colored by intensity values.
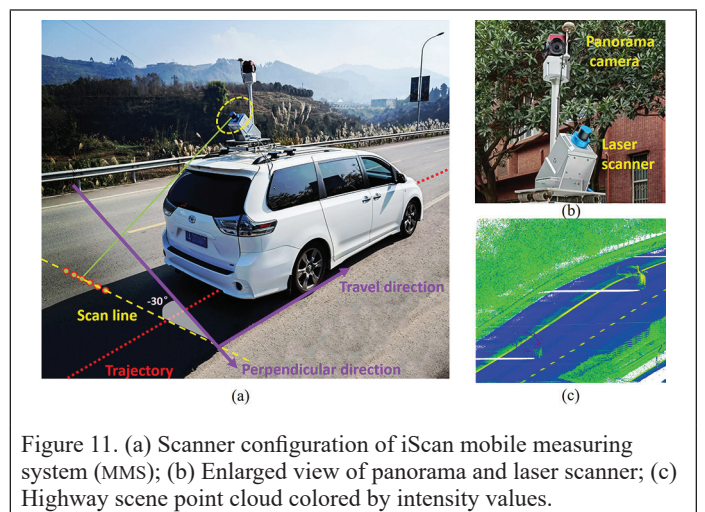
period with various wear markings and severe noise and is thus found to be adequate for demonstrating feasibility and reliability. Figure 11a shows the working process of the iScan MMS, and Figure 11b shows the panorama camera and laser scanner carried on the MMS. Table 1 lists the performance index of the MLS system. As shown in the scanner configuration, the scanner orientation was set to –30° (see Figure

11a), which is the angle between the perpendicular direction and scan line, to provide adequate coverage of the transverse at fast speeds, and trajectory data were obtained by the GNSS and IMU carried on the MMS. Figure 11c illustrates the collected point clouds color-coded by intensity values.

Experimental Results Analysis

Extraction and Reconstruction Results
We implemented all the programs in C++ with the open-source Point Cloud Library and Open Source Computer Vision Library (OpenCV). All experiments were carried out on a standard computer with 64

Table 2. Quantitative descriptions of the data sets A and B.

Data Sets	Road Length (km)	Scenario
A	3.964	the alpine and gorge areas
B	12.854	village area with overpasses

(a)

(b)

(c)

(d)

Figure 12. Overview of two test sites. (a) View of the scenario for data set A; (b) View of the scenario for data set B; (c) Data set A; (d) Data set B.

Table 3. Descriptions and settings of vital parameters.

Parameter	Description	Value
α	Exponent depending on the target geometry	3
R_{pixel}	Grid size of the feature map	0.8
φ_1	The length-width ratio of the minimum bounding box in the candidate object of highway markings (the solid line highway marking aspect ratio should be set to a larger threshold)	8
φ_2	Restriction on the rectangularity of the clustering	0.6
φ_3	Allowed difference in width between the clustered objects and the design dimensions	0.2
T_{low}	Low threshold	10
T_{high}	High threshold	100
S_{min}	Minimum score	0.85
g	Coefficient of greed	0.8

Figure 14. Highway marking extraction and reconstruction of data set B: a global overview; (a)–(c) are the enlarged typical stretches for detailed inspection.

GB RAM and an AMD Ryzen 7 5800X 8-Core Processor 3.80 GHz. In the section "Methods", several parameters and thresholds were introduced. In Table 3, we summarized and described them together with the values used for the validation of the method. The value of the parameters comes from previous knowledge of the problem, such as geometric properties of highway markings and standard value of highway specification, and an empirical verification that is needed in every methodology heavily based on heuristics. Figure 13 and Figure 14 show qualitative illustrations of the extraction and reconstruction results for HMs using the proposed approach from data sets A and B in complex highway scenes, respectively, where the global overviews are displayed and several typical road stretches are enlarged for detailed inspection. Figure 15 shows the HM extraction and reconstruction results using the proposed approach on a typical road stretch, where the HMs marked by the red rectangle are of wear and occlusion. Figure 16 shows the HM extraction and reconstruction results for a complex existing road stretch with various point densities and intensities.
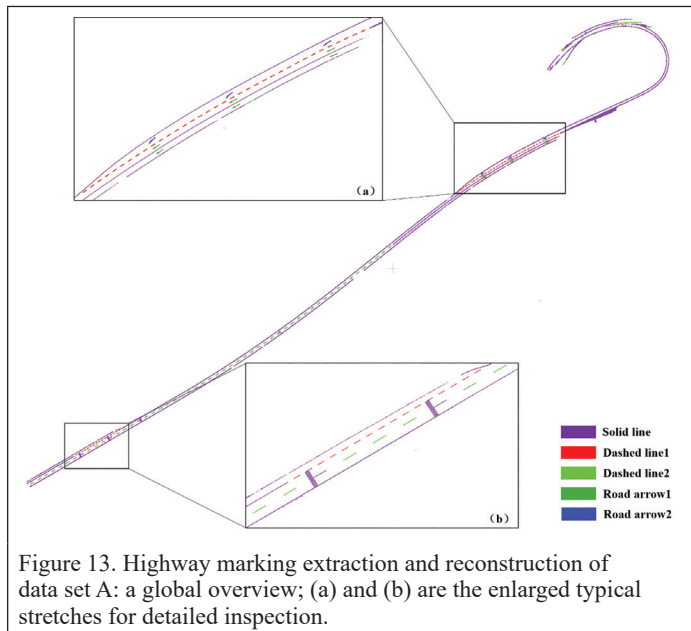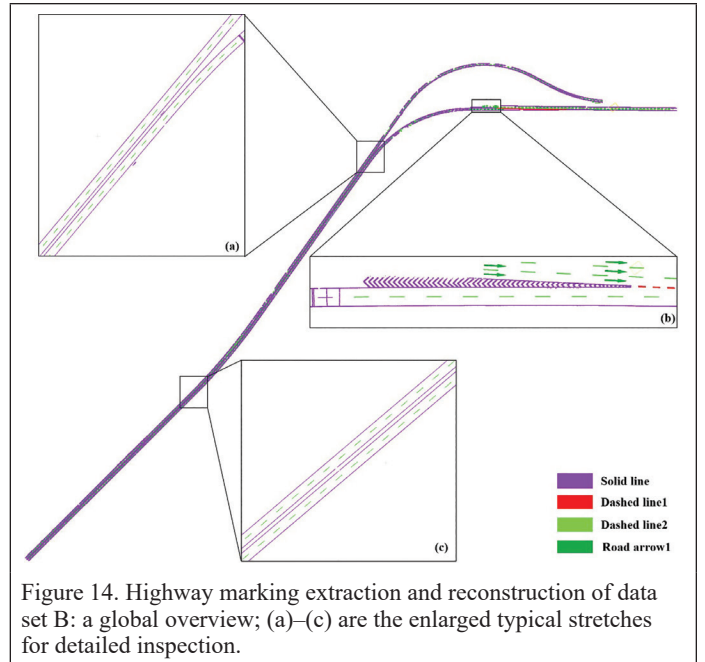

Figure 13. Highway marking extraction and reconstruction of data set A: a global overview; (a) and (b) are the enlarged typical stretches for detailed inspection.
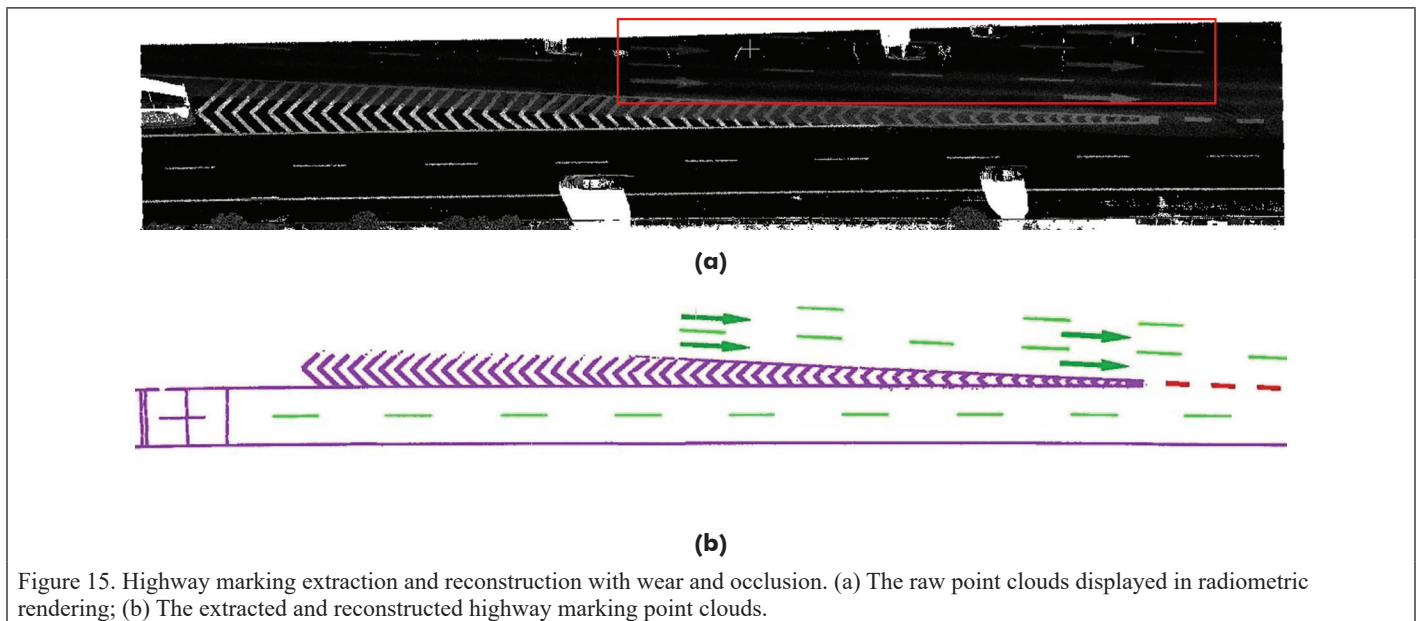

Figure 15. Highway marking extraction and reconstruction with wear and occlusion. (a) The raw point clouds displayed in radiometric rendering; (b) The extracted and reconstructed highway marking point clouds.

Figure 16. Highway marking extraction and reconstruction with various intensities and point densities. (a) The raw point clouds displayed in radiometric rendering; (b) The extracted and reconstructed highway marking point clouds.
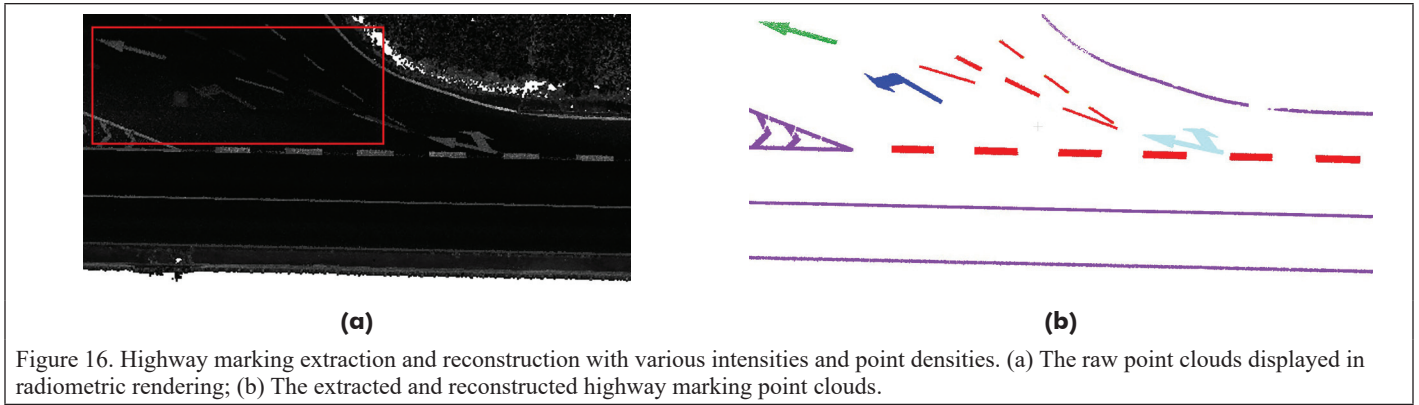
The HM extraction and reconstruction results demonstrate that the proposed combination of the bottom-up and top-down methods is robust to complex highways with different densities, intensities, wear, and occlusion. On the one hand, most existing bottom-up approaches for HM extraction from point clouds use the local intensity difference between the pixel of marking and background to set the threshold, which depends heavily on intensity quality and uniformity. However, intensity quality and uniformity suffer from some factors, including the scanning mechanism of MLS, the performance period of the highway, and other reasons, such as road humidity and dust. Moreover, if adopting a top-down strategy completely, the mass volume of the point cloud leads to a low efficiency for HM extraction, especially in highway scenes owing to its long distance. Based on these challenges of the two strategies above, the proposed approach integrates them for HMs extraction and reconstruction from point clouds in complex highway scenes. First, the bottom-up strategy is adopted to coarsely detect highway marking candidates, which ensures the completeness of the marking objects for improving the recall rate. Simultaneously, the efficiency and accuracy are greatly enhanced by point conversion to featured maps and sophisticated image processing. Then, according to the specification template of the HMs, edge-based matching is adopted to accurately extract and reconstruct the HMs after obtaining the coarse marking candidate objects, a process that constructs the edge models of different highway marking templates and computes the similarity between the edge point of the template in models and the highway marking object in the searching image for scoring to select optimal matching. Therefore, in the proposed approach, we take into account the characteristics of both extraction strategies and the complexity of the existing highway scenes. The method combines the complexity of the existing highway, radiometric appearance, and overall geometric features of the HMs. In contrast to the existing bottom-up approach, we proposed that the process is less sensitive to raw data quality and improves robustness and efficiency.

The quantitative evaluation metrics for HM extraction are precision, recall, and F1-score:

$$\text{Precision} = \frac{\text{TP}}{\text{TP} + \text{FP}} \tag{9}$$

$$\text{Recall} = \frac{\text{TP}}{\text{TP} + \text{FN}} \tag{10}$$

$$F_{score} = 2 \cdot \frac{\text{Precision} \cdot \text{Recall}}{\text{Precision} + \text{Recall}} \tag{11}$$

where TP, FP, and FN are the number of true positives in the extracted results, the number of false positives in the extracted results, and the number of false negatives in the ground truth, respectively.

Manually extracted highway marking points were compared to the results extracted by the present method, and the evaluation measures

of data sets A and B are shown in Table 4 and Table 5, respectively. For solid line markings, the meter is used as the evaluation unit of the identified length, while the object of reconstruction is used as the evaluation unit for nonsolid line markings. Therefore, the evaluation metrics of the solid line and nonsolid line markings are discussed due to different units.

Data sets A and B are both collected in complex highway scenes, with a variety of scene types, severe noise, and wear. As listed in Table 4 and Table 5, the present approach achieved 96.2% and 93.6% in terms of average recall and precision for solid line marking extraction, respectively, and achieved 94.7% and 94.3% with respect to average recall and precision for nonsolid line marking extraction, respectively. The high values of the recall, precision, and F-score measures in all data sets indicate that the proposed method to extract the HMs works well in the existing highway scenes. The slight difference between recall, precision, and F-score in the two data sets shows the stability and reliability of the performance of the proposed method.

The experimental results also show several failures if the following conditions exist: (1) it is easy to confuse or misrecognize the two types of dashed lines when occlusion or wear occurs on raw point clouds because there is the only the difference in length and width between

Table 4. Quantitative evaluation of the highway marking (HM) extraction results in test area A.

Category	GT	TP	FP	FN	Recall	Precision	F-Score
solid line	8760.0	8431.44	576.50	328.55	0.962	0.936	0.949
dash line &1	53	50	5	3	0.943	0.910	0.925
dash line &2	52	49	2	3	0.942	0.960	0.951
road arrow &1	6	6	0	0	1.000	1.000	1.000
road arrow &2	3	5	0	0	1.000	1.000	1.000
overall	113	109	7	6	0.947	0.939	0.943

GT = ground truth; TP = the number of true positives in the extracted results; FP = the number of false positives in the extracted results; FN = the number of false negatives in the ground truth.

Table 5. Quantitative evaluation of the highway marking (HM) extraction results in test area B.

Category	GT	TP	FP	FN	Recall	Precision	F-Score
solid line	25222.0	24099.07	925.92	1122.93	0.955	0.963	0.959
dash line &1	502	478	28	24	0.952	0.944	0.948
dash line &2	51	49	3	2	0.960	0.942	0.951
road arrow &1	5	5	0	0	1.000	1.000	1.000
overall	558	532	31	26	0.953	0.945	0.949

GT = ground truth; TP = the number of true positives in the extracted results; FP = the number of false positives in the extracted results; FN = the number of false negatives in the ground truth.
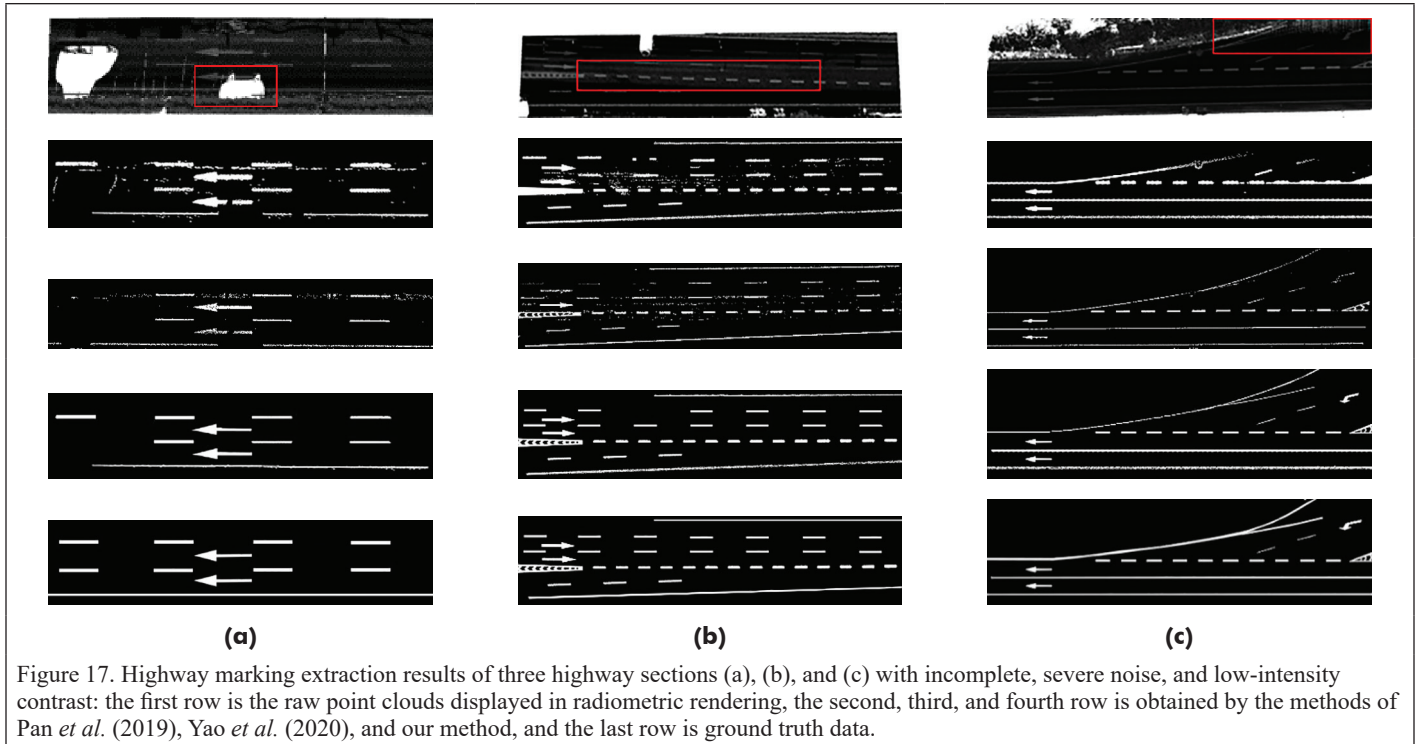
Figure 17. Highway marking extraction results of three highway sections (a), (b), and (c) with incomplete, severe noise, and low-intensity contrast: the first row is the raw point clouds displayed in radiometric rendering, the second, third, and fourth row is obtained by the methods of Pan *et al.* (2019), Yao *et al.* (2020), and our method, and the last row is ground truth data.

Table 6. Quantitative evaluation results of different highway marking extraction methods.

Method	Typical Road Stretches (a)			Typical Road Stretches (b)			Typical Road Stretches (c)		
	Precision (%)	Recall (%)	F-score (%)	Precision (%)	Recall (%)	F-score (%)	Precision (%)	Recall (%)	F-score (%)
Pan *et al.* (2019)	89.64	90.23	89.93	86.47	92.62	89.43	84.29	86.36	85.31
Yao *et al.* (2020)	92.73	86.62	89.57	88.26	89.18	88.71	92.64	94.28	93.45
Ours	94.59	93.63	94.10	95.72	93.46	94.57	95.70	94.95	95.32

dashed lines; (2) when point clouds are collected by working for a long period of the existing highway, it is difficult to avoid putting the pavement point cloud with severe noise identified as some nonsolid line markings; (3) it is inevitable to have some vehicle passes during the MLS work, which causes an obstacle to extraction and recognition of the HMs on incomplete data. To avoid the above failure as much as possible, we conclude some measures taken to improve the reliability and accuracy of HMs extraction. First, to reduce the incomplete point clouds collected, we collect the MLS point clouds during the low-traffic flow period. Second, to obtain a higher point density, we use a slower speed in the process of running the vehicle. Last, the highway department should regularly inspect the conditions of wear or cracks on markings, as well as take measures to perform updates and maintenance.
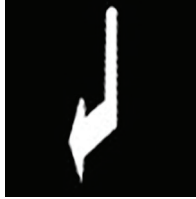
Comparison Analysis

We compared different algorithms using point clouds with incomplete, severe noise, and low-intensity contrast and analyzed the results. The performance was compared with the methods of Pan *et al.* (2019) and Yao *et al.* (2020). Figure 17 shows the results on three typical road stretches, where the HMs marked by red rectangles are incomplete data, severe noise, and uneven intensity. In these cases, the method of Pan *et al.* (2019), which calculates a global intensity threshold to extract the HMs, does not obtain a good result. Although the method of Yao *et al.* (2020) adopting a dynamic threshold using integral images improves the results in most cases, it also yields results with noise when incomplete markings exist. Compared with the proposed method, the above two methods both adopt a bottom-up strategy and are sensitive to imperfect data, while our method adopts a divide-and-conquer strategy and model-driven approach, takes into account both the complexity of the data and the efficiency of the algorithm, and achieves better results. Table 6 presents the performance of the different methods. Since there

are different degrees of noise in the three test data, all F-scores for the method of Pan *et al.* (2019) are less than 90%. The method of Yao *et al.* (2020) achieves high precision, but the F-score is insufficient in typical road stretches (a) and (b) (89.57% and 88.71%, respectively). By achieving an average precision of 95.67%, average precision of 94.01%, and average precision of 94.66% in three typical road stretches, the present method performs better than the other methods, and the findings further show the effectiveness of the proposed method.

Degradation Analysis

After extraction and reconstruction of HMs, we carried out a degradation analysis on each object of marking in test areas A and B. According to the section "Highway marking degradation analysis", taking into account the geometric appearance and radiation information of HMs, the value of SEM and SAM is calculated by edge-based and area-based template matching, respectively. The value of SEM and SAM describe the condition of the current HMs from different aspects, in which the SEM value calculated for each marking object provides the completeness of the marking contour and the SAM value provides the consistency within the marking. Through trial and error on the SEM and SAM with the various conditions of highway markings, we set degradation thresholds to count the number of two different types of degradation present in the HMs. Furthermore, a database can be established to describe the degradation result of each marking object in the test area, as shown in Table 7, as an example of a database. Assessment results of each marking object include image, type, position (geographic coordinate system was converted to projection of Universal Transverse Mercator (UTM)), the value of SEM and SAM, and acceptance of degradation (marked by √ represents no degradation; otherwise, marked by × represents maintenance is required). According to the content of the database presented in Table 7, we concluded

Table 7. Quantitative degradation analysis results of different lane marking extraction method.

Object				
Marking type	Dash line	Straight arrow	Right-turn arrow	Straight or right-turn arrow
Assessment results				
Image				
Position (UTM)	(524967.36, 3209313.98)	(529634.43, 3210105.80)	(529664.58, 3210230.65)	(529159.24, 3208493.70)
SEM	0.934	0.952	0.965	0.931
SAM	0.949	0.976	0.951	0.954
Quality	√	√	√	√
Assessment results				
Image				
Position (UTM)	(373273.13, 3426763.02)	(373216.15, 3426813.11)	(365660.97, 3428576.27)	(373967.51, 3426262.71)
SEM	0.873	0.851	0.902	0.881
SAM	0.842	0.876	0.892	0.852
Quality	×	×	×	×

UTM = Universal Transverse Mercator; SEM = the score of the best edge-based template matching; SAM = the score of area-based template matching. Cells marked by √ represents no degradation; otherwise, marked by × represents maintenance is required.

Table 8. Quantitative assessment results of highway marking degradation in test area A.

Type	Total	The Number of SEM Degradation	The Number of SAM Degradation	The Rate of SEM Degradation	The Rate of SAM Degradation
Dashed line 1	53	6	4	11.32%	7.54%
Dashed line 2	52	7	5	13.46%	9.61%
Straight arrow	6	1	0	16.66%	0
Left-turn arrow	3	0	0	0	0

SEM = the score of the best edge-based template matching; SAM = the score of area-based template matching.

Table 9. Quantitative assessment results of highway marking degradation in test area B.

Type	Total	The Number of SEM Degradation	The Number of SAM Degradation	The Rate of SEM Degradation	The Rate of SAM Degradation
Dashed line1	502	28	16	5.57%	3.18%
Dashed line2	51	6	5	11.76%	9.80%
Straight arrow	5	1	0	20.00%	0

SEM = the score of the best edge-based template matching; SAM = the score of area-based template matching.

that when there is an incomplete contour or internal inconsistency occurring in the HMs, there will be a significant change in the values of SEM and SAM to indicate the degree of degradation. Meanwhile, the highway maintenance department can efficiently locate the highway markings with existing wear or missing parts and implement repair and maintenance. For example, if the significant drop of the SEM or SAM value indicates existing incompletion and wear on the marking object, repair is needed.

Table 8 and Table 9 list the statistical results of HM degradation in test areas A and B, where the number of marking contour completeness degradation (SEM degradation) and the number of marking consistency degradation (SAM degradation) are counted, respectively. Although the

values of SEM and SAM have not yet established an absolute function with the degree of wear of the HMs, these two indicators provide explicit guidance for carrying out the repair of the highway maintenance department. Moreover, the values of SEM and SAM collected in different phases also provide a relative comparison for reflecting changes in conditions in the HMs.

Conclusion

This paper addressed the problem of the extraction, reconstruction, and degradation analysis of HMs in complex highway scenes using MLS point clouds. The main contribution of this study was a model-driven approach for the extraction and reconstruction of highway markings with precise positions and semantics and constructing two evaluation indicators to quantitatively analyze highway marking degradation for efficient maintenance. The proposed method was tested on two data sets with lengths of 3.9 km and 12.8 km, and promising results were obtained. The reported average precision values of 93.8% and 95.5% and average recall value of 95.4% and 95.4% for the two types of markings in the two test areas show the reliability of the proposed approach for extracting and reconstructing HMs. In terms of the degradation analysis of HMs, a database is established for reflecting the condition of the marking object, including marking object type, position, and the value of two degradation indicators. The detailed description contents of the HMs generated by the present method provide significant support for the digital operation, maintenance, and intelligent management of highways. Moreover, the results can also be applied to studies of HD maps and road safety assessments.

In the future, our research work will focus on how a rigorous model can be established between the degradation degree of the HMs and metrics of description.

Acknowledgments

References

Bello, S. A., S. Yu, C. Wang, J. M. Adam and J. Li. 2020. Review: Deep learning on 3D point clouds. *Remote Sensing* 12(11):1729.

Burghardt, T. E., R. Popp, B. Helmreich, T. Reiter and M. Artmann. 2021. Visibility of various road markings for machine vision. *Case Studies in Construction Materials* 15:e00579.

Cha, Y. J., W. Choi, G. Suh, S. Mahmoudkhani and O. Buyukozturk. 2018. Autonomous structural visual inspection using region-based deep learning for detecting multiple damage types. *Computer-Aided Civil Infrastructure Engineering* 33(9):731–747.

Che, E., M. J. Olsen, C. E. Parrish and J. Jung. 2019. Pavement marking retroreflectivity estimation and evaluation using mobile Lidar data. *Photogrammetric Engineering and Remote Sensing* 85(8):573–583.

Chen, S., Z. Zhang, R. Zhong, L. Zhang, H. Ma and L. Liu. 2021. A dense feature pyramid network-based deep learning model for road marking instance segmentation using MLS point clouds. *IEEE Transactions on Geoscience and Remote Sensing* 59(1):784–800.

Chen, X., B. Kohlmeyer, M. Stroila, N. Alwar, R. Wang and J. Bach. 2009. Next generation map making: Geo-referenced ground-level LIDAR point clouds for automatic retro-reflective road feature extraction. Pages 488–491 in *Proceedings of the 17th ACM SIGSPATIAL International Conference on Advances in Geographic Information Systems*, held in Seattle, Wa., 4–6 November 2009.

Cheng, M., H. Zhang, C. Wang and J. Li. 2017. Extraction and classification of road markings using mobile laser scanning point clouds. *IEEE Journal of Selected Topics in Applied Earth Observations Remote Sensing* 10(3):1182–1196.

Cheng, Y. T., A. Patel, C. Wen, D. Bullock and A. Habib. 2020. Intensity thresholding and deep learning based lane marking extraction and lane width estimation from mobile light detection and ranging (LiDAR) point clouds. *Remote Sensing* 12(9):1379.

Fang, L., Z. Huang, H. Luo and C. Cheng. 2019. Solid lanes extraction from mobile laser scanning point clouds. *Acta Geodaetica et Cartographica Sinica* 48(8):960–974.

Ge, X., B. Wu, Y. Li and H. Hu. 2019. A multi-primitive-based hierarchical optimal approach for semantic labeling of ALS point clouds. *Remote Sensing* 11(10):1243.

Guan, H., J. Li, Y. Yu, C. Cheng, M. Chapman and B. Yang. 2014. Using mobile laser scanning data for automated extraction of road markings. *ISPRS Journal of Photogrammetry and Remote Sensing* 87:93–107.

Guan, H., J. Li, Y. Yu, M. Chapman and C. Wang. 2015a. Automated road information extraction from mobile laser scanning data. *IEEE Transactions on Intelligent Transportation Systems* 16(1):194–205.

Guan, H., J. Li, Y. Yu, Z. Ji and C. Wang. 2015b. Using mobile LiDAR data for rapidly updating road markings. *IEEE Transactions on Intelligent Transportation Systems* 16(5):2457–2466.

Guan, H., J. Li, S. Cao and Y. Yu. 2016. Use of mobile LiDAR in road information inventory: A review. *International Journal of Image and Data Fusion* 7(3):219–242.

Guo, J., M. J. Tsai and J. Y. Han. 2015. Automatic reconstruction of road surface features by using terrestrial mobile lidar. *Automation in Construction* 58:165–175.

Han, H., Y. Ding, Q. Zhu, W. Bo, H. Lin, Z. Du and Y. Zhang. 2014. An adaptive surface filter for airborne laser scanning point clouds by means of regularization and bending energy. *ISPRS Journal of Photogrammetry and Remote Sensing* 92(2):98–111.

Han, X., Z. Dong and B. Yang. 2021. A point-based deep learning network for semantic segmentation of MLS point clouds. *ISPRS Journal of Photogrammetry Remote Sensing* 175:199–214.

Jaakkola, A., J. Hyyppä, H. Hyyppä and A. Kukko. 2008. Retrieval Algorithms for road surface modelling using laser-based mobile mapping. *Sensors* 8(9):5238–5249.

Jung, J., E. Che, M. J. Olsen and C. Parrish. 2019. Efficient and robust lane marking extraction from mobile lidar point clouds. *ISPRS Journal of Photogrammetry and Remote Sensing* 147:1–18.

Kashani, A. G., M. J. Olsen, C. E. Parrish and N. Wilson. 2015. A review of LIDAR radiometric processing: From ad hoc intensity correction to rigorous radiometric calibration. *Sensors* 15(11):28099–28128.

Kawano, M., K. Mikami, S. Yokoyama, T. Yonezawa and J. Nakazawa. 2017. Road marking blur detection with drive recorder. Pages 4092–4097 in *2017 IEEE International Conference on Big Data (Big Data)*), held in Boston, Mass., 11–14 November 2017.

Kheyrollahi, A. and T. P. Breckon. 2012. Automatic real-time road marking recognition using a feature driven approach. *Machine Vision Applications* 23(1):123–133.

Korpela, I., H. O. Ørka, J. Hyyppä, V. Heikkinen and T. Tokola. 2010. Range and AGC normalization in airborne discrete-return LiDAR intensity data for forest canopies. *ISPRS Journal of Photogrammetry and Remote Sensing* 65(4):369–379.

Kumar, P., C. P. Mcelhinney, P. Lewis and T. Mccarthy. 2014. Automated road markings extraction from mobile laser scanning data. *International Journal of Applied Earth Observation and Geoinformation* 32:125–137.

Li, Y., R. Bu, M. Sun, W. Wu, X. Di and B. Chen. 2018. PointCNN: Convolution on X-transformed points. Pages 820–830 in *Annual Conference on Neural Information Processing Systems 2018 (NeurIPS)*, held in Montréal, Canada, 3–8 December 2018.

Ma, L., Y. Li, J. Li, C. Wang, R. Wang and M. Chapman. 2018. Mobile laser scanned point-clouds for road object detection and extraction: A review. *Remote Sensing* 10(10):1531.

Ma, L., Y. Li, J. Li, Z. Zhong and M. A. Chapman. 2019. Generation of horizontally curved driving lines in HD maps using mobile laser scanning point clouds. *IEEE Journal of Selected Topics in Applied Earth Observations Remote Sensing* 12(5):1572–1586.

Mi, X., B. Yang, Z. Dong, C. Liu, Z. Zong and Z. Yuan. 2021. A two-stage approach for road marking extraction and modeling using MLS point clouds. *ISPRS Journal of Photogrammetry and Remote Sensing* 180:255–268.

Pan, Y., B. Yang, S. Li, H. Yang, Z. Dong and X. Yang. 2019. Automatic road markings extraction, classification and vectorization from mobile laster scanning data. Pages 1089–1096 in *The International Archives of the Photogrammetry, Remote Sensing and Spatial Information Sciences*). https://doi.org/10.5194/isprs-archives-XLII-2-W13-1089-2019.

Qi, C. R., S. Hao, K. Mo and L. J. Guibas. 2017. PointNet: Deep learning on point sets for 3D classification and segmentation. Pages 652–660 in *Proceedings of the IEEE Conference on Computer Vision and Pattern Recognition*, held in Honolulu, Hawaii, 21–26 July 2017.

Rastiveis, H., A. Shams, W. A. Sarasua and J. Li. 2019. Automated extraction of lane markings from mobile LiDAR point clouds based on fuzzy inference. *ISPRS Journal of Photogrammetry and Remote Sensing* 160:149–166.

Riveiro, B., H. González-Jorge, J. Martínez-Sánchez, L. Díaz-Vilariño and P. Arias. 2015. Automatic detection of zebra crossings from mobile LiDAR data. *Optics & Laser Technology* 70:63–70.

Soilán, M., B. Riveiro, J. Martínez-Sánchez and P. Arias. 2017. Segmentation and classification of road markings using MLS data. *ISPRS Journal of Photogrammetry and Remote Sensing* 123:94–103.

Soilán, M., A. Justo, A. Sánchez-Rodríguez and B. Riveiro. 2020. 3D point cloud to BIM: Semi-automated framework to define IFC alignment entities from MLS-acquired LiDAR data of highway roads. *Remote Sensing* 12(14):2301.

Soilán, M., D. González-Aguilera, A. del-Campo-Sánchez, D. Hernández-López and S. Del Pozo. 2022. Road marking degradation analysis using 3D point cloud data acquired with a low-cost mobile mapping system. *Automation in Construction* 141:104446.

Spencer Jr, B. F., V. Hoskere and Y. Narazaki. 2019. Advances in computer vision-based civil infrastructure inspection and monitoring. *Engineering* 5(2):199–222.

Wang, J., R. Lindenbergh and M. Menenti. 2017. SigVox—A 3D feature matching algorithm for automatic street object recognition in mobile laser scanning point clouds. *ISPRS Journal of Photogrammetry and Remote Sensing* 128:111–129.

Wen, C., X. Sun, J. Li, C. Wang, Y. Guo and A. Habib. 2019. A deep learning framework for road marking extraction, classification and completion from mobile laser scanning point clouds. *ISPRS Journal of Photogrammetry and Remote Sensing* 147:178–192.

Yan, L., H. Li, J. Tan, Z. Li, H. Xie and C. Chen. 2016. Scan line based road marking extraction from mobile LiDAR point clouds. *Sensors* 16(6):903.

Yang, B., L. Fang, Q. Li and J. Li. 2012. Automated extraction of road markings from mobile Lidar point clouds. *Photogrammetric Engineering and Remote Sensing* 78(4):331–338.

Yang, B., Y. Liu, Z. Dong, F. Liang, B. Li and X. Peng. 2017. 3D local feature BKD to extract road information from mobile laser scanning point clouds. *ISPRS Journal of Photogrammetry and Remote Sensing* 130:329–343.

Yang, M., Y. Wan, X. Liu, J. Xu, Z. Wei, M. Chen and P. Sheng. 2018. Laser data based automatic recognition and maintenance of road markings from MLS system. *Optics & Laser Technology* 107:192–203.

Yao, L., C. Qin, Q. Chen, H. Wu and S. Zhang. 2020. Automatic extraction and recognition of road markings based on vehicle laser point cloud. *ISPRS Annals of the Photogrammetry, Remote Sensing and Spatial Information Sciences*: 313–319. https://doi.org/10.5194/isprs-annals-V-2-2020-313-2020.

Yao, Y. and Q. Hu. 2014. Automatic extraction method study of road marking lines based on projection of point clouds. Pages 1–4 *in 2014 22nd International Conference on Geoinformatics*, held in Kaohsiung, Taiwan, 25–27 June 2014 .

Yu, Y., J. Li, H. Guan, F. Jia and C. Wang. 2017. Learning hierarchical features for automated extraction of road markings from 3-D mobile LiDAR point clouds. *IEEE Journal of Selected Topics in Applied Earth Observations Remote Sensing* 8(2):709–726.

Zai, D., J. Li, Y. Guo, M. Cheng, Y. Lin, H. Luo and C. Wang. 2018. 3-D road boundary extraction from mobile laser scanning data via supervoxels and graph cuts. *IEEE Transactions on Intelligent Transportation Systems* 19(3):802–813.

Zhang, D., X. Xu and R. Gui. 2019. Automatic road-marking detection and measurement from laser-scanning 3D profile data. *Automation in Construction* 108:102957.

Zhang, H., J. Li, M. Cheng and C. Wang. 2016. Rapid Inspection of Pavement Markings Using Mobile Laser Scanning Point Clouds. *International Archives of the Photogrammetry, Remote Sensing and Spatial Information Sciences* XLI-B1:717–723. https://doi.org/10.5194/isprsarchives-XLI-B1-717-2016.

Zhou, Y., R. Huang, T. Jiang, Z. Dong and B. Yang. 2021. Highway alignments extraction and 3D modeling from airborne laser scanning point clouds. *International Journal of Applied Earth Observation Geoinformation* 102:102429.

Zhu, Q., L. Zhang, Y. Ding, H. Hu and X. Ge. 2022. From real 3D modeling to digital twin modeling. *Acta Geodaetica et Cartographica Sinica* 51(6):1040–1049.

WHO'S WHO IN ASPRS

Founded in 1934, the American Society for Photogrammetry and Remote Sensing (ASPRS) is a scientific association serving thousands of professional members around the world. Our mission is to advance knowledge and improve understanding of mapping sciences to promote the responsible applications of photogrammetry, remote sensing, geographic information systems (GIS) and supporting technologies.

BOARD OF DIRECTORS
BOARD OFFICERS

President
Lorraine B. Amenda, PLS, CP
Towill, Inc

President-Elect
Bandana Kar
Oak Ridge National Lab

Vice President
Amr Abd-Elrahman
University of Florida

Past President
Christopher Parrish, Ph.D
Oregon State University

Treasurer
John McCombs
NOAA

Secretary
Harold Rempel
ESP Associates, Inc.

COUNCIL OFFICERS
ASPRS has six councils. To learn more, visit https://www.asprs.org/Councils.html.

Sustaining Members Council
Chair: Ryan Bowe
Deputy Chair: Melissa Martin

Technical Division Directors Council
Chair: Hope Morgan
Deputy Chair:

Standing Committee Chairs Council
Chair:
Deputy Chair:

Early-Career Professionals Council
Chair: Youssef Kaddoura
Deputy Chair:

Region Officers Council
Chair: Demetrio Zourarakis
Deputy Chair: Jason Krueger

Student Advisory Council
Chair: Oscar Duran
Deputy Chair:

TECHNICAL DIVISION OFFICERS
ASPRS has seven professional divisions. To learn more, visit https://www.asprs.org/Divisions.html.

Geographic Information Systems Division
Director: Denise Theunissen
Assistant Director: Jin Lee

Lidar Division
Director: Ajit Sampath
Assistant Director: Mat Bethel

Photogrammetric Applications Division
Director: Ben Wilkinson
Assistant Director: Hank Theiss

Primary Data Acquisition Division
Director: Srini Dharmapuri
Assistant Director: Ravi Soneja

Professional Practice Division
Director: Hope Morgan
Assistant Director: Matt Elious

Remote Sensing Applications Division
Director: Tao Liu
Assistant Director: Indu Jeyachandran

Unmanned Autonomous Systems (UAS)
Director: Jacob Lopez
Assistant Director: Bahram Salehi

REGION PRESIDENTS
ASPRS has 13 regions to serve the United States. To learn more, visit https://www.asprs.org/regions.html.

Alaska Region

Cascadia Region
Jimmy Schulz

Eastern Great Lakes Region
Craig Fry

Florida Region
Matt LaLuzerne

Gulf South
Cody Condron

Heartland Region
Whit Lynn

Mid-South Region
David Hughes

North Atlantic Region
Kurt Lutz

Northeast Region

Pacific Southwest Region
Omar Mora

Potomac Region
Jason Brown

Rocky Mountain Region
Trent Casi

Western Great Lakes Region
Adam Smith

SUSTAININGMEMBERS

ACI USA Inc.
Weston, Florida
https://acicorporation.com/
Member Since: 2/2018

Aerial Services, Inc.
Cedar Falls, Iowa
www.AerialServicesInc.com
Member Since: 5/2001

Airworks Solutions Inc.
Boston, Massachusetts
Member Since: 3/2022

Applanix
Richmond Hill, Ontario, Canada
http://www.applanix.com
Member Since: 7/1997

Ayres Associates
Madison, Wisconsin
www.AyresAssociates.com
Member Since: 1/1953

Cardinal Systems, LLC
Flagler Beach, Florida
www.cardinalsystems.net
Member Since: 1/2001

CT Consultants
Mentor, Ohio
Member Since: 3/2022

Dewberry
Fairfax, Virginia
www.dewberry.com
Member Since: 1/1985

Esri
Redlands, California
www.esri.com
Member Since: 1/1987

GeoCue Group
Madison, Alabama
http://www.geocue.com
Member Since: 10/2003

Geographic Imperatives LLC
Centennial, Colorado
Member Since: 12/2020

GeoWing Mapping, Inc.
Richmond, California
www.geowingmapping.com
Member Since: 12/2016

GPI Geospatial Inc.
Orlando, Florida
www.aca-net.com
Member Since: 1/1994

Halff Associates, Inc.
Richardson, Texas
www.halff.com
Member Since: 8/2021

Keystone Aerial Surveys, Inc.
Philadelphia, Pennsylvania
www.kasurveys.com
Member Since: 1/1985

Kucera International
Willoughby, Ohio
www.kucerainternational.com
Member Since: 1/1992

L3Harris Technologies
Broomfield, Colorado
www.l3harris.com
Member Since: 6/2008

Merrick & Company
Greenwood Village, Colorado
www.merrick.com
Member Since: 4/1995

Nearmap
South Jordan, Utah
www.nearmap.com
Member Since: 6/2023

NV5 Geospatial
Sheboygan Falls, Wisconsin
www.quantumspatial.com
Member Since: 1/1974

Pickett and Associates, Inc.
Bartow, Florida
www.pickettusa.com
Member Since: 4/2007

PixElement
Belmont, Michigan
https://pixelement.com
Member Since: 2/2017

Riegl USA, Inc.
Orlando, Florida
www.rieglusa.com
Member Since: 11/2004

Robinson Aerial Surveys, Inc.(RAS)
Hackettstown, New Jersey
www.robinsonaerial.com
Member Since: 1/1954

Sanborn Map Company
Colorado Springs, Colorado
www.sanborn.com
Member Since: 10/1984

Surdex Corporation
Chesterfield, Missouri
www.surdex.com
Member Since: 12/2011

Surveying And Mapping, LLC (SAM)
Austin, Texas
www.sam.biz
Member Since: 12/2005

T3 Global Strategies, Inc.
Bridgeville, Pennsylvania
https://t3gs.com/
Member Since: 6/2020

Towill, Inc.
San Francisco, California
www.towill.com
Member Since: 1/1952

Woolpert LLP
Dayton, Ohio
www.woolpert.com
Member Since: 1/1985

SUSTAININGMEMBERBENEFITS

Membership

- ✓ Provides a means for dissemination of new information
- ✓ Encourages an exchange of ideas and communication
- ✓ Offers prime exposure for companies

Benefits of an ASPRS Membership

- Complimentary and discounted Employee Membership*
- E-mail blast to full ASPRS membership*
- Professional Certification Application fee discount for any employee
- Member price for ASPRS publications
- Discount on group registration to ASPRS virtual conferences
- Sustaining Member company listing in ASPRS directory/website
- Hot link to company website from Sustaining Member company listing page on ASPRS website
- Press Release Priority Listing in *PE&RS* Industry News
- Priority publishing of Highlight Articles in *PE&RS* plus, 20% discount off cover fee
- Discount on *PE&RS* advertising
- Exhibit discounts at ASPRS sponsored conferences (exception ASPRS/ILMF)
- Free training webinar registrations per year*
- Discount on additional training webinar registrations for employees
- Discount for each new SMC member brought on board (Discount for first year only)

*quantity depends on membership level

LANDSAT'S ENDURING LEGACY
PIONEERING GLOBAL LAND OBSERVATIONS FROM SPACE
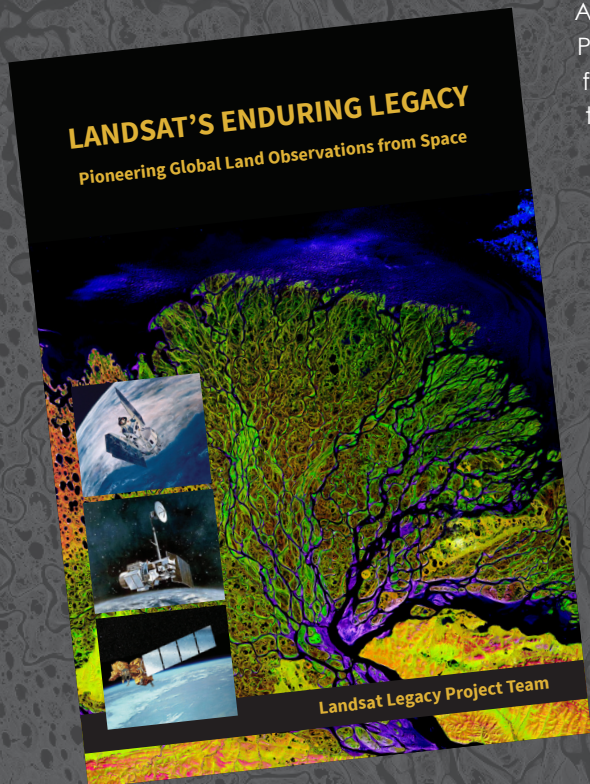
After more than 15 years of research and writing, the Landsat Legacy Project Team published, in collaboration with the American Society for Photogrammetry and Remote Sensing (ASPRS), a seminal work on the nearly half-century of monitoring the Earth's lands with Landsat. Born of technologies that evolved from the Second World War, Landsat not only pioneered global land monitoring but in the process drove innovation in digital imaging technologies and encouraged development of global imagery archives. Access to this imagery led to early breakthroughs in natural resources assessments, particularly for agriculture, forestry, and geology. The technical Landsat remote sensing revolution was not simple or straightforward. Early conflicts between civilian and defense satellite remote sensing users gave way to disagreements over whether the Landsat system should be a public service or a private enterprise. The failed attempts to privatize Landsat nearly led to its demise. Only the combined engagement of civilian and defense organizations ultimately saved this pioneer satellite land monitoring program. With the emergence of 21st century Earth system science research, the full value of the Landsat concept and its continuous 45-year global archive has been recognized and embraced. Discussion of Landsat's future continues but its heritage will not be forgotten.

The pioneering satellite system's vital history is captured in this notable volume on Landsat's Enduring Legacy.

Landsat Legacy Project Team

Samuel N. Goward

Darrel L. Williams

Terry Arvidson

Laura E. P. Rocchio

James R. Irons

Carol A. Russell

Shaida S. Johnston

Landsat's Enduring Legacy

Hardback. 2017, ISBN 1-57083-101-7

Member/Non-member	$48*
Student Member	$36*

* Plus shipping

Order online at
www.asprs.org/landsat